SAPIENZA
UNIVERSITÀ DI ROMA

Study of the beam-cavity interaction in the CERN PS 10 MHz cavities and investigation of hardware solutions to reduce beam loading

PhD in Accelerator Physics

Ciclo XXIX

Giorgia Favia

CERN-THESIS-2017-166
21/02/2017

Thesis advisor:

Luigi Palumbo

CERN supervisor:

Michele Morvillo

Alla mia famiglia

Contents

List of Figures

Introduction

The most known accelerator at CERN is the Large Hadron Collider (LHC), in which proton beams are accelerated to the highest energy in the world and then put in collision to probe into the heart of matter. However, the LHC top energy is gradually built up in a chain of accelerators of equal importance. Each machine boosts the energy of the particles beam, before injecting it into the next machine in the sequence. Since the quality of delivered beam from the injector chain determines greatly the overall performance of the LHC, studies are carried out to overcome eventual beam parameters limitations in the injectors, in the perspective of increasing the LHC beam brightness.

In particular, in the Proton Synchrotron (PS), where the LHC protons longitudinal structure (bunch spacing) is determined as the result of a sophisticated series of Radio Frequency (RF) gymnastics, collective effects were identified as a major limitation to the achievable beam current delivered to the LHC.

One major cause of collective effects is the beam coupling impedance, the quantity describing the effect of the fields induced by a beam passing through any accelerator device back on itself. Dedicated machine development studies pointed out the RF cavities to be one of the major source of instability in the PS. In particular, the 10 MHz RF system, responsible for beam acceleration, was identified as the most probable impedance source in the machine. The cavity impedance limits the circulating intensity in the accelerator since the beam-induced voltage could trigger longitudinal instabilities causing beam losses. For this reason the cavity impedance seen by the beam must be kept as low as possible.

This thesis focuses on the improvements of the wide band feedback system that encloses the 10 MHz cavities and their driving amplifier. It describes the upgrade it underwent to reduce the cavity impedance seen by the beam, avoiding a complete

redesign of the amplifier-cavity system and keeping the present configuration of the vacuum tubes amplifier driving the cavity. This work describes the studies that were carried out to quantify the contribution of the 10 MHz RF system to the PS longitudinal impedance. It, indeed, summarizes the measurements and simulations that led to a full characterization and evaluation of the effective impedance of the eleven 10 MHz cavity-amplifier systems installed in the PS.
The thesis is structured as described in the following.
Chapter 1 offers an overview of the CERN accelerator complex and recalls the main beam dynamics concepts used throughout this thesis. It is mainly focused on the particles longitudinal motion and the acceleration provided by the RF cavities.
In addition, the beam-cavity interaction is analyzed, focusing on the main longitudinal instabilities that originate from this interaction: wakefields and beam loading. Consequently the definition of the longitudinal coupling impedance, being the main object of study, is recalled. Finally the wide-band feedback as cure of the beam loading is presented.

Chapter 2 describes the PS and its role as the third accelerator in the LHC injector chain. An overview of its RF systems, whose performance we aim to improve, is given and its role in the production of the "LHC-type" beams is highlighted. Additionally, the PS main beam parameters treated in this document are listed. Finally the LHC Injector Upgrade (LIU) project is presented, explaining its main goals and locating our studies into the project.

Chapter 3 focuses on the 10 MHz RF system of the PS. The cavities are presented with an overview of their main components, parameters and control systems. The amplifier driving the 10 MHz cavities in its standard configuration is described with the performed measurements characterizing all of the system stages. In addition, a circuital model describing the cavity-amplifier system, developed using the PSPICE simulation tool, is presented. The results of numerical simulation, compared with measurements, are reported in the chapter.

Chapter 4 describes the proposed upgrade of the PS 10 MHz RF system resulting from this thesis work. The improvement of the amplifier-cavity system's wide-band

feedback to reduce the impedance seen by the beam is described. The upgrade focusing on the feedback amplifier loop gain increase is made possible only by improving its stability. In this context, the proposed solutions and the adjustments to increase the chain amplifiers gain are presented with a focus on the stability margins of the system. The new components which have been developed and installed in a final prototype of the amplifier are described as well. Finally, an analysis of the dedicated measurements, benchmarked by PSPICE simulations is presented, assessing the performance of the amplifier and the expected impedance reduction.

Chapter 5 presents the results of some studies on the ferrite properties, which have been carried out throughout the development of the new amplifier prototype. Ferrite is used as core of the 10 MHz cavities as well as in other elements of the amplifier chain. A measurement technique for the evaluation of the ferrite properties is presented. In this context, an innovative method for biasing the ferrites has been introduced and tested.

Chapter 6 is dedicated to the study of the beam cavity interaction in the PS 10 MHz cavities, carried out via measurements and simulations.
A full characterization of this interaction has been obtained through the evaluation of the cavity impedance seen by the beam. The latter is presented as the result of a dedicated measurement campaign and numerical simulations.
The PSPICE model, described in Chapter 3, is used to benchmark the measurements and study the impact of the cavity-amplifier system components in the interaction. In this context, the results of the study focused on the distribution of the induced voltage in the cavity, when the accelerating gaps are short-circuited by high voltage relays, are presented.
Moreover, the chapter presents an innovative combined CST-PSPICE model of the amplifier-cavity system, that accounts for the feedback amplifier effect and the real geometry of the cavity in the evaluation of the coupling impedance. Finally, measurements performed to validate the upgrade of the amplifier are presented and the consequent impedance reduction is demonstrated.

Chapter 1

Basics of beam dynamics

In this chapter, the motion of the particles in a synchrotron is reviewed. Special attention is given to the instabilities caused by the interaction of a charged particle beam with its surroundings, as wakefield and beam loading. For the sake of completeness, a detailed treatment of the beam dynamics can be found in [1] [2].

1.1 CERN accelerator complex

The European Organization for Nuclear Research (CERN) is an international laboratory, located on the Franco-Swiss border near Geneva. CERN's main function is to design, construct and run particle accelerators and associated experimental areas, operated for nuclear and particle physics research [3]. The accelerator complex at CERN is a sequence of machines that accelerate particles to increasingly higher energies. The Large Hadron Collider (LHC), a 27 km long particle accelerator, is the last element of the accelerator chain, in which proton beams are accelerated to the highest energy in the world and then put in collision. The particles produced by collisions in the accelerator experiments are analyzed in the LHC detectors. Most of the other accelerators in the chain have associated experimental halls, where beams are used for experiments at lower energies, with collisions on a fixed target.
A full scheme of the CERN accelerator chain is shown in Fig. 1.1, denoting the various type of circulating beams in the different machines. Since this work meanly treats proton beam dynamics, in the following the proton beam path in the accelerator chain

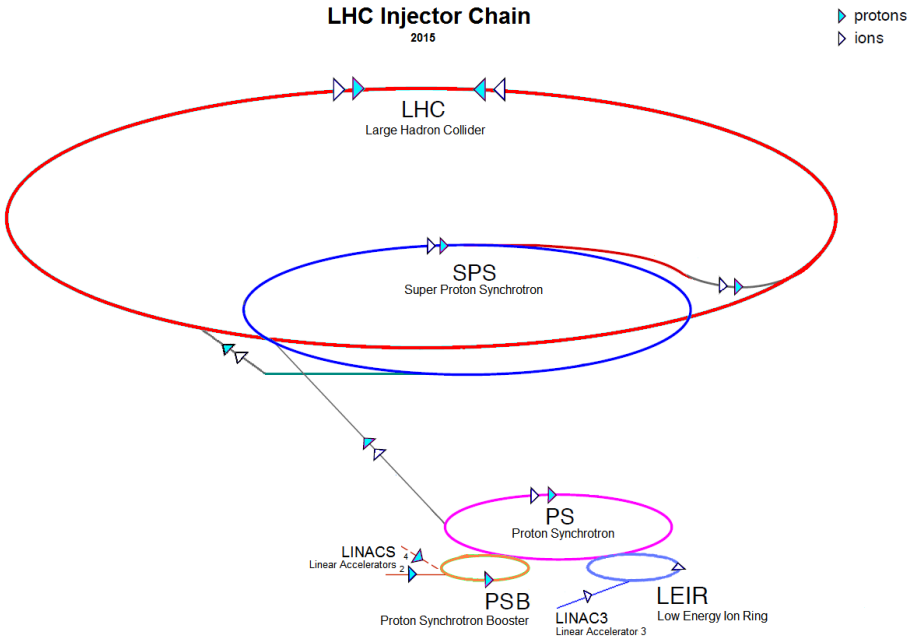

Figure 1.1: CERN accelerators chain [3].

is briefly described.

The proton source is an hydrogen gas injected in a plasma chamber. An electric field strips hydrogen atoms of their electrons, extracting protons at 100 keV towards LINAC 2.

The linear accelerator, LINAC 2, is the first accelerator in the chain. It captures protons in bunches and accelerates them to the energy of 50 MeV. A new injector is in preparation, the LINAC 4, where hydogen anions H^- will be produced and accelerated to 160 MeV to improve the injector complex performance and overcome brightness limitations. The beam is then injected into the Proton Synchrotron Booster (PSB), which consists of four superimposed synchrotrons that accelerate the protons to 1.4 GeV (it will soon be upgraded to 2 GeV). The PSB is followed by the Proton Synchotron (PS), which pushes the beam up to a momentum of 26 GeV/c.

The protons are then sent to the Super Proton Synchrotron (SPS) where they are accelerated to 450 GeV/c. The protons are finally transferred to the two beam pipes of the LHC. The two beams in the two adjacent chambers circulate in opposite directions and are brought to collision at specific points along the circumference [4]. The injected beams are brought up by design report to 7 TeV/c, making it the world's

highest energy particle accelerator.

Beams circulate for many hours inside the LHC beam pipes under normal operating conditions. The two beams are brought into collision inside four Interaction Points (IP 1, 2, 5, 8), where the detectors of ATLAS, ALICE, CMS and LHCb experiments are respectively installed.

From 2010 to 2012, at the start of Run I, the LHC was operated at half of its design beam energy (3.5 TeV). Starting from 2012, the top energy was increased to 4 TeV until the Long Shutdown 1 (LS1, 2013–2015). On the 4$^{\text{th}}$ July 2012, the discovery of a new boson at about 125 GeV, the long awaited Higgs particle, was announced [5] [6]. On the restart in 2015, the top energy was set to 6.5 TeV.

The injectors do not only manipulate and accelerate the LHC beams, but they additionally provide beams with different energies to various experiments. For example, beams extracted from the PS Booster are sent to the Online Isotope Mass Separator (ISOLDE) to produce radioactive ion beams. PS beams are used to produce neutrons for the n-ToF experiment, antiprotons for the Antiproton Decelerator (AD), and are extracted for other fixed-target experiments. SPS beams are also sent to fixed-target experiments and to a dedicated beam line for plasma wakefield acceleration in the AWAKE experiment [7].

The LHC and its injectors are presently involved in two projects: the High Luminosity Large Hadron Collider (HL-LHC) and the LHC Injectors Upgrade (LIU). Several upgrade options are currently being studied and planned, in view of increasing the research capabilities of CERN. The HL-LHC is a novel configuration of the Large Hadron Collider, aiming at increasing the luminosity by a factor of 5 or more above the nominal LHC design [8]. That can be achieved by increasing the bunch intensity by about a factor of 2 and reducing the transverse beam size at the collision points. In order to reach the beam parameters necessary for the HL-LHC, the LIU project is dealing with an upgrade of the LHC injectors [9]. Solutions are investigated and implemented in all the injector complex to overcome present limitations and reliably reach this new level of performance.

1.2 Lorentz force

In a synchrotron, a charged particle beam is guided and accelerated by electromagnetic fields. The electromagnetic force $\vec{F}$ exerted by an electric field $\vec{E}$ and a magnetic field $\vec{B}$ on a particle of charge q moving at velocity $\vec{v} = \vec{\beta}c$ is described by the Lorentz equation:

$$\vec{F} = \frac{d\vec{p}}{dt} = q(\vec{E} + \vec{v} \wedge \vec{B}) \tag{1.1}$$

As one can infer from Eq. 1.1, a longitudinal electric field can accelerate charged particles increasing their momentum $\vec{p}$ [10].
Often, the electric field is provided by the Radio Frequency (RF) cavities. Particles are accelerated by means of an alternating electric field generated between two electrodes in the cavity gap, whose polarity is synchronized with the particles passage. An electrostatic field can also be used for acceleration, but it is suitable only for low-energy accelerators, due to limitations from the field breakdown and accelerator length.
According to Eq. 1.1, a particle beam can be guided, confined and focused in a circular closed path by applying an orthogonal magnetic field to its trajectory. In fact, dipole magnets are generally used to bend the particles and to keep them in a closed trajectory, while quadrupole magnets are used to focus the beam in the transverse plane.
The stability of the trajectory requires the magnetic component of the Lorentz force experienced by a particle to be equal in magnitude and opposite in direction to the centrifugal force F_c:

$$F_c = m\frac{v^2}{\rho} \tag{1.2}$$

where m is the particle mass and ρ is the bending radius.
Consequently, from Eqs. 1.1 and 1.2, the bending radius ρ obeys to the relation:

$$\frac{p}{q} = B\rho, \tag{1.3}$$

with p being the particle momentum. Equation 1.3 defines the *magnetic rigidity*, which establishes the relationship between the magnetic field and the bending radius.

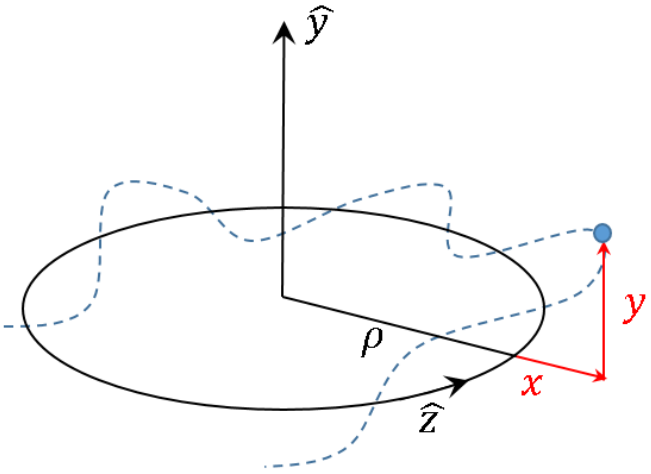

Figure 1.2: Cartesian coordinate system describing the particle motion in a synchrotron.

When the particle beam is being accelerated, its energy level gets higher and higher. As a consequence the magnetic field must be synchronized with the accelerating electric field in order to keep particles on a closed circular trajectory.
For the beam dynamics description, we consider the Cartesian coordinate system ($\vec{x}$, $\vec{y}$, $\vec{z}$) presented in Fig. 1.2, moving with a reference particle q. x,y are defined as betatron coordinates and indicate the position of the particle in the transverse plane, while z expresses the motion in the longitudinal direction.

In the following, since the major attention in this work is posed on the longitudinal motion of particles, the tools for particles acceleration and the longitudinal dynamics are presented.

1.3 Accelerating cavities

Since there are many different types of accelerators, a variety of RF cavities exist, optimized for different purposes and with different abilities. They can be classified according to the electromagnetic wave characteristics (standing-wave cavities or traveling-wave structures) and the cavity material (normal-conducting vs super-

conducting). The choice of the cavity type depends on many factors, such as the required voltage, the frequency, the power, fabrication and operation costs, space constraints, etc [11].
The focusing in the longitudinal plane, as well as the acceleration, is obtained by the longitudinal component of the electric field in the RF cavities, which is applied across isolated gaps in the vacuum chamber.

1.3.1 Characterization of a cavity

The electromagnetic fields in the cavity are excited via external coupling. An external power source is usually coupled to the cavity by an aperture, a wire probe or a loop. The electric field $\mathcal{E}_z$ in the RF cavity gap can be expressed as follows:

$$\mathcal{E}_z(t) = \mathcal{E}_0 \sin(\omega_{rf} t + \Phi) \tag{1.4}$$

where $\mathcal{E}_0$ is the peak amplitude of the RF field in the cavity gap, ω_{rf} is the frequency of the RF source and Φ is the RF phase seen by the particle crossing the middle of the accelerating cavity gap [12] [2]. During the passage through the RF cavity gap of length g the energy gained by the particle is:

$$\Delta E = q \int_{-\frac{g}{2}}^{\frac{g}{2}} \mathcal{E}_z dz = q \int_{-\frac{g}{2}}^{\frac{g}{2}} \mathcal{E}_0 \sin\left(\frac{\omega_{rf}}{\beta c} z + \Phi\right) dz = q\mathcal{E}_0 g T \sin\Phi \tag{1.5}$$

where T is represents the transit-time factor, defined as:

$$T = \frac{\sin\frac{\omega_{rf} g}{2\beta c}}{\frac{\omega_{rf} g}{2\beta c}} \tag{1.6}$$

It quantifies the reduction of energy gain due to the fact that the particle travels with a finite velocity in an electric field with a sinusoidal time variation. The transit-time factor varies between 0 and 1. Since $\Delta E = q V_{acc} T$, the accelerating voltage V_{acc} across the gap of the RF cavity can be expressed as:

$$V_{acc} = \mathcal{E}_0 g T. \tag{1.7}$$

The beam-cavity interaction can be described by using the equivalent model depicted in Fig. 1.3. The cavity fundamental mode interacts with the beam current just like a parallel $R - L - C$ lumped resonator.

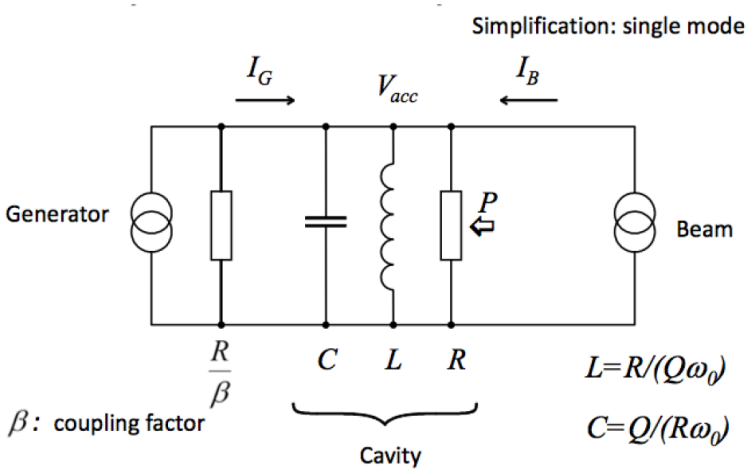

Figure 1.3: Equivalent resonant circuit of a cavity.

Since the real cavities are lossy, due to surface currents that cause energy dissipation, a certain amount of RF power should be provided from the outside to compensate for these losses, keeping the accelerating field at the desired level [13], [14].
The quality factor characterizes the RF losses in the cavity and is defined as the ratio of the stored energy in the cavity and the power dissipated on the cavity per cycle. It is hence an indicator of the efficiency of a resonator:

$$Q = \frac{\omega_0 W}{P_{loss}} \tag{1.8}$$

where $\omega_0 = 1/\sqrt{LC}$ is the resonant frequency of the cavity, W is the energy stored in the cavity and P_{loss} is the power lost in the cavity walls. P_{loss} is equally the power that will have to be fed into the cavity, in order to keep the stored energy at a constant value W. It is clear that Q is inversely proportional to the needed power to compensate for cavity losses [15]. Additionally, one of the most important parameters characterizing the cavity accelerating modes is the shunt impedance R.

It relates P_{loss} and the gap voltage V_{acc}, as follows:

$$R = \frac{|V_{acc}|^2}{2P_{loss}} \tag{1.9}$$

Traditionally, the shunt impedance is the quantity to optimize for minimizing the required power to provide a chosen gap voltage. The square of the accelerating voltage results proportional to the stored energy and allows defining another important parameter of a cavity, the ratio R/Q:

$$\frac{R}{Q} = \frac{|V_{acc}|^2}{2\omega_0 W} \tag{1.10}$$

It is worth noting that this ratio is independent of the power dissipation and is a qualification parameter of the cavity geometrical design.

1.4 Synchrotron oscillations

A synchrotron is a circular accelerator where the nominal particle trajectory is kept at a constant physical radius by variations of both the magnetic field and the radio frequency, in order to follow the energy variation [10].
The radio frequency needs to be synchronous to the revolution frequency. To achieve this synchronism, the RF frequency ω_{rf} is set up to be an integer multiple of the revolution frequency ω_0:

$$\omega_{rf} = h\omega_0 \tag{1.11}$$

where h is called the *harmonic number*. In these conditions, a particle of nominal energy circulating on the nominal trajectory will always experience the same RF phase Φ_s when passing the RF gap. This particle is denoted as the *synchronous particle* and the phase Φ_s associated to it, the *synchronous phase*. Hence, the harmonic number defines the number of stable synchronous particle. They are equidistantly spaced around the circumference of the accelerator. All synchronous particles will have the same nominal energy and will follow the nominal trajectory.
During the acceleration in a synchrotron, the energy of the synchronous particle

increases and so does the revolution frequency (unless particles are ultra relativistic). Clearly, if one wants to keep the accelerated particle on the same trajectory, the magnetic field must vary with time. The time derivative of the momentum $p = qB\rho$, for a constant bending radius ρ, yields to:

$$\frac{\mathrm{d}p}{\mathrm{d}t} = q\rho\dot{B} \tag{1.12}$$

For one turn in the synchrotron, this results in:

$$(\Delta p)_{turn} = q\rho\dot{B}T_0 = \frac{2\pi q\rho R\dot{B}}{v}, \tag{1.13}$$

where T_0 is the revolution period, $R = L/2\pi$ the machine physical radius and L is the circumference of the accelerator.
Since the particle energy is given by $E^2 = E_0^2 + p^2c^2$, it follows that the energy gain per turn $\Delta E = v\Delta p$ is expressed by:

$$(\Delta E)_{turn} = 2\pi q\rho R\dot{B} = qV_{acc}\sin\Phi_s \tag{1.14}$$

Equation 1.14 shows that the stable phase of the synchronous particle changes during the acceleration as the magnetic field B varies:

$$\sin\Phi_s = \frac{2\pi\rho R\dot{B}}{V_{acc}} \tag{1.15}$$

Moreover, as mentioned previously, the radio frequency f_{rf} has to change with the revolution frequency f_0 and it will increase during acceleration as:

$$f_0 = \frac{f_{rf}}{h} = \frac{v(t)}{2\pi R} = \frac{1}{2\pi}\frac{qc^2}{E(t)}\frac{\rho}{R}B(t) \tag{1.16}$$

Expressing the particle rest mass $E_0 = m_0c^2$, the radio frequency must follow the variation of the magnetic field according to:

$$f_0 = \frac{f_{rf}}{h} = \frac{c}{2\pi R}\left\{\frac{B(t)^2}{(m_0c^2/qcp)^2 + B(t)^2}\right\}^{1/2} \tag{1.17}$$

The phase of the RF voltage, when a particle is crossing the RF gap, determines the relative longitudinal position of the particle. For an arbitrary particle, the phase Φ is referred to its deviation from the synchronous particle phase Φ_s:

$$\Phi = \Phi_s + \Delta\Phi. \tag{1.18}$$

In a similar way as for the phase coordinate, the energy E of the arbitrary particle is related to that of the synchronous particle, E_0, as follows:

$$E = E_0 + \Delta E \tag{1.19}$$

The longitudinal phase-space coordinates $\{\Delta\Phi, \Delta E\}$ fully describe the longitudinal motion of the particles.
A synchronous particle circulates on the design orbit, and it is synchronous with f_{rf}. All the other protons in the accelerator will oscillate in energy and in phase around the synchronous particles under the influence of the RF system. This means that instead of being spread uniformly around the circumference of the accelerator the particles get bunched around the synchronous particles in what is called *bunch*.

1.4.1 Dispersion effects and phase stability

If a particle is slightly shifted in momentum with respect to the synchronous one, it will have a different velocity and also a different trajectory and orbit length. The momentum offset is related to the orbit length deviation via the *momentum compaction factor*, α:

$$\alpha = \frac{\frac{\Delta L}{L}}{\frac{\Delta p}{p}} \tag{1.20}$$

Similarly, the revolution frequency changes with the momentum according to:

$$\eta = \frac{\frac{\Delta f_0}{f_0}}{\frac{\Delta p}{p}} \tag{1.21}$$

where η is defined as *slip factor*.
These two aforementioned parameters are related according to:

$$\eta = \left(\frac{1}{\gamma^2} - \alpha \right) \tag{1.22}$$

with $\gamma = E/mc^2$ being the relativistic gamma. η can be either positive or negative, depending on the particle energy. The energy at which the sign changes is the transition energy γ_{tr}:

$$\gamma_{tr} = \sqrt{\frac{1}{\alpha}} \tag{1.23}$$

The synchronous RF phase Φ_s, at which the synchronous particles passes the RF cavities on every turn, must be chosen depending on the particle relativistic γ, being below or above the transition. Two different regimes can, hence, be identified:

- $\gamma < \gamma_{tr}$ $(\eta > 0)$
  In this case, $0 < \Phi_s < \pi/2$ ensures the bunch stability, that corresponds to the particle which is on the positive slope of the RF voltage $V(t) = V_{rf} \sin \Phi(t)$.
  Below transition an increase in energy determines an increase in revolution frequency, since the velocity increase is the dominating effect.
  A particle which reaches the RF earlier with respect to the synchronous one will gain less energy and, since its velocity will be smaller, in the next turn it will get closer to it. The effect is opposite for particles which arrive later than the reference particle: they will gain more energy, reducing their delay compared to the equilibrium particle in the following turn.

- $\gamma > \gamma_{tr}$ $(\eta < 0)$
  In this other case, above transition, a particle that will arrives earlier will get more energy and, since it will follows a larger orbit ($v \sim c$), the revolution time will increase. Hence, in the next turn it will arrive later, closer to the synchronous particle. In this regime the stable motion occurs on the negative slope of the RF voltage, or for $\frac{\pi}{2} < \Phi_s < \pi$.

Particles with a small deviation from the synchronous one perform stable oscillations around the nominal particle, following an elliptical path in the phase space, while for larger energy deviations these circles get flattered into a pseudo-ellipse. These

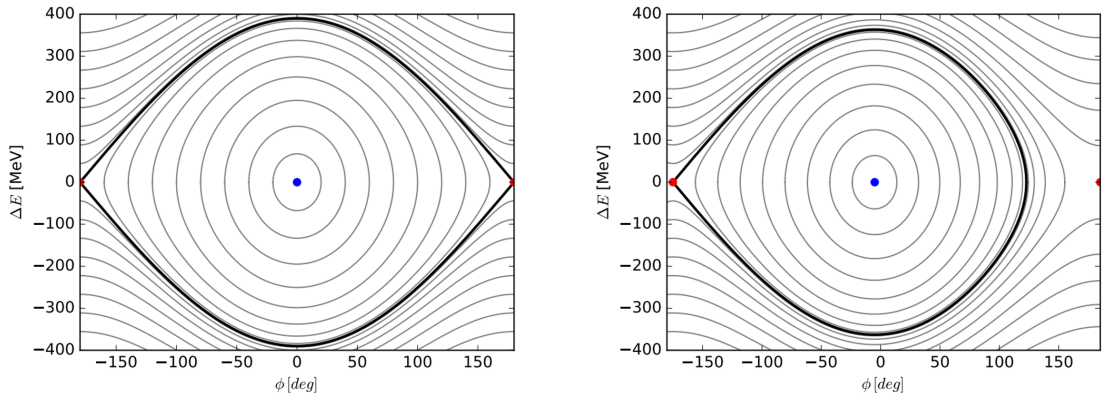

(a) Stationary bucket

(b) Accelerating bucket

Figure 1.4: Particle trajectories in phase space in the stationary case (left) and during acceleration (right). The solid black line shows the separatrix of the RF bucket. Blue points are stable fixed points and red points are unstable fixed points [16].

oscillations are called *synchrotron oscillations*. The stable phase space region is called *bucket*, while the boundary in the phase space is referred to as the *separatrix*, which separates stable and unstable oscillations. Acceleration is only possible for particles inside the stable region. Particle injected at a point outside the separatrix will get lost. Bunches of particles occupy buckets, but not all buckets need be occupied. Batches (or bunch trains) are groups of bunches formed in specific patterns, often from upstream accelerators. The area of the stable region of the phase space filled by the particles of a bunch is called the *longitudinal emittance*.

The phase extension of the bucket is maximum when there is no acceleration and $\sin \Phi_s = 0$, so that $\Phi_s = 0$ or π. This *stationaty bucket* spans the whole range of Φ from $-\pi$ to π (Fig. 1.4a). As the synchronous phase gets closer to $\pi/2$, the size of the bucket shrinks, both in phase and in energy (Fig. 1.4b).

The equation of motion in the longitudinal plane of a particle with a phase $\Phi = \Phi_s + \Delta\Phi$, can be written as:

$$\Phi'' + \frac{{\omega_{s0}}^2}{\cos \Phi_s} (\sin \Phi - \sin \Phi_s) = 0 \tag{1.24}$$

where:

$$\omega_{s0}^2 = \frac{\omega_{rs}^2 h\eta e\hat{V}}{2\pi R_s p_s} cos\Phi_s \tag{1.25}$$

is the synchrotron angular frequency with h being the harmonic number, R_s and ω_{rs} being respectively the synchronous orbit radius and the revolution frequency, p_s being the particle momentum.
If the particle presents a small deviation $\Delta\Phi$ from the synchronous phase, the corresponding motion reduces to a harmonic oscillation:

$$\Phi'' + \omega_{s0}^2 \Delta\Phi = 0 \tag{1.26}$$

Stability occurs when $\omega_{s0} \propto \eta \cos\Phi_s$ is real and so ω_{s0} is positive (Fig. 1.5).

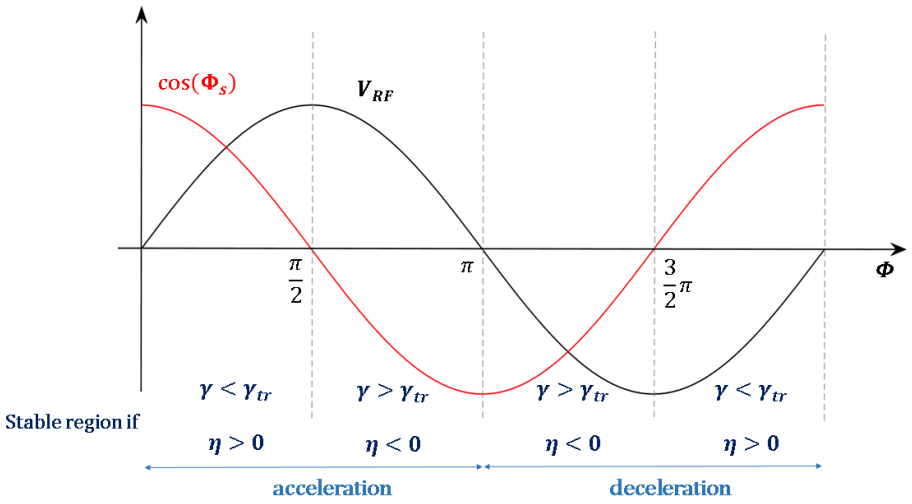

Figure 1.5: Phase stability in a synchrotron for small amplitude oscillations [10].

1.5 Wakefields and beam loading

The motion of a single accelerator particle is established by the electromagnetic fields, mainly generated by the RF systems and the magnets. However, in addition to these external fields, particles are affected by self-fields, generated by the interaction with

other particles or with the environment. These fields are called wakefields of the beam and they are the main source of longitudinal and transverse beam instabilities.
Let's consider a charge q, circulating in a synchrotron. When crossing a vacuum pipe with resistive walls or variation in chamber geometry or material, it generates an image current with opposite sign, that flows on the vacuum chamber wall following the beam (Fig. 1.6).

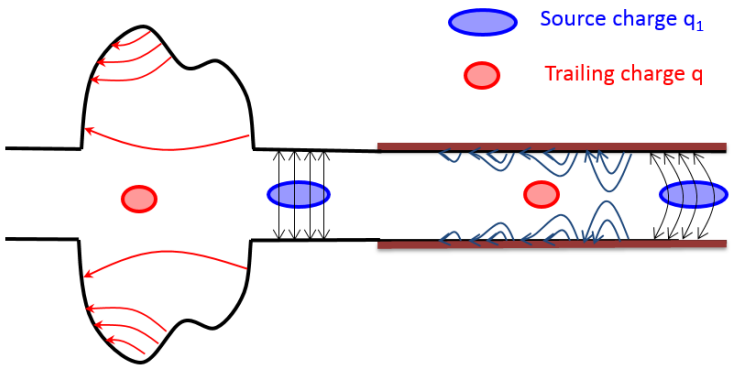

Figure 1.6: EM wakefields due a discontinuity of the vacuum chamber (red) and resistive walls (blue). A leading charge q_1 loses part of its energy and generates a EM wakefield that acts behind on a test charge q.

Turn by turn, the beam loses part of its energy generating these EM (wake) field that acts back on the beam itself. These wakes could cause a significant modification particles motion dynamics. Intrinsically, an accelerator cavity can be considered, by design, such a pipe variation and, since it has a finite conductivity, it presents an impedance Z to the wall currents. When a bunch of current I_B leaves the cavity, a beam induced voltage V_B fills the cavity. The latter reads:

$$V_B = -Z \cdot I_B, \tag{1.27}$$

where the minus sign indicates that the induced voltage leads to an energy loss [17].

1.5.1 Definition of wakefield

Wakefields may have both a longitudinal component, responsible of energy losses, and a transverse one, which causes deflection of particle trajectory.

We can determine the effect of a source charge q_1, moving with constant velocity $v = \beta c$, on a test charge moving behind it. z_1 is the longitudinal position and r_1 is the transverse position vector of the particle [18].

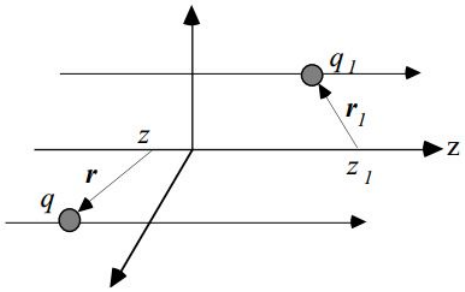

Figure 1.7: Main coordinates system.

Let E and B be the electromagnetic fields produced by q_1 and acting on the test charge q, or trailing charge, at a given position r, z. The leading charge generates a force, with both longitudinal and transverse components, acting on the trailing charge:

$$F(r, z, r_1, z_1; t) = q[E(r, z, r_1, z_1; t) + v \times B(r, z, r_1, z_1; t)] = F_{\parallel} + F_{\perp} \tag{1.28}$$

Since we are mainly interested in the beam motion in the longitudinal plane, let's neglect the effects experienced by the particle in the transverse plane. A detailed analysis could be found in [19].
Considering τ the time delay between the leading and trailing charges, the energy lost by the leading charge q_1, at the time $t = z_1/v$, due to the resistive walls and to the discontinuities of the pipe, is:

$$U_{11}(r_1) = -\int_{-\infty}^{\infty} F_{\parallel}(r_1, z_1, r_1, z_1; t)\, dz \qquad [J] \tag{1.29}$$

The field produced by q_1 acts back on the trailing charge at the time $t = z_1/v + \tau$, changing its energy by U_{21}:

$$U_{21}(r, r_1; \tau) = -\int_{-\infty}^{\infty} F_{\parallel}(r, z, r_1, z_1; t)\, dz \qquad [J] \tag{1.30}$$

Depending on τ, U_{21} can be positive (energy loss) or negative (energy gain).

From these quantities we can define the longitudinal *loss factor*:

$$k_{\parallel}(r_1) = \frac{U_1(r_1)}{{q_1}^2} \qquad [V/C] \tag{1.31}$$

that is the energy lost by q_1 per unit charge squared.
The longitudinal *wake function* $w_{\parallel}(r, r_1; \tau)$ is the energy lost by the test charge q per unit of both charges:

$$w_{\parallel}(r, r_1; \tau) = \frac{U_{21}(r, r_1; \tau)}{q q_1} \qquad [V/C] \tag{1.32}$$

A real accelerator has a finite length and includes transitions in geometry and various devices such as kickers, RF cavities, diagnostic components that can perturb the field. A good evaluation of the wakefields can be done by assuming that the fields are confined in a limited region. Hence, the integration can be done over a period L of a periodic structure of the vacuum chamber, or in the circular accelerator case, over the entire circumference.

1.5.2 Wakefield of a bunch

In the following, the wakefields properties and definition are generalized to the case of a bunch of particles.
Let be q_1 the total charge of a source bunch with a longitudinal time distribution function $I_B(\tau)$:

$$q_1 = \int_{-\infty}^{\infty} I_B(\tau)\, d\tau \tag{1.33}$$

The longitudinal *wake potential* of a bunch distribution is the convolution of the single particle wake function with the bunch distribution. The bunch is splitted into infinitesimal slices and the energy lost by a trailing charge q travelling across the slice at τ' reads:

$$dU(r, \tau - \tau') = q I_B(\tau') w_{\parallel}(r, \tau - \tau')\, d\tau' \tag{1.34}$$

The contribution of the entire bunch distribution is obtained by integration and the

wake potential reads:

$$W_{\parallel}(r;\tau) = \frac{U(r,\tau)}{q_1 q} = \frac{1}{q_1}\int_{-\infty}^{\infty} I_B(\tau') w_{\parallel}(r,\tau-\tau')\, d\tau' \tag{1.35}$$

1.6 Coupling impedance

The wakefields induce instabilities which are resonant phenomena. For this reason, it is useful to analyse the spectrum of the wake functions. The Fourier transform of the wake function is known as the *coupling impedance*, since it is measured in Ohms. The longitudinal coupling impedance reads:

$$Z_{\parallel}(r,r_1;\omega) = \int_{-\infty}^{\infty} w_{\parallel}(r,r_1;\tau) e^{-j\omega\tau}\, d\tau \tag{1.36}$$

Sources of coupling impedance can be any discontinuity of vacuum chamber walls and finite conductivity of the vacuum chamber (the resistive wall impedance) in the accelerators.

The coupling impedance can be distinguished in broadband impedance and narrow-band impedance, according to the effective range of a wakefield. Figure 1.8 represents a typical real part of an accelerator cavity impedance. Below the cavity cut-off, the impedance spectrum is represented by sharp peaks, representing the fundamental mode and Higher Order Modes (HOMs) of the RF cavity. Above the cut-off frequency the broadband impedance modes have a low-Q and a broader spectrum; in addition, its associated wake lasts for a relatively short time. Typically this type of wakefield can only affect particles in the same bunch and does not effect particles in the trailing bunches. Contrarily, a narrowband impedance corresponds to a long range wake effect: the wakefield lasts longer than the time separation between bunches, thus trailing bunches can interact with wakes from leading bunches triggering multi-bunch instabilities.

The longitudinal cavity impedance related to a single cavity mode wakefield can be defined, referring to the $R-L-C$ circuit model approximation, described in Sec. 1.3.1.

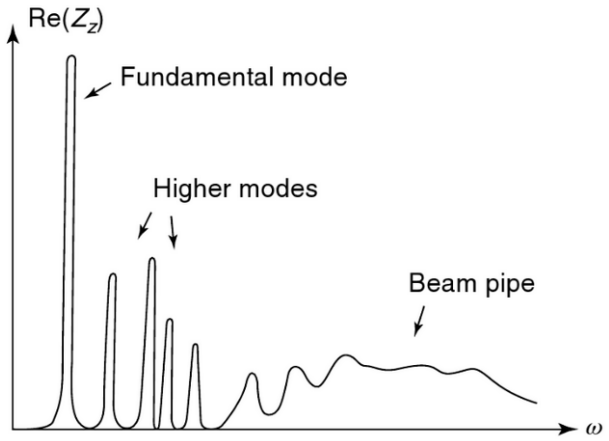

Figure 1.8: Typical frequency spectrum of the real part of an accelerator cavity impedance.

The longitudinal impedance reads:

$$Z(\omega) = \frac{R}{1 + jQ\left(\frac{\omega}{\omega_0} - \frac{\omega_0}{\omega}\right)} \tag{1.37}$$

with R being the shunt impedance and $\omega_0 = 1/\sqrt{LC}$ the resonant frequency of the circuit representing the considered cavity mode. The formula takes into account that the cavity resonant frequency ω_0 is not necessarily equal to the driving frequency of the generator.
The cavity wake potential can be calculated as the Fourier anti-transform of this cavity impedance.

1.7 Beam-cavity interaction

Beam loading is the conventional term used to indicate the effect induced by the beam passage in an RF cavity. Cavities are fed by RF power amplifiers and the cavity-amplifier system is generally optimized for providing the maximum acceleration with the minimum RF input power. As a consequence, the cavity impedance is large, while the current from RF generator is minimized [20].

In addition, the beam-induced voltage can lead to single or multi-bunch instabilities, in case a circulating bunch sees the voltage induced by the previous bunches. Since this voltage is proportional to the cavity impedance, the latter has to be minimized.

1.7.1 Beam loading

If the distance between two successive bunches is large compared to the filling time of the cavity, the field induced by a leading bunch does not affect the passage of the following bunch. The latter only experiences an accelerating RF voltage (Fig. 1.9 a) [21]. The bunch passage in the cavity excites a field (Fig. 1.9 b) exponentially decaying and oscillating at the cavity resonant frequency and, as a consequence, a distorted field distribution with decreased amplitude remains in the cavity (Fig. 1.9 c).

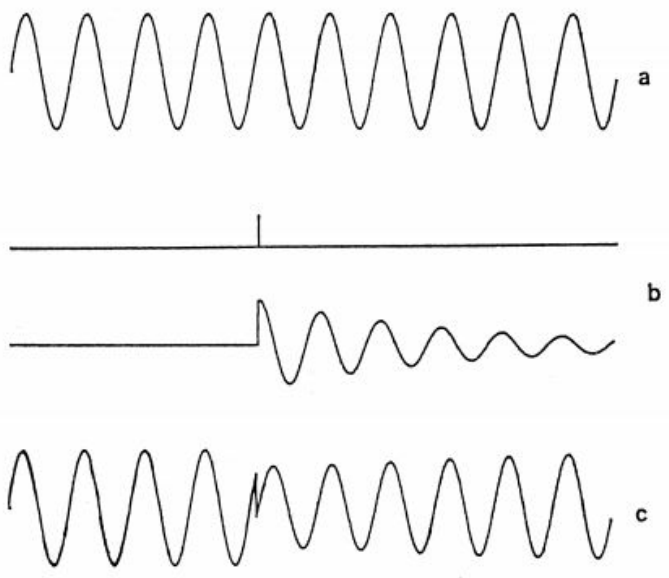

Figure 1.9: Effect of a bunch passage in a cavity [21].

Let $\vec{V_g}$ be the voltage provided by the driving generator and $\vec{I_B}$ be the fundamental component of the beam current. The bunch passage induces a decelerating voltage $\vec{V_B}$. The total cavity voltage is:

$$\vec{V_t} = \vec{V_G} + \vec{V_B} = Z_G\vec{I_G} + Z_B\vec{I_B} \tag{1.38}$$

Around the resonance frequency ω_0 the cavity can be modelled as an $R-L-C$ parallel circuit in Fig. 1.10. The total cavity current is:

$$\vec{I_t} = \vec{I_G} + \vec{I_B} \tag{1.39}$$

Since $Z_B = Z_G = Z_{cav}$ in the simplified circuit of Fig. 1.10, the total voltage reads:

$$V_t = Z_{cav}(I_G + I_B) \tag{1.40}$$

According to Eq. 1.37, the cavity impedance can be expressed as:

$$Z_{cav}(\omega) = \frac{R}{1 + jQ\left(\frac{\omega}{\omega_0} - \frac{\omega_0}{\omega}\right)} = R\cos\psi e^{-i\psi} \tag{1.41}$$

where ψ is the detuning angle with:

$$\tan\psi = Q\left(\frac{\omega}{\omega_0} - \frac{\omega_0}{\omega}\right) \tag{1.42}$$

If $\frac{\omega_0-\omega}{\omega_0} = \frac{\Delta\omega}{\omega_0} << 1$:

$$\tan\psi = 2Q\frac{\Delta\omega}{\omega_0} \tag{1.43}$$

In the vector representation in Fig. 1.10, φ_B is the stable phase angle ($\varphi_B > 0 =$ acceleration), ψ is the detuning angle, i.e the phase angle of the generator plus the cavity impedance, and φ_L is the *loading phase angle*, i.e. the equivalent impedance angle as observed by the RF source, with no beam loading [22] [23].
Since the total current is the vector sum of I_G and I_B, using Eq. 1.38, we can write:

$$\vec{I_t} = \frac{1}{Z_{cav}}V = V\left[\frac{1}{R} + j\left(C\omega - \frac{1}{L\omega}\right)\right] \tag{1.44}$$

The contribution of the beam induced voltage affects the reactive component of the cavity impedance, causing a frequency shift ($\omega_0 \neq \omega_{rf}$), therefore preventing the maximum power transfer.
I_G must compensate I_B to keep the modulus of the total accelerating voltage V_t at the desired value (desired bucket area). In addition, detuning is necessary to minimize

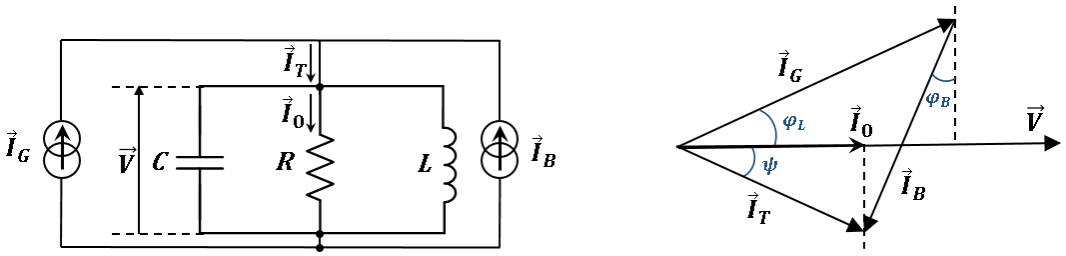

Figure 1.10: Equivalent circuit and steady-state vector diagram of the RF currents in a cavity.

the requested RF power and to cancel out the reactive component introduced by the beam loading.

We are considering the case of the stationary beam loading and focusing our attention on the line of the beam frequency spectrum corresponding to the RF frequency ω_{rf}. In Fig. 1.10, $\vec{I}_0 = \vec{V}/R$ is the minimum current needed to develop a voltage V when the cavity is tuned. Static beam loading is quantified using the beam loading parameter Y defined by:

$$Y = \frac{I_B}{I_0} \tag{1.45}$$

Transient beam loading can occur when the filling time T_f of the cavity is not very large compared with the time interval T_b between two bunches or when the ring is not filled uniformly. In this case the spectral components of the beam current extend over a wide frequency range where the cavity impedance is not negligible.

One can say that the frequency spectrum of the voltage induced by the beam consists in a line at the carrier frequency f_{rf} (stationary beam loading) and sidebands at frequency multiples of f_{rev} (transient beam loading) [24].

The beam loading decreases moving away from the carrier frequency, hence a compensation is needed at the frequencies:

$$f = f_{rf} \pm n f_{rev} \tag{1.46}$$

In addition, a multi-bunch beam can be affected by instabilities due to the interaction between bunches. The bunches can start longitudinal oscillation at the synchrotron

frequency f_s. The presence of dipolar or higher order motion makes the beam current periodic of f_{rev} with a phase modulation at f_s. These oscillations will sample the cavity impedance at the frequencies:

$$f = f_{rf} \pm n f_{rev} \pm m f_s \tag{1.47}$$

1.7.2 Wide-band feedback

Many techniques exist for compensating the beam loading effect [20]. Some, such as the 1-turn and the coupled-bunch feedback, provide a reduction of the impedance acting at fixed harmonics; others, such as the wide-band feedback (also named *fast feedback*), compensate for the beam loading at the main RF frequency and lowers the side bands of the cavity impedance spectrum that falls in the cavity filter action.
The wide-band feedback consists into enclosing the cavity and its driving amplifier in a high gain loop, as shown in Fig. 1.11. Part of the cavity voltage is re-injected back and added to the RF signal delivered by the amplifier driving the cavity. This allows to reduce the cavity impedance seen by the beam by a factor equal to the loop gain.

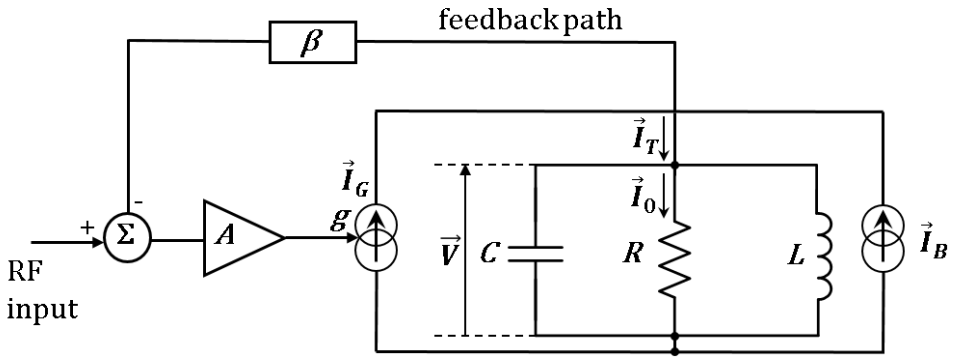

Figure 1.11: Block diagram of the wideband beam loading compensation.

In the circuit shown in Fig. 1.11, we can also distinguish a first amplification stage A followed by a voltage-controlled current source, characterized by a trans-conductance g and providing the necessary RF current to the cavity. I_B is the beam current circulating in the gap, while I_0 is the current flowing in the cavity resistance R at the cavity resonance ω_0. The equivalent cavity impedance as seen by the beam is reduced

according to:

$$Z_{eq}(\omega) = \frac{Z_{cav}}{1 + G_L} \tag{1.48}$$

where G_L is the loop gain. It is maximum at the cavity resonance:

$$G_L(\omega_0) = Ag\beta R \tag{1.49}$$

where AgR is the open loop gain of the amplification chain, and β is the feedback attenuation. The current I_0 can then be expressed as:

$$I_0{}' = I_0(1 + G_L(\omega_0)) \tag{1.50}$$

Consequently, the relative beam loading parameter Y is reduced according to:

$$Y' = \frac{Y}{1 + G_L} \tag{1.51}$$

The main limitation of the fast feedback compensation is the loop delay T which is introduced by cables and electronics.

Near its resonant frequency, the cavity impedance is expressed by:

$$Z(\omega) = \frac{R}{1 + j2Q\frac{\Delta\omega}{\omega_0}} \tag{1.52}$$

where Q is the quality factor and $\Delta\omega = \omega - \omega_0$.
If we consider that the cavity is detuned by $\Delta\omega$ from the resonant frequency, outside the $\omega_{0/}Q_0$ bandwidth the cavity impedance is purely reactive:

$$Z(\omega) = \frac{R}{j2Q\frac{\Delta\omega}{\omega_0}} \tag{1.53}$$

At these frequencies the cavity introduces a $-\frac{\pi}{2}$ phase shift. To provide the system stability, the loop gain module must be less than 1 when the phase is $-\pi$. In order to keep a reasonable phase margin of $\pi/4$ the loop gain must be less than 1 when the delay T introduce an extra $-\pi/4$ phase shift.

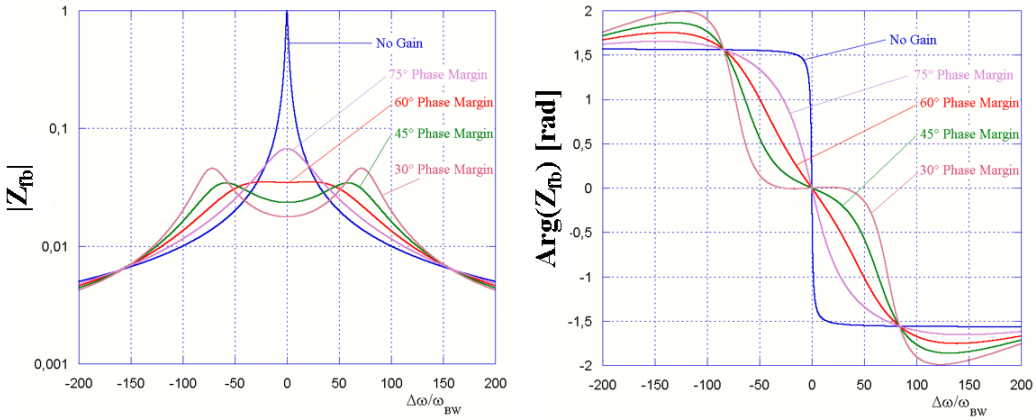

Figure 1.12: Modulus and phase of the feedback impedance. The figures show the distortion due to the reduction of the stability limits of the feedback system [14].

Since $\Delta\omega = \frac{\Delta\varphi}{T}$, we get [24]:

$$Ag\beta|Z(\frac{\pi}{4T})| \leq 1 \tag{1.54}$$

The maximum loop gain and the minimum impedance at the resonance are:

$$G_{L_{max}} = \frac{\pi Q}{2\omega_0 T} \tag{1.55}$$

$$R_{eq_{min}} = \frac{2\omega_R}{\pi}\frac{R}{Q}T \tag{1.56}$$

If the loop gain is increased up to the stability limits, the shape of the cavity impedance spectrum starts to deviate from the classical bell shaped curve, presenting an overshoot on the edges of the pass-band as clearly shown in Fig. 1.12.

Chapter 2

The CERN Proton Synchrotron

The CERN Proton Synchrotron (PS) is a part of the LHC injector chain. It plays a key role in the accelerator complex and supplies beams for almost all important experiments. The final design of the CERN PS was adopted in 1954 and the beam was accelerated up to a kinetic energy 24 GeV in 1959. At the time, the linear accelerator LINAC 1 was the injector of the PS with 50 MeV proton beams, until the LINAC 2 and the PSB were built and commissioned [25].
Today the PS accelerator complex includes LINAC 2 and LINAC 3, PSB, LEIR, the Antiproton Deccelerator (AD) and the PS ring, as sketched in Fig. 2.1.

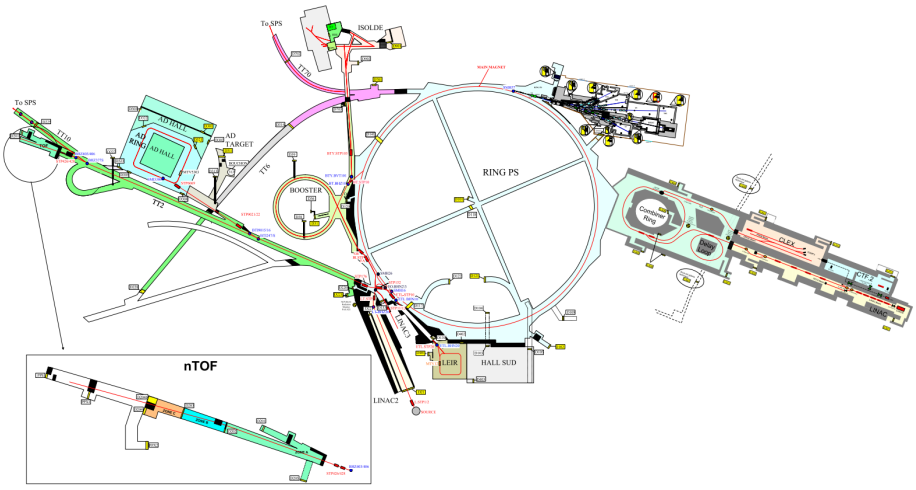

Figure 2.1: The PS complex [25].

In the Long Shutdown 2 (LS2) planned in 2019-2020, a new 160 MeV H^- linear accelerator, the LINAC 4, is expected to replace LINAC 2 as injector to PSB, aiming at an increase of the PSB beam brightness by a factor of 2 [9].
The PS is a ring of 628 m circumference made of 100 main magnets and straight sections. Accelerating cavities, beam diagnostic devices and injection and extraction elements are installed in straight sections, that are placed between two subsequent magnet units.
The accelerator operates at energies up to 25 GeV. In addition to protons, the PS has been used to accelerate a variety of particles: alpha particles (helium nuclei), oxygen and sulphur nuclei, electrons, positrons and antiprotons (Fig. 2.2).

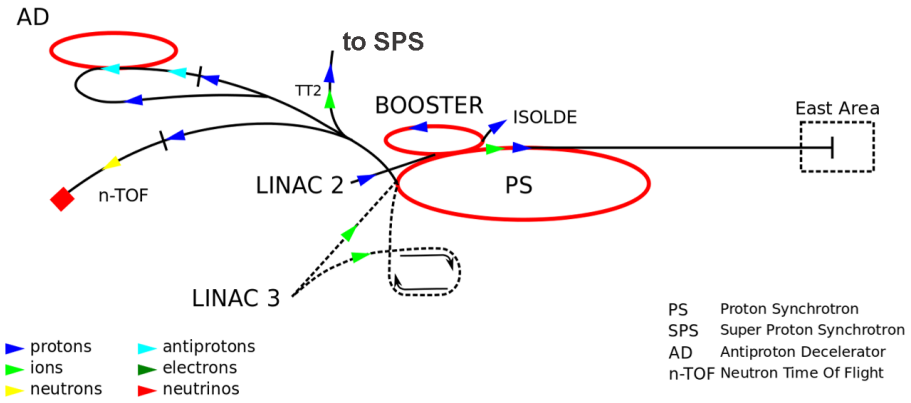

Figure 2.2: Overview of the various types of circulating beams in the PS complex [3].

Nowadays, the proton beams are injected in the PS having the kinetic energy 1.4 GeV, while their extraction energy varies according to the beam user.
The proton beam intensity delivered by the PS has continuously increased over the years and upgrade projects are presently ongoing planning to push forward the performance of the accelerator and increase the number of protons per bunch.

2.1 Beams in the CERN PS

Beams from PS are either delivered to SPS for further acceleration and then used in operation for the LHC, or directly sent to the physics users located in 3 experimental areas:

- n-ToF: it is the CERN's neutron time-of-flight facility, where neutron-nucleus interactions are studied allowing precise measurements of neutron-related processes [26];
- AD: protons from the PS are dumped into a metal target to create high-energy antiprotons, which are then slowed down in the Antiproton Decelerator (AD), where physicists are producing anti-hydrogen atoms to study the properties of antimatter [27];
- the East Area (EA): it consists of several beamlines, where experiments on fixed target take place and where an irradiation facility is active since 2014 [28] [29] [30].

2.1.1 The PS as injector of the LHC

The PS is equipped with several RF systems, 2.8-10, 20, 40, 80 and 200 MHz, which accelerate and perform the necessary RF gymnastics for the LHC-type beam production. Their distribution in the ring is shown in Fig. 2.3.

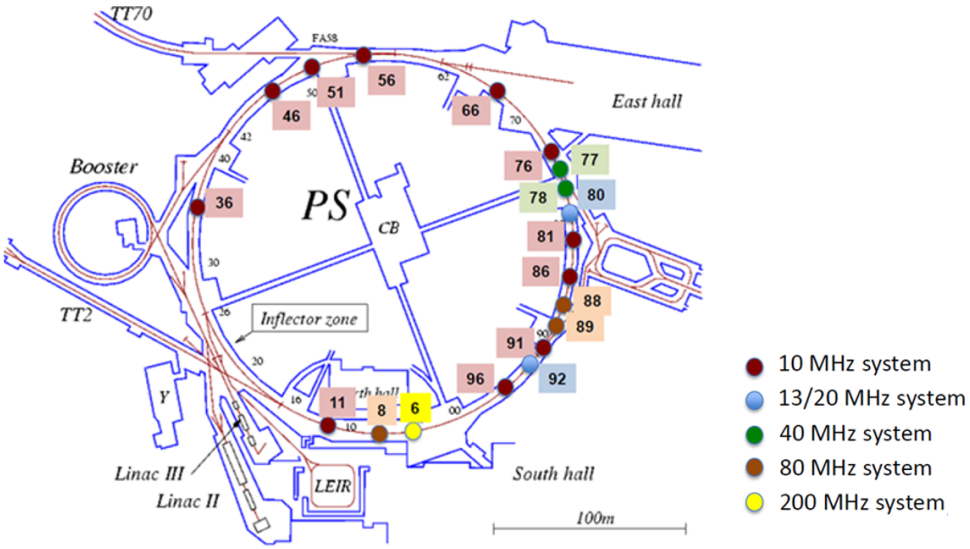

Figure 2.3: Distribution of RF systems in the PS.

The combined use of the 10 MHz system (working on h=7→21) and the 20 MHz system (working on h=42), followed by the 40 MHz system (working on h=84) and

the 80 MHz system (working on h=168) allows to produce the desired beam pattern and filling scheme. Until now, the LHC physics beams with 25, 50 and 75 ns bunch have been produced, however only the 25 ns LHC beam is kept as *nominal* LHC beam for *pp* collisions [31].
According to the production scheme, the transverse emittances of the LHC-type beam is established in the PSB, while the longitudinal structure is the result of very complicated RF gymnastics in the PS. In addition, the beam is cleaned from possible tails in the SPS and the longitudinal and/or the transverse emittances are increased by controlled blow-ups.
LHC-type beams use double-batch injection from PSB to PS. The PSB works at h=1, nonetheless up to 4 bunches per batch can be sent to the PS, since the PSB consists of four superimposed rings. During the first injection, four bunches are sent from the PSB and captured on four consecutive buckets on h=7 in the PS. On the following injection, two more bunches are provided (Fig. 2.6b) [32]. After the second injection, the bunches receive a special longitudinal manipulation by the RF cavities in order to generate the required bunch spacing and numbers.

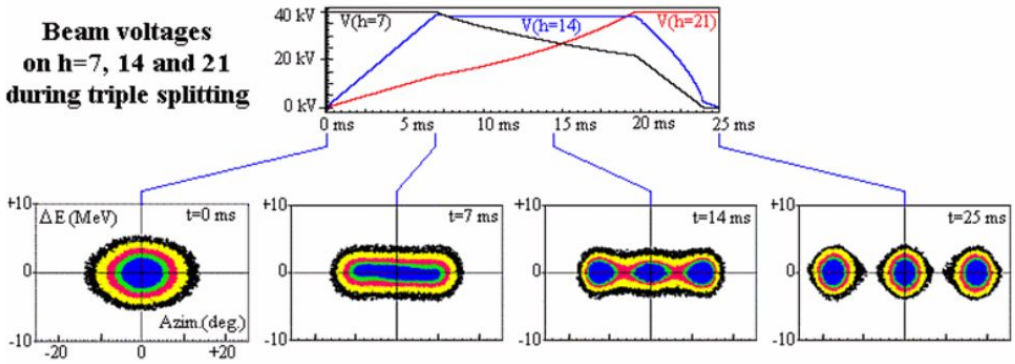

Figure 2.4: Princicle of triple splitting [9].

The bunches are first triple-splitted at flat bottom, with a consequent production of 18 bunches at h=21 (Fig. 2.4) [33]. Triple splitting requires three simultaneous RF harmonics, h=7, h=14 and h=21, which can be provided by the 10 MHz ferrite cavities divided in three different tuning groups. Starting with h=7, the bunch is flattened by the voltage increase on h=14 and h=21 (t = 7 ms in Fig. 2.4). Provided that the rate of change of the voltages is sufficiently slow, the particles of the initial

bunch are gradually captured in the new buckets, whose area growth is generated by the voltage decrease on h=7 and increase on h=21 ($t = 14\,\text{ms}$). Three equal bunches are finally obtained, each of them has the same distribution of particle density as the initial one ($t = 25\,\text{ms}$) [9].

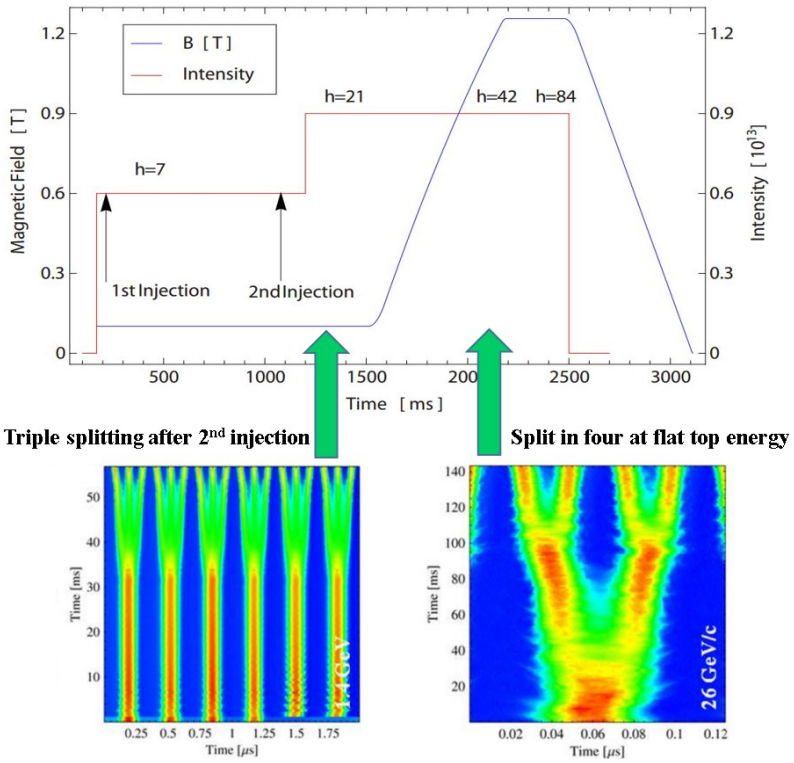

Figure 2.5: Production of the nominal LHC 25 ns beam in the PS. The blue curve is the magnetic field as a function of time, the red is the beam intensity in number of protons as a function of the harmonic number changed by the successive RF gymnastics. In the bottom, triple splitting at 2.5 GeV and double splittings at 25 GeV are shown in the tomoscope plots of longitudinal density. Longitudinal density is colour-coded from blue (no beam) to red (maximum) [9].

After acceleration to 26 GeV/c, two additional double splittings occur at top energy. The final 72 bunches obtained are spaced by 25 ns. During this process, shown in Fig. 2.5, the harmonic number changes again from 21 to 42 and then to 84.

At the end of the splitting process at 25 GeV, bunches are longitudinally rotated by raising quickly, first the 40 MHz (h=84) system, and 180 μs later, the 80 MHz (h=168)

system to full voltage. The resulting bunch is now ready to fit in the 4 ns long SPS bucket. In the following, the main characteristics of some beams circulating in the PS are shown. Table 2.1 summarizes the beam parameters for two high intensity beams n-ToF and AD compared to the nominal LHC beam.

Beam	n-ToF	AD	LHC Nominal
Maximum Intensity [10^{10}]	850	1600	940
Number of bunches	1	4	$6 \rightarrow 72$
Transverse emittance ϵ_H $(1\sigma)[\pi\cdot$ mm·mrad]	12	9	< 2.5
Transverse emittance ϵ_V (1σ) $[\pi\cdot$ mm·mrad]	9	5	< 2.5
Longitudinal emittance ϵ_L[eVs]	1.75	1.8	1.3
Bunch Length at extraction [ns]	27	∼33	< 4.2

Table 2.1: Main parameters of ToF, AD and LHC 25 ns beams [34]. The values of transverse and longitudinal emittances refer to the injected beam.

Figure 2.6 shows the injection process from PSB to PS, in case of an LHC-type beam (a) and n-ToF beam (b). The latter requires only a single batch injection.

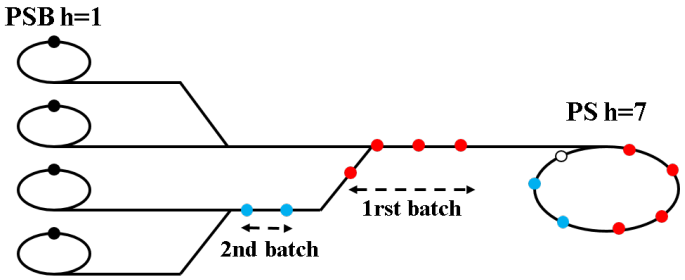

(a) LHC-type beam injection process.

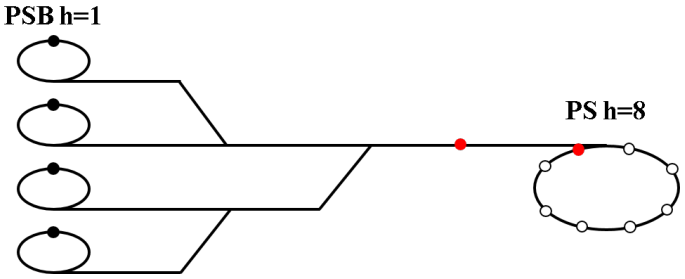

(b) ToF-type beam injection process.

Figure 2.6: Injection scheme from PSB to PS. LHC-type beam requires a double batch injection (4+2), while a single batch is necessary for n-ToF single bunch beams.

2.1.2 Alternative schemes for LHC beam production

Beside the classical production scheme of the LHC-type beam, based on triple splitting at injection energy plus two double splitting on the extraction flat top, ever more complicated RF manipulations have been proposed in the PS machine to increase the brightness of beams in the LHC. [36].
The BCMS (Batch Compression Merging and Splittings) is an alternative scheme used for the production of the LHC physics beam during the 2015 run. The process, shown in Fig. 2.7, can be summarized as follows:

- two batches of four bunches from the PSB are injected in eight PS buckets on h=9;
- the injected bunches are compressed by adiabatically increasing the harmonic number from h=9 to h=14;
- a bunch pair merging ($h = 14 \rightarrow 7$) doubles the intensity per bunch while leaving the transverse emittance unaffected;
- finally, each bunch is triple-split and 12 bunches are accelerated on h=21 to flat-top.

This evolved RF gymnastics is performed at an intermediate kinetic energy of 2.5 GeV to avoid transverse emittance blow up due to space charge and to relax the requirements on the longitudinal emittance at injection.
The resulting 12 bunches are then accelerated to top energy, where splitting in four is exercised to obtain the final 25 ns bunch spacing. Compared to the nominal process, the scheme provides 48 bunches instead 72, increasing the filling time of the LHC and decreasing the maximum number of bunches in the collider. However, the corresponding beam at LHC injection results with a very reduced transverse emittance and can potentially increase luminosity.
The BCMS options is currently under consideration to push further the injector performance to match the High-Luminosity LHC project (HL-LHC) needs, since it adds significant damage risk for the protection devices in the SPS, LHC and transfer lines.

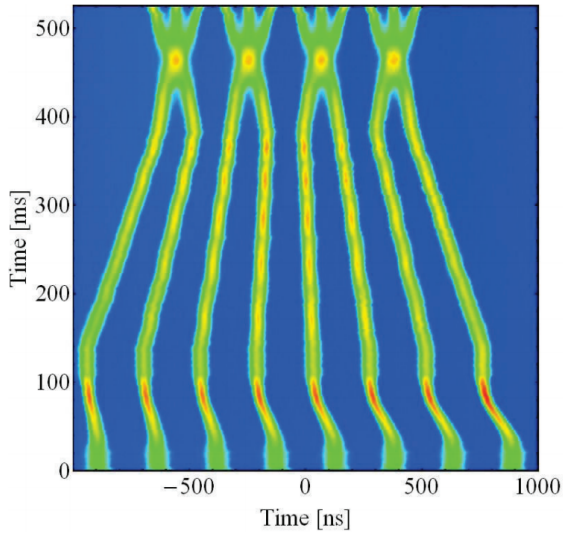

Figure 2.7: Thomoscope view of the RF gymnastic performed for the production of the BCMS scheme at intermediate energy. The batch compression is followed by a bunch merging and a triple splitting [35].

2.2 The LHC Injectors Upgrade project

In the framework of HL-LHC an increased number of collisions per seconds is required to improve the statistical significance of the experimental data. A more powerful LHC, in fact, would provide more accurate measurements of new particles properties and increase our understanding at the energy frontier.
The luminosity L [$\mathrm{cm}^{-2}\mathrm{s}^{-1}$] is a key parameter of a particle collider since it measures the number of collisions per second and cm^2:

$$L = \frac{N_{event}}{\sigma_{event}}, \tag{2.1}$$

with N_{event} being the number of collisions per second and σ_{event} [cm^2] being the cross section for the respective event. An increased number of collisions in the LHC can hence be achieved with an increased luminosity, which can also be defined as follows, relating it to the beam and parameters:

$$L_{LHC} = \left(\frac{\gamma}{4\pi}\frac{1}{\beta^*} f_{rev} F\right) \cdot \left(n_b N_b \cdot \frac{N_b}{\epsilon_n}\right) \tag{2.2}$$

where γ is the relativistic factor, β^* the betatron function at the interaction point, f_{rev} the beam revolution frequency, F a form factor depending upon the geometry of the bunch crossing, n_b the number of bunches per ring, N_b the number of protons per bunch and ϵ_n the normalized transverse beam emittance.
In the second term in brackets, the product $n_b N_b$ represents the beam intensity and N_b/ϵ_n is the beam brightness and they are both greatly fixed by the LHC injectors. High intensity and high brightness beams are key ingredients of high luminosity in the LHC.
The accelerators of the injector complex strongly contribute to the final performance of the Large Hadron Collider (LHC): they provide many different types of beams over a wide range of intensities, emittances and distances between bunches.
To overcome today's limitations of the injector chain, a significant upgrade program, the LHC Injectors Upgrade (LIU), has been launched at the end of 2010 [9].

2.2.1 Upgrade plan

To achieve the targets demanded by the HL-LHC, injectors must provide more intense beams within constant or, if possible, smaller transverse emittance, thus featuring increased brightness.
In the framework of the LIU project, various solutions are being implemented or under investigation in all the LHC injectors. The project, in fact, covers LINAC 4 and the upgrades of the PSB, PS and SPS that must be implemented by the end of the second Long Shutdown (LS2) to satisfy the beam requirements by the end of Run 3.
The LIU-PS project consists of two major upgrade programmes: the upgrade of the injection energy from 1.4 GeV to 2 GeV, with the necessary interventions in the injection area, and the upgrade of the RF systems to overcome space-charge limitations and longitudinal instabilities [37]. The goal is to increase the bunch intensity from $1.7{\cdot}10^{11}$ ppb to $2.6{\cdot}10^{11}$ ppb with emittances of 1.9 μm at ejection from the PS.
The maximum intensity $n_b N_b$ for bright bunches in the PS is mainly limited by longitudinal instabilities, due to coupled bunch oscillations, and transient beam loading. Coupled bunch instabilities are most likely excited by the impedance presented by the 10 MHz accelerating cavities to the circulating beam. To reach the HL-LHC beam characteristics, and reduce coupled bunch oscillations, a new wide-band feedback has

been installed, adopting a dedicated longitudinal kicker cavity [38].
Moreover the 1-turn feedback around the 10 MHz cavities has been upgraded [39] and, in addition, an upgrade of the wide-band feedback around the 10 MHz amplifiers has been investigated, to reduce the impedance presented by the cavities.
The latter will be the main topic of the first part of this thesis work; an in-depth analysis will describe the study and explain the work done to achieve this goal. In addition, the evaluation of the effective impedance of the total 10 MHz RF system in the PS ring is discussed. In fact, several machine development studies took place, and supported by numerical simulations, led to a full characterization of the beam-cavity interaction helping in the validation of the proposed upgrade.

Chapter 3

The 10 MHz PS high level RF system

In this chapter, a description of the 10 MHz accelerating cavity and its main control and tuning systems is provided.
The chapter is meant to give a comprehensive overview of the standard configuration of the amplifier driving the cavities, showing its present performance and highlighting its limitations. In addition, the amplifier-cavity PSPICE model, which will be largely used in the next chapters, is presented.

3.1 The 10 MHz RF cavity

The 10 MHz RF system consists of eleven accelerating cavities, operating in the frequency range between 2.8 and 10 MHz [40]. The system plays a crucial role in the beam dynamics of particles circulating in the PS ring, since it is responsible for the beam acceleration and allows beam manipulations, such as bunch merging, splitting and rotation.
The 10 MHz cavities (Fig. 3.1), ten operational plus one spare, are installed in straight sections 11, 36, 46, 51, 56, 66, 76, 81, 86, 91 and 96 of the PS ring. Moreover, a test cavity is located outside the PS ring, used for maintenance purpose and for testing the cavity-amplifier system. The cavities are programmable both in gap voltage (0.5 kV_p to 10 kV_p per gap) and frequency (2.8 MHz to 10 MHz) and they work in four groups

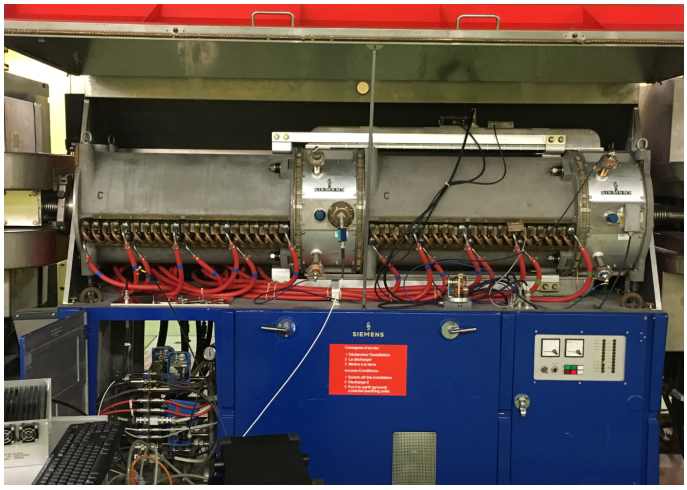

Figure 3.1: 10 MHz cavity. Two ferrite loaded cylinders with the accelerating gaps at their end can be identified. The blue base contains the power amplifier.

during the PS supercycle.

Each cavity consists of two lambda/4 shorted coaxial lines, partially filled with ferrite disks, with a capacitive ceramic gap at their input ends. In addition, a variable capacitor is connected in parallel to the gap, to let the cavity resonate at ∼2.6 MHz in absence of tuning current.

The two ceramic gaps allow the beam acceleration. As illustrated in Fig. 3.2, the two gaps are seen by the beam as in series, but they are fed in parallel by the RF power amplifier.

The beam passes through the cavity from left to right, i.e. first through the vacuum chamber of the left cavity half [41]. The chamber is surrounded by the ferrite rings, which are stacked together with copper cooling plates. After this section, the particles are accelerated by the alternating electric field in the first gap. The beam enters the second vacuum chamber where it is accelerated again by the second gap before leaving the cavity.

The RF voltage on the gaps is provided by a vacuum tube-based multi-stage amplifier, located at the base of the cavity, by means of two short coaxial bars.

The cavity losses are mainly due to the ferrite losses and the power amplifier output resistance. The equivalent resistance of a cavity gap measured at low voltage is 22 kΩ at 3 MHz and 10 kΩ at 10 MHz; the output resistance of the amplifier, which is

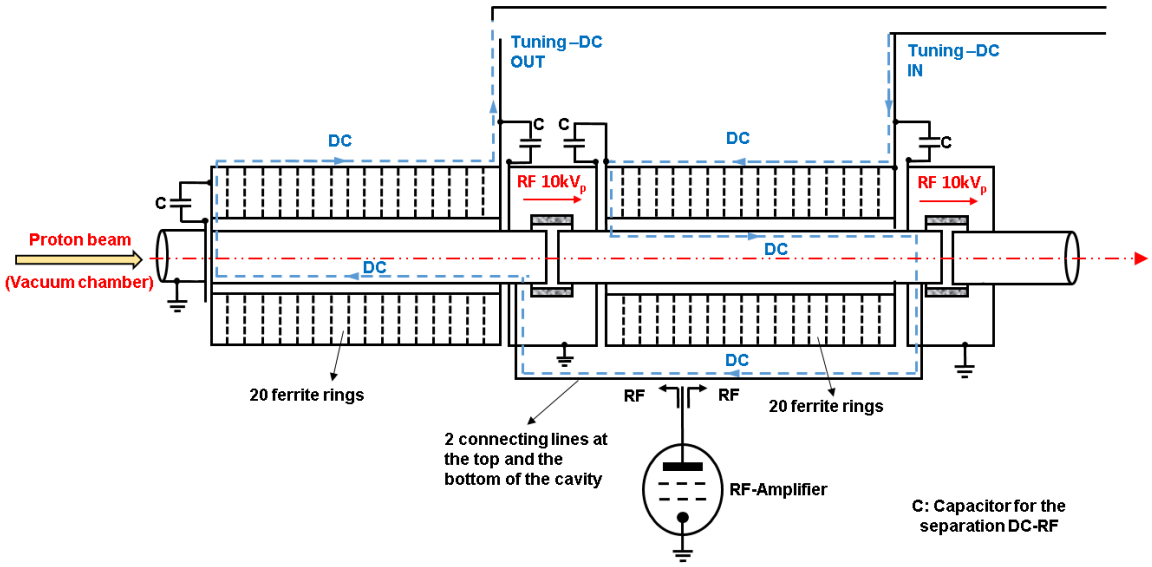

Figure 3.2: 10 MHz cavity skeleton.

equivalent to the anode resistance of the tube used in the final stage of the amplifier chain, is $\sim$6 kΩ.

When the cavities are not in use two high-voltage relays, one per cavity half, short-circuit the gaps reducing strongly their impedance and, as a consequence, the induced voltage by the beam.

3.1.1 Tuning system

Twenty 4L2-grade ferrite disks are used to fill each cavity half. The ferrite permeability is varied by means of a bias tuning current and, as a consequence, also the equivalent inductance of the cavity changes. This variable inductance, resonating with the capacitive gap of the cavity, allows tunability over the frequency range of 2.8-10 MHz.

The correct tuning of the cavity is provided by two systems: the *coarse tuning* and the *fine tuning*. The coarse tuning is the main tuning system, since it delivers up to 3 kA DC current to a group of cavities. The eleven cavities are divided into four main tuning groups, as shown in Tab. 3.1, to enable different beam RF manipulations at the same time.In fact, a dedicated module converts the requested cavity operational frequency to a signal driving the 150 kW power converter which delivers

up to 50 V/3 kA to each cavity group.

CT group #	1	2	3	4
Cavity straight sections	56-66-76-81	36-46-51	86-91-96	11-Test

Table 3.1: Coarse tuning groups.

In addition, each cavity is equipped with a fine tuning system. A variable current up to 300 A is added to the coarse tuning one, in order to set independently each cavity at the required resonant frequency. The fine tuning uses a closed loop control: it measures the phase difference between the grid and the anode RF voltage of the tube, used as a final stage of the amplifier chain, and it adds a bias current to keep the phase difference between the two signal at zero.
The interaction between the two tuning systems is critical, since the ferrites are very sensible to sudden current changes, which cause a permeability-distortion thus a temporary loss of Q, that tends to counteract the desired effect of the DC current. Therefore, the coarse tuning system is programmed to slowly increase the current after injection of particles. The fine tuning current is set at a constant value of 200 A when the gap voltage is $< 700\,\mathrm{V_p}$ and it switches to control mode once a stable RF amplitude ($> 700\,\mathrm{V_p}$) on the gap is achieved.
It is worth mentioning that the current circuit biasing the ferrites makes a figure-of-8 loop around the two cavity halves, which cancels out the total RF voltage induced in the DC path, and also provides a coupling between the two resonators.

3.1.2 Beam control system

The setting of cavity and machine parameters is crucial to provide the correct acceleration to the beam and to preserve the beam dynamic characteristics [42].
The first step consists in programming the B field slope characteristics of the bending magnets; from this, according to Eq. 1.14, the amplitude of the RF voltage is calculated for the corresponding increase in energy. At the same time, the RF frequency is determined from the B field. Then the beam-control system makes a fine adjustment, correcting the RF phase according to the beam position, in order to provide the correct acceleration with the right phase angle.
The RF voltage amplitude at the gap is controlled by the Amplitude Voltage Control

(AVC), which consists in a base-band feedback system. The AVC compares the RF voltage amplitude at the gap with the programmed voltage and compensates for possible differences, providing the input signal to the amplifier chain feeding the cavity. Figure 3.3 shows a diagram of the AVC feedback loop.

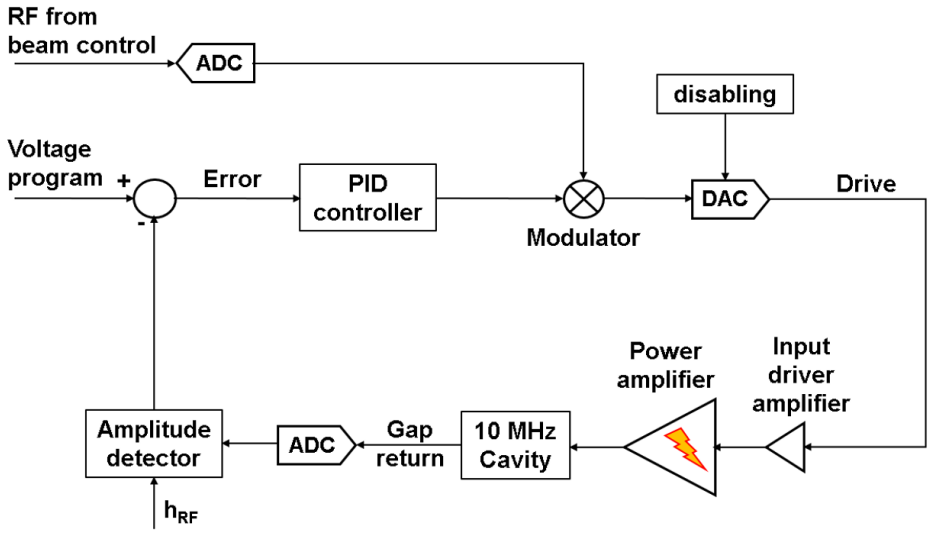

Figure 3.3: AVC feedback loop.

The main elements of the AVC are described in the following:

- the *Proportional-Integral-Derivative* (PID) controller is a control loop feedback mechanism. It takes an error signal as input, calculated as the difference between the detected gap voltage and the voltage program, and regulates its output according to the specific process requirements, providing the loop stability;
- the *RF modulator*, driven by the error-correction system and the RF program, modulates the amplitude of the RF signal provided by the beam control. Its output signal is the input to the amplifier chain that generates up to $10\,\mathrm{kV_p}$ RF voltage on the gaps;
- the *disabling system* ensures high power hardware safety; an *AVC surveillance* module inhibits the system when big discrepancies are found between the requested voltage and the cavity voltage (Fig. 3.4);

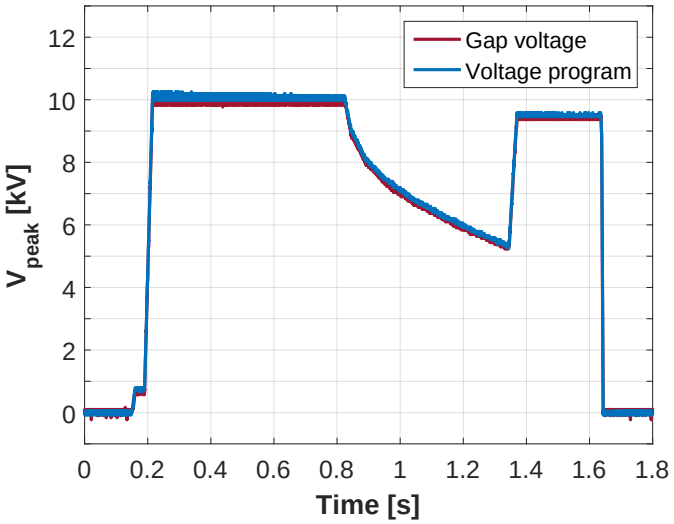

Figure 3.4: Voltage program and gap voltage signals of the AVC surveillance module.

- the amplitude detector extracts the amplitude of the RF signal measured on the cavity gap (gap return), comparing it with the amplitude of the programmed RF voltage.

3.2 The 10 MHz driving amplifier

The present configuration of the amplifier driving the 10 MHz cavities has been developed in 1989 [43]. It consists of three stages (Fig. 3.5):

- the input stage, the *Pre-driver*, whose control grid forms the capacitive summing point for the feedback signals and the RF input;
- the second stage, the *Driver*, has two tubes in parallel to increase the gain and the output current. This stage is loaded by a tunable resonator (grid circuit), where the local feedback signal is taken using a capacitive pick-up;
- the last stage, the *Final*, that delivers the needed power to the cavity to reach 10 kV_p per gap. The fast-feedback signal, intended to compensate for the beam loading, is taken from the anode of the Final tube using a capacitive pickup.

Mechanically, the amplifier is built as a removable module, placed in a box under the cavity. This box houses also the water and the air cooling systems and a power transformer for the filament heating of the Final tube. Power supplies, low-level electronics and the driving solid state amplifier, are located outside the PS ring to prevent radiation damages. All the parts of the amplifiers are mounted directly on the metal chassis, with the exception of the Pre-driver and Driver, placed in a removable box.

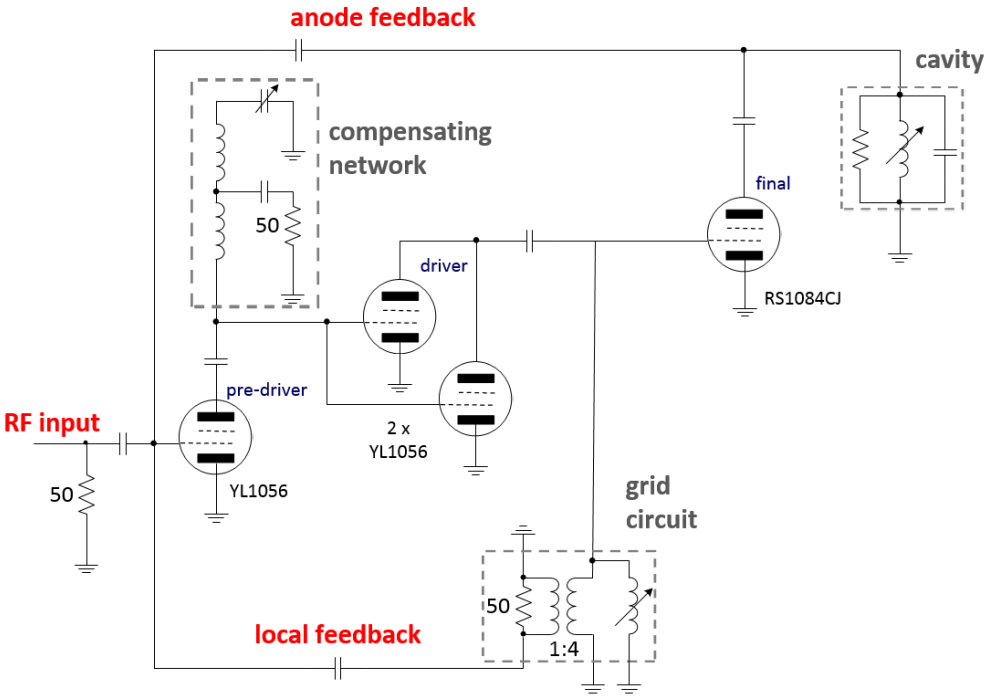

Figure 3.5: Simplified schematic of the amplifier chain, with its main elements. It contains 3 YL1056 tubes used for the Pre-driver and the Driver stages and the "RS1084CJ" tube of the Final stage. The Pre-driver is loaded by a circuit used for phase and amplitude compensation; the Driver is loaded by a tunable resonator made of a variable inductance, the Final tube input capacity and a transformed load. The Driver output signal is inverted and re-injected back into the summing point via a capacitor, as well as the Final anode signal. The cavity is represented as an equivalent parallel $R - L - C$ circuit.

3.2.1 Summing point

The *summing point* (Fig. 3.6) is the part in the amplifier chain where input and feedback signals are combined together. It forms a capacitive voltage divider with the feedback and the Pre-driver input capacities.
An external RF linear amplifier, provides the input signal to the amplifier chain; the present model (Herfurth) can deliver up to 150 W and it is terminated by a 50 Ω coaxial load in order to have a good matching over the whole frequency range. From this load the signal is sent into the summing point through a 100 pF capacitor.

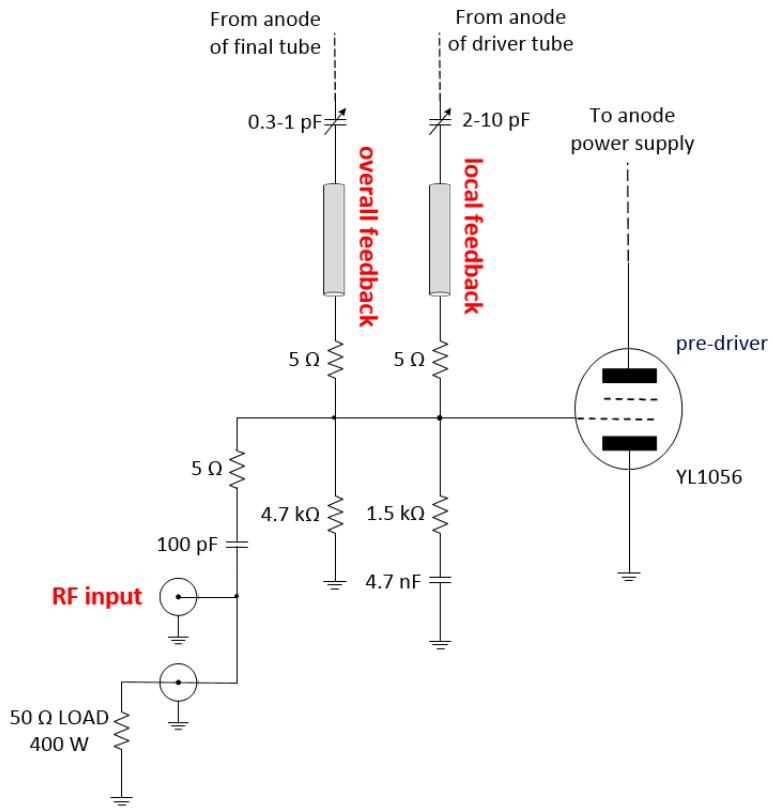

Figure 3.6: Schematic of the summing point.

Since the bandwidth of the "YL1056", tubes used in the Pre-driver and Driver stage, extends up to 1.2 GHz, 5 Ω resistors are placed in series with the input and the feedbacks capacitors in order to prevent oscillation at high frequencies. The 1.5 kΩ resistor and a 4.7 nF capacitor reduce the feedback at low frequencies, preventing oscillations

due to the parallel resonances of anode chokes and DC decoupling capacitors.

3.2.2 Pre-driver stage

The first stage of the amplifier chain is the Pre-driver. It is a wide band amplifier using one air cooled power tetrode "YL1056". It amplifies the signal coming from the summing point, and it can accept, with the present grid bias voltage, an RF signal of $\sim$90 V_{pp} maximum. The Pre-driver operates in class A and its forward transconductance is $\sim$80 mA/V. The tube filament voltage and current are respectively 3.8 V and 22 A.
In the standard operating conditions the anode voltage is 800 V, the anode current is 650 mA and the screen grid voltage is 300 V.
The transfer function of the stage, measured via a Network Analyser, is shown in Fig. 3.7.

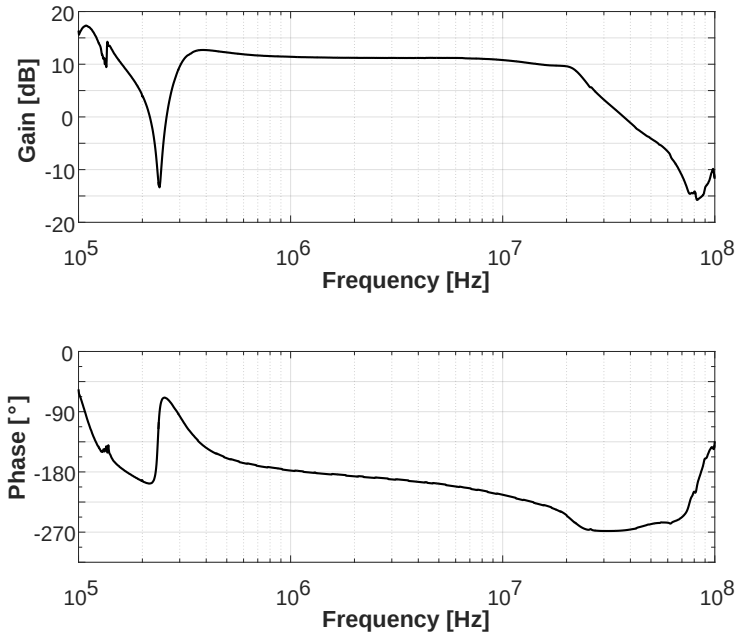

Figure 3.7: Gain and phase measurements of the Pre-driver stage.

The figure shows a gain essentially flat from 300 kHz to 20 MHz, of $\sim$11 dB. The series resonance at 270 kHz is due to the Pre-driver anode choke and the anode supply filter.

This stage is one of the main limits to the system stability, since it introduces a large phase shift between 3 MHz and 10 MHz, due to the Driver tubes input capacitance and the Pre-driver tube output capacitance. The amplifier is, in fact, equipped with a compensating network, which reduces this phase shift to about 30 ° (which is still relevant).

3.2.3 Driver stage

The Driver stage is made of two "YL1056" tubes in parallel and operates in class AB. The tubes work with 1200 V anode voltage and 1.2 A (600 mA per tube) anode current and 380 V screen voltage. Since the tubes are the same type of the first stage, the same filament supply settings are kept in the Driver stage.
In order to compensate for the large phase shift, which could be introduced by the Final grid input capacitance, the Driver is loaded by a ferrite variable inductance. The inductance resonates, in the frequency range of 2.8-10 MHz, with ∼390 pF, which is the parallel of the Final tube input capacitance and the Driver tubes output capacitance. This device also works as 1:2 voltage transformer, increasing the Driver load from 50 Ω to 200 Ω.

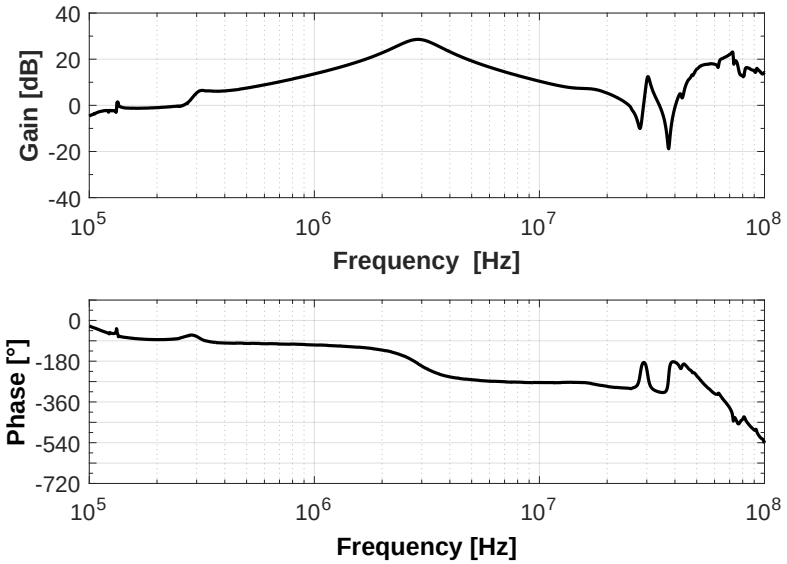

Figure 3.8: Gain and phase measurement of Driver at 3 MHz.

The Driver transfer function is largely affected by the grid circuit characteristics mainly set by the ferrite properties.

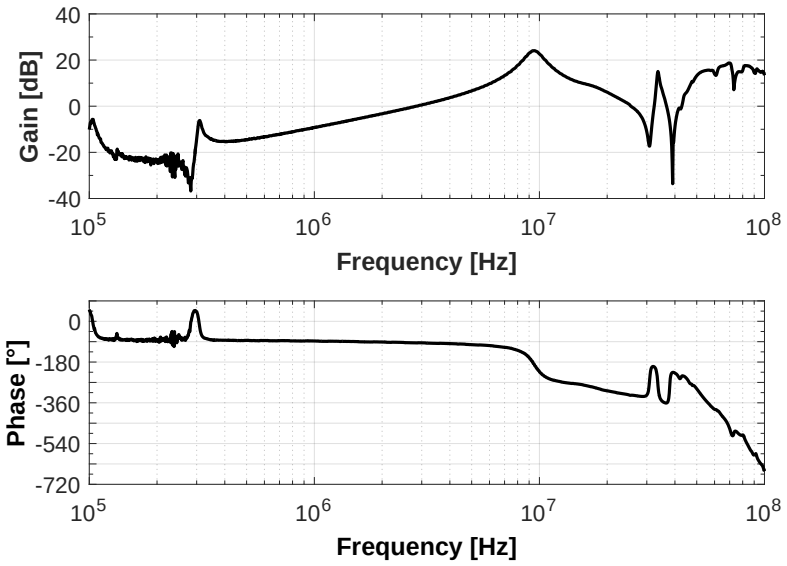

Figure 3.9: Gain and phase measurement of Driver at 10 MHz.

As shown in Figs. 3.8 and 3.9 the gain is about 27 dB at 3 MHz and 25 dB at 10 MHz. Several resonances can be identified in the figures: one resonance at 270 kHz is due to the anode choke, while the resonances above 10 MHz are due to the stray capacitance and the leakage inductance of the grid resonator.

3.2.4 Final grid circuit

As already mentioned, before the Final stage, the Driver is loaded by a *Final grid circuit* which performs the following functions:

- it serves as a ferrite-based variable inductance, whose value is changed via a DC current biasing the ferrite; this inductance resonates with the Final input grid capacitance, from 3 to 10 MHz, at the cavity resonating frequency;
- it transforms the Driver 50 Ω load into 200 Ω;
- it provides 180 ° phase shift for the local feedback signal;

Figure 3.10 shows a schematic of this device. The device is made of two $4L2$-grade ferrite rings and it has a complex construction [40]. The ferrite toroids are inserted in two copper sheets connected in figure-of-8, forming a two turn winding around the two ferrite rings: this represents the primary circuit of the transformer. One turn, symmetrically around the centre of winding, is picked up and connected to a 50 Ω load. The load is connected to the circuit via the inverting balun and transformed up to 200 Ω (transformation ratio 4:1). The transformer windings are shielded by a copper structure. The latter is wound by 50 figure-of-0 shaped turns of copper cable, connected to a DC bias, variable from 0 to 20 A current. This biasing current changes the permeability of the ferrite and thus the resonant frequency of the resonator.

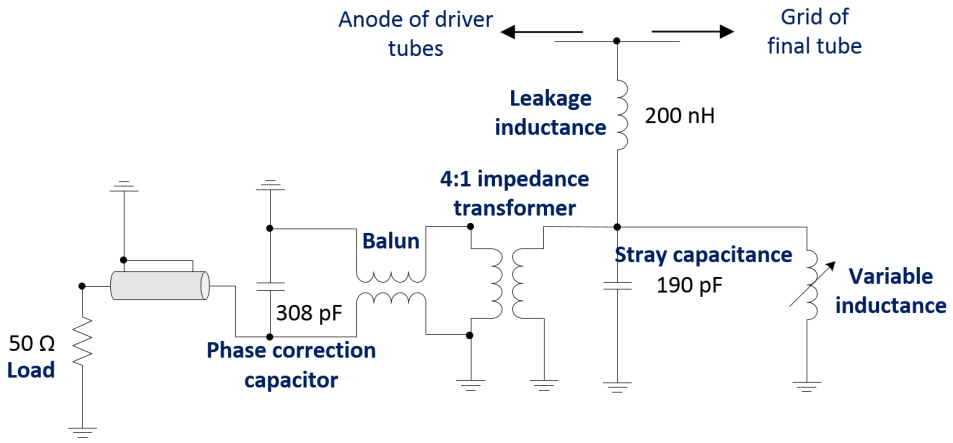

Figure 3.10: Schematic of Final grid resonator.

The tuning current is controlled by an EPROM based card which has two inputs: the fine and coarse tuning currents. This card converts the sum of the two signals into the corresponding bias current for the variable inductance.

The figure-of-8 shape of the RF winding causes the RF current B flux, flowing in opposite directions in each ferrite ring, to cancel out the RF voltage induced in the DC biasing windings.

The balun isolates the balanced 1-turn winding to connect the unbalanced 50 Ω load. Moreover, the correct phase shift for the local feedback signal is provided. Additionally, as shown in Fig. 3.10, a 308 pF capacitance is connected in parallel to the 50 Ω giving a small phase advance and a slightly lower Driver stage gain at 10 MHz, which improves the gain margin at this frequency.

In this Final grid circuit, the total stray inter-windings capacitance is about ∼190 pF and the leakage inductance of the internal connections amounts to ∼200 nH.

3.2.5 Local Feedback

The output voltage of the Driver is fed back into the summing point through a cable connected to a variable capacitor (∼2-10 pF), as sketched in Fig. 3.6.
The local feedback lowers the Q of the first two stages chain (which, for simplicity of description, we will call "local amplifier"), providing a better stability of the whole amplifier chain, as explained in the following.
A low Q is an important requirement of the grid resonator, since this ensures a low group delay. The group delay τ_G of a resonator is defined as the rate of change of the total phase shift $\Delta\varphi$ in an interval $\Delta\omega$:

$$\tau_G = \frac{\Delta\varphi}{\Delta\omega} \tag{3.1}$$

As one can observe in Fig. 3.11, showing the response of a generic parallel $R-L-C$ circuit with $Q > 1$, the phase of a resonator (red curve) is approximately linear over the bandwidth BW, which means that its group delay is constant.

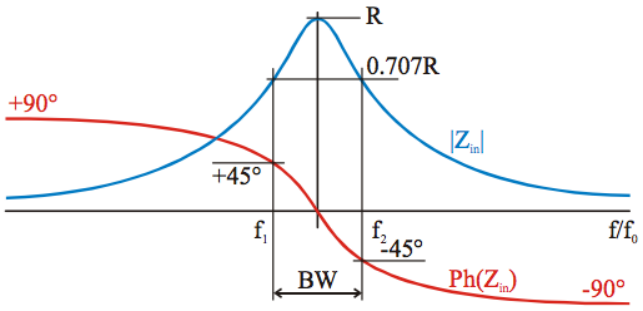

Figure 3.11: Impedance versus frequency characteristics of the parallel $R-L-C$ resonator.

If the resonator has a low Q, the phase variation results slower in its characteristic bandwidth, therefore the group delay is reduced.
The cavity has the highest Q value in the system. The phase is already constant $(+/-90\,^\circ)$ at the frequencies where we analyze the stability of the amplifier chain,

and its group delay is negligible. The total group delay of the full system is mainly due to the contribution of the local resonator and the group delay introduced by the cables length and by the electronics.
Figures 3.12, 3.13, 3.14 and 3.15 show the transfer function of the local amplifier at 3 MHz and 10 MHz, when the feedback loop is opened and closed.

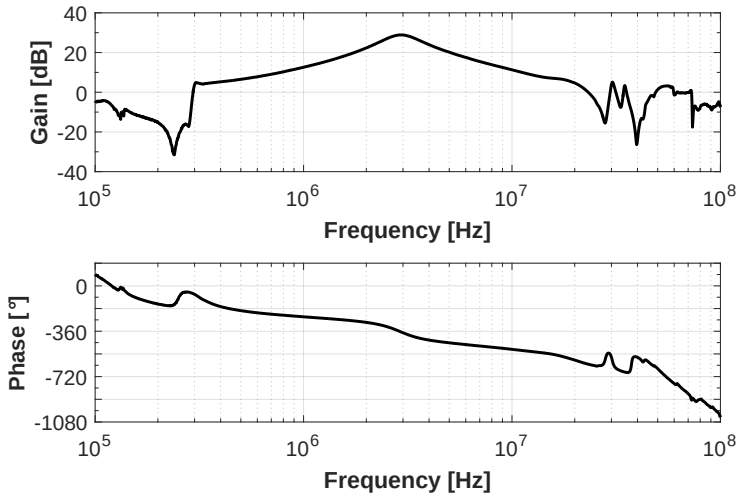

Figure 3.12: Gain and phase measurement of local open loop at 3 MHz.

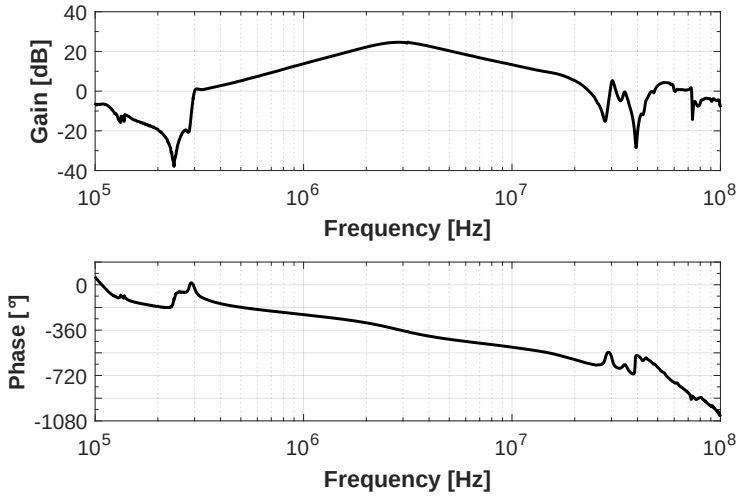

Figure 3.13: Gain and phase measurement of local closed loop at 3 MHz.

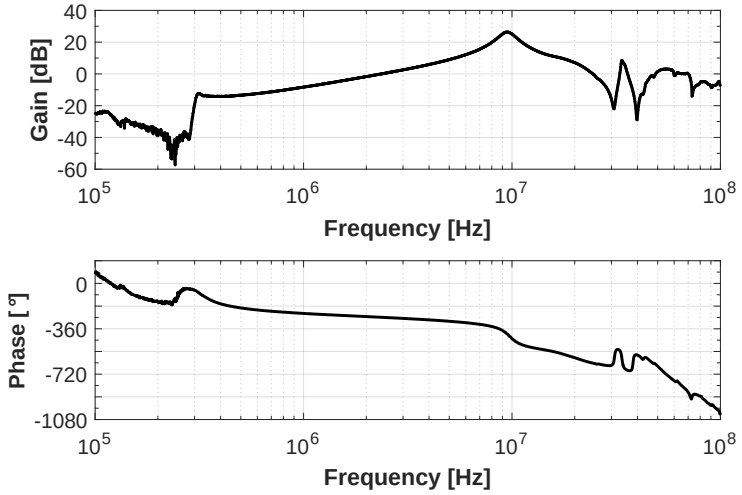

Figure 3.14: Gain and phase measurement of local open loop at 10 MHz.

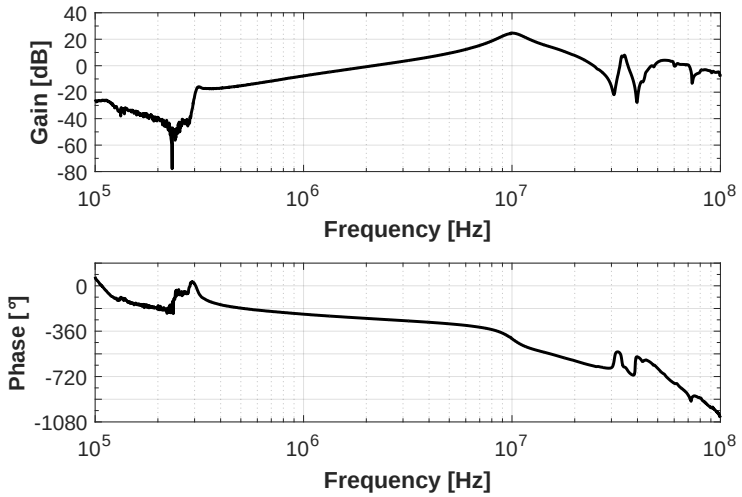

Figure 3.15: Gain and phase measurement of local closed loop at 10 MHz.

Tables 3.2 and 3.3 summarize the effect of the feedback involving Driver and Predriver stages, in terms of reduction of Q, gain and increase of bandwidth at 3 MHz and 10 MHz.

	Gain [dB]	**BW [MHz]**	**Q**
loop open	29	1.24	2.33
loop closed	24.6	2.52	1.133

Table 3.2: Gain, BW and Q values of the local amplifier transfer function, when the feedback loop is open and closed at 3 MHz.

	Gain [dB]	**BW [MHz]**	**Q**
loop open	26.37	1.8	5.37
loop closed	24.5	2.61	3.7

Table 3.3: Gain, BW and Q values of the local amplifier transfer function, when the feedback loop is open and closed at 10 MHz.

3.2.6 Final stage

The Final stage provides the RF current needed to reach the nominal voltage on both gaps. This stage is based on water cooled tetrode "RS1084CJ" and it operates in class AB. The DC anode current is 1.5 A, the anode voltage is 15 kV and the control grid voltage is 1500 V. The filament is supplied by a transformer that delivers 12.5 V and 200 A. The water cooling system keeps the maximum anode temperature below 50 °C. Figures 3.16 and 3.17 show the characteristic curves of the Final stage at 3 MHz and 10 MHz. The stage gain, measured with a capacitive probe with 80 dB attenuation, is about 44 dB at 3 MHz and 42 dB at 10 MHz; the lack of gain at 10 MHz is due to the higher losses of the ferrites used in the cavity .
The stage is loaded by the cavity. The current is provided in parallel to the two gaps, by the means of two rectangular coaxial lines. The latter are short enough, so that the voltage developed on the anode is almost the same voltage on both gaps.
The cavity coupling line resonates with the anode capacity of the Final tube at ∼35 MHz. Moreover, the lines coupling the two sections of the two cavity halves resonate at the same frequency. A filter connected to the anode partially dumps these resonances.

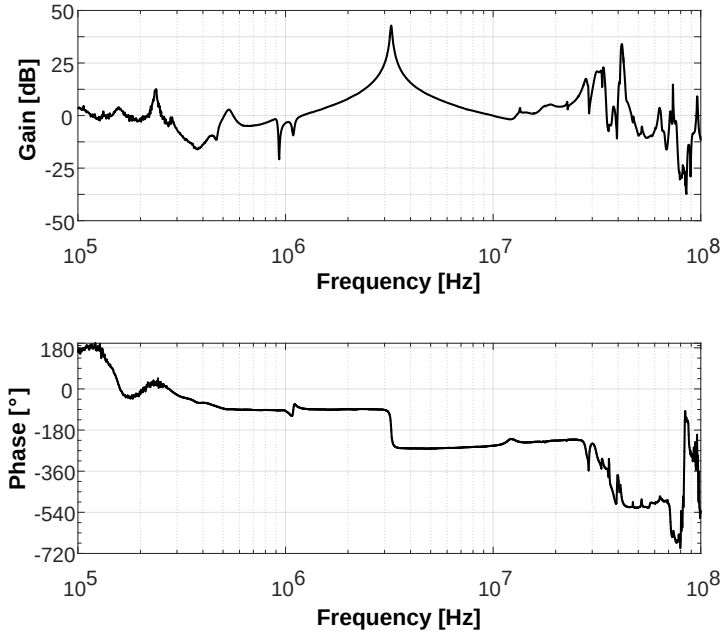

Figure 3.16: Gain and phase of the Final stage at 3 MHz.

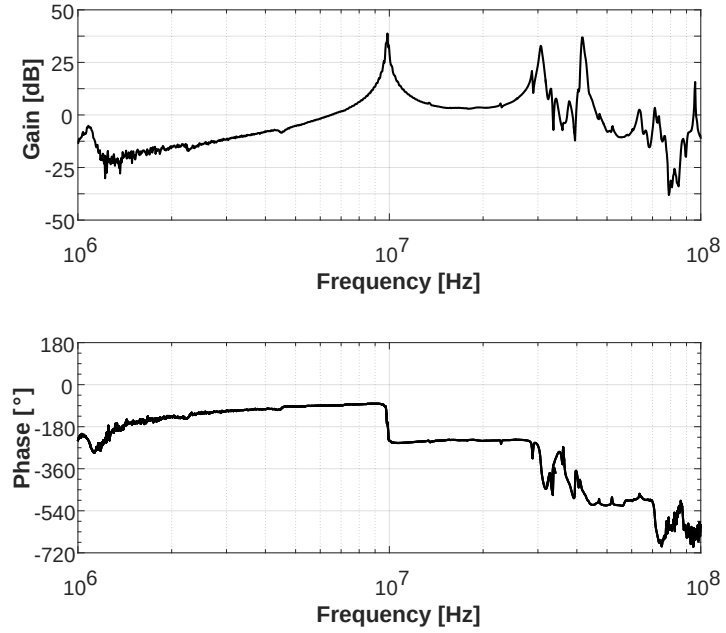

Figure 3.17: Gain and phase of the Final stage at 10 MHz.

3.2.7 Overall feedback

The amplifier chain is enclosed in a feedback loop, which reduces the equivalent impedance seen by the beam, when it crosses the gaps. Part of the anode voltage is fed back into the summing point via a capacitive coupling to the anode provided by a disk. The diameter and the position of the disk determines the attenuation of the feedback loop.
Figures 3.18 and 3.19 show the open and closed loop gain of the system at 3 MHz and 10 MHz.

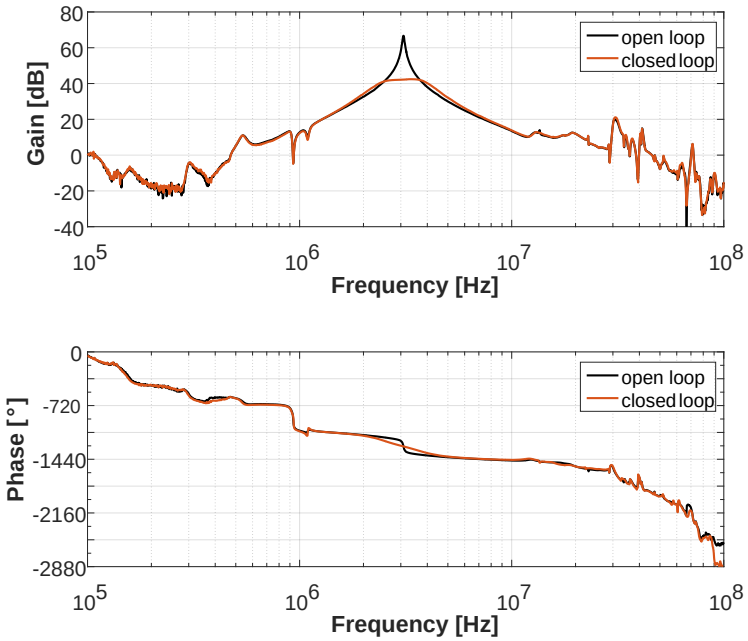

Figure 3.18: Gain and phase of the whole amplifier at 3 MHz.

The loop gain is ∼25 dB. The impedance of one cavity gap seen by the beam is typically 350-400 Ω. In the framework of the LIU project [9], an upgrade of the cavity-feedback system has been investigated and developed, aiming at lowering the cavity impedance as much as possible.
Presently the 11 cavities in the PS ring have an impedance reduction factor ≤20 (∼24/26 dB of loop gain), which is about the maximum that can be obtained with this configuration. An important requirement of a well-performing feedback system

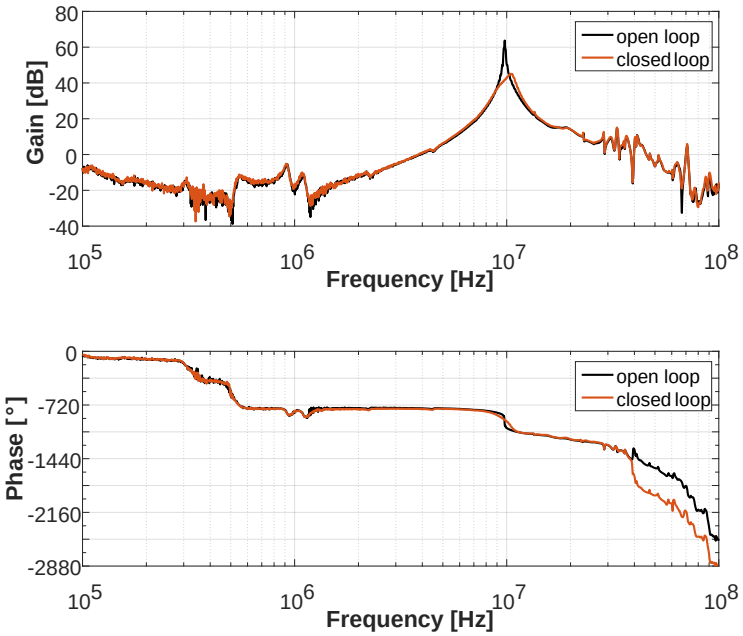

Figure 3.19: Gain and phase of the whole amplifier at 10 MHz.

is that the group delay must be reduced as much as possible, since the large phase shift in the feedback chain may drive the system into instability. The wide operating frequency range, the time delays and phase shifts introduced by the cables, filters and amplifiers causes the phase margins to be pretty small.

A negative phase shift from the ideal phase is observed in the transfer function of the whole chain and it is mainly due to the first stage and cables delay. This phase shift is compensated by tuning the local resonator at a higher resonant frequency than the cavity, therefore adding a positive phase at the cavity resonant frequency.

Increasing the loop gain, the bandwidth increases as well, but the response is no more symmetrical, because of the large phase shift, as shown in Fig. 3.19. This asymmetry may lead to beam instabilities; in fact, a further increase of the loop gain can turn the amplifier into an oscillator. The aim of the proposed upgrade therefore consists of improving the margins of the system, allowing an additional increase of the loop gain.

3.3 PSPICE simulations

The studies leading to the system upgrade have been carried out via direct measurements on the amplifier system and via simulations of the latter's performance in PSPICE [44]. An exhaustive model, was developed. It turned out to be of a great help in the characterization of every single element of the circuit and the understanding of their contribution to the whole system behaviour and stability.
Dedicated libraries have been developed to reproduce the tubes behaviour, including their non-linearity. The tube anode current as a function of the anode and the control grid voltage were extracted from the datasheet (Fig. 3.20) or directly measured [45]. The collected data has been then elaborated in Matlab [47], to extract the information needed to generate the dedicated PSPICE code. This procedure is explained in the following.
The anode current is by definition a function of the anode voltage, of the screen and control grid voltages [46], according to:

$$I_A = k\left(V_g + \frac{V_s}{\mu_2} + \frac{V_A}{\mu_A}\right)^n, \tag{3.2}$$

where V_g, V_s and V_A are, respectively, the potentials of the control grid, the screen grid, and the anode with respect to the cathode and k, μ_2, μ_A, n are constants. Typically $\mu_2 \sim 5-10$, $\mu_A \sim 100-200$ and n is in the range 1.5 to 2.5. Since, in our case, the screen is kept at constant DC voltage, the dependence of the anode current on the screen voltage can be neglected. The anode current can therefore be written as a function of the grid and anode voltage.
In order to create a realistic PSPICE model of the four tubes in the amplifier stages, the anode current for several anode and grid voltages was measured. In the first step the anode current is expressed as a polynomial function of the grid voltage at constant anode voltage $I_A = f(V_g)|_{V_A=const}$. The measured data, together with datasheet ones,

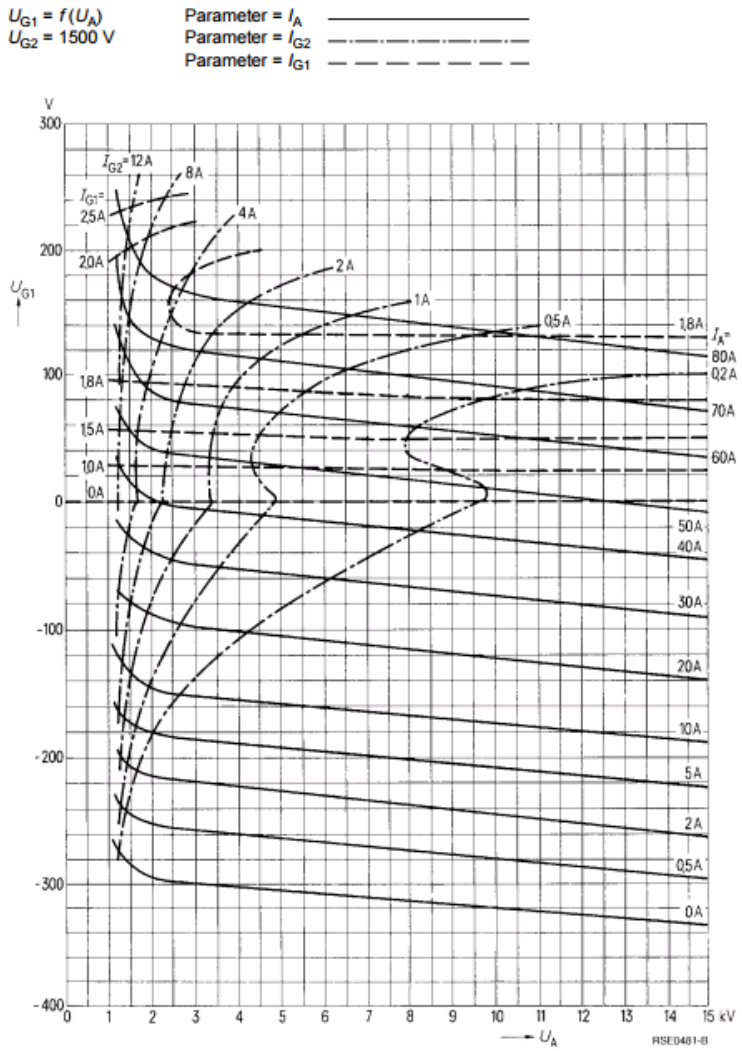

Figure 3.20: Datasheet curves of RS1084CJ tetrode with screen grid at constant voltage V_s=1500 V.

were then used to calculate the $a_{n,k}$ coefficients of the system of equation 3.3:

$$\begin{cases} I_1 = a_{n,1} \cdot V_g^n + a_{n-1,1} \cdot V_g^{n-1} + \cdots + a_{1,1} \cdot V_g + a_{0,1}|_{V_{A1}} \\ I_2 = a_{n,2} \cdot V_g^n + a_{n-1,2} \cdot V_g^{n-1} + \cdots + a_{1,2} \cdot V_g + a_{0,2}|_{V_{A2}} \\ \vdots \\ I_k = a_{n,k} \cdot V_g^n + a_{n-1,k} \cdot V_g^{n-1} + \cdots + a_{1,k} \cdot V_g + a_{0,k}|_{V_{Ak}} \end{cases} \tag{3.3}$$

where V_g is the control grid voltage and $(I_1, I_2, \cdots, I_k)$ are the values of the anode cur-

rents as a function of the grid voltage at constant anode voltage $(V_{A1}, V_{A2}, \cdots, V_{Ak})$. In a second step the anode current is expressed as a function of both the grid and anode voltages:

$$I_A = A_n(V_A) \cdot V_g^n + A_{n-1}(V_A) \cdot V_g^{n-1} + \cdots + A_1(V_A) \cdot V_g + A_0(V_A) \tag{3.4}$$

where the coefficient $A_{n,\cdots,0}$ are expressed by the system of equation in the following:

$$\begin{cases} A_n(V_A) = f\left(a_{n,k}, a_{n,k-1}, \cdots, a_{n,0}\right) \\ \qquad\qquad \vdots \\ A_1(V_A) = f\left(a_{1,k}, a_{1,k-1}, \cdots, a_{1,0}\right) \\ A_0(V_A) = f\left(a_{0,k}, a_{0,k-1}, \cdots, a_{0,0}\right) \end{cases} \tag{3.5}$$

For a generic V_A value, PSPICE calculates the coefficients $(A_n, \cdots, A_0)$ using a linear interpolation between the adjacent values of the vector $(a_{i,k}, a_{i,k-1}, \cdots, a_{i,0})$, where i varies from 0 to n. The order of the polynomial of Eq. 3.4 is chosen in order to better fit the real data.

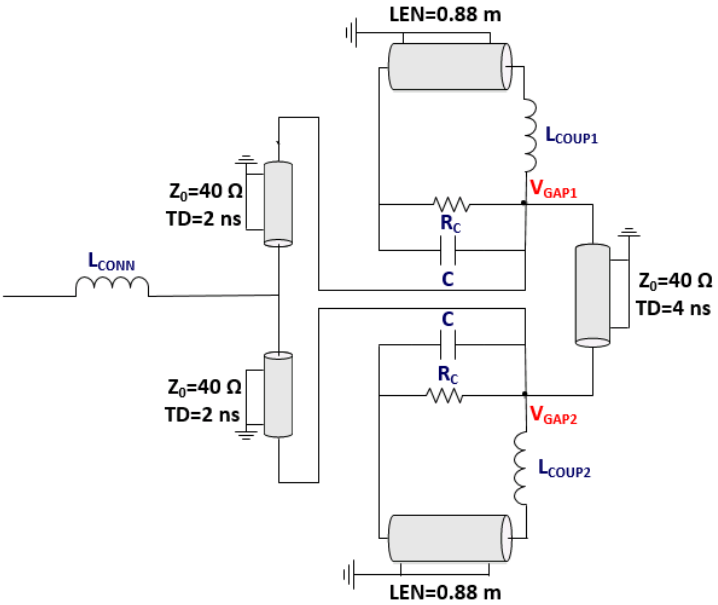

Figure 3.21: Electrical equivalent model of the 10 MHz cavity.

The cavity is modeled in PSPICE as in Fig. 3.21. L_{CONN} represents the equivalent 260 nH inductance of the line which couples the amplifier to the cavity, and which

resonates at ∼35 MHz with the Final tube anode capacity. R_c represents the ferrite losses of one cavity half: it varies with the frequency, proportionally to the μ'' of the ferrite; C is the equivalent 210 pF capacity of one gap. A 4 ns coaxial line electrically couples the two gaps. L_{COUP1} and L_{COUP2} are two coupled 0.2 μH inductances, modelling the magnetic coupling between the two gaps, made in reality by the 8-shaped path of the ferrite bias. Two 2 ns lines are used to connect the RF amplifier to the two gaps; the two shorted coaxial lines, 0.88 m long, model the inductive contribution of the two cavity halves. In the model, the resonant frequency of the cavity is changed by varying the inductance per unit length of the two coaxial lines. Particular effort has been spent to get a good matching between the measurements and PSPICE simulations. The model, based on the real circuit components, was not able to fully reproduce the behaviour of the system in a wide frequency range: parasitic components (stray capacitance and leakage inductance) of the amplifier electronics or inter-stage connections has been added in the PSPICE model, taking into account their variation with frequency.

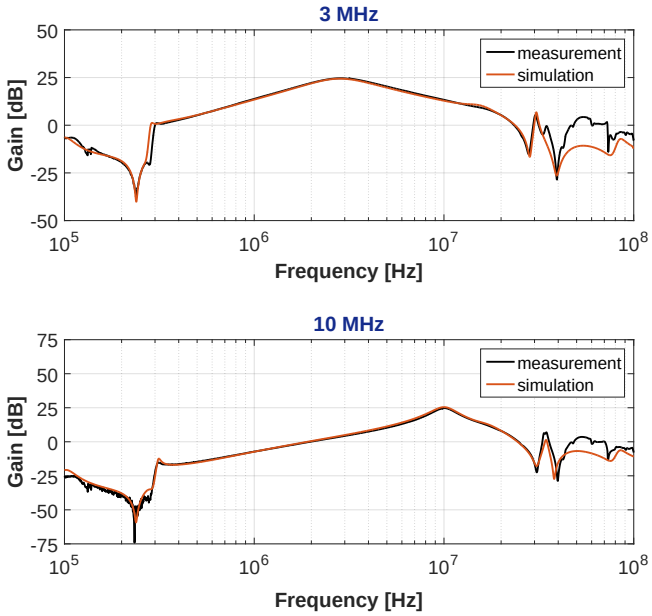

Figure 3.22: Comparison between measurements and simulations of the local loop transfer function at 3 MHz and 10 MHz.

A comparison between simulations and measurements of the gain of the local amplifier

is shown in Fig. 3.22.

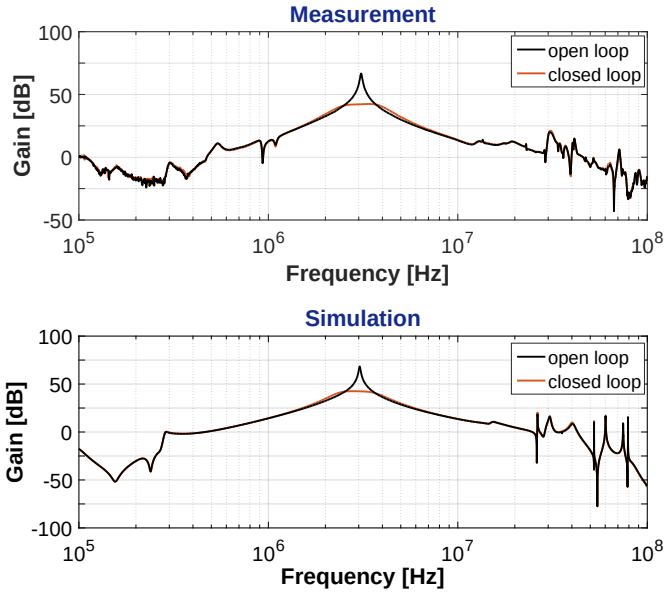

Figure 3.23: Comparison between measurements and simulations of the transfer function of the system at 3 MHz.

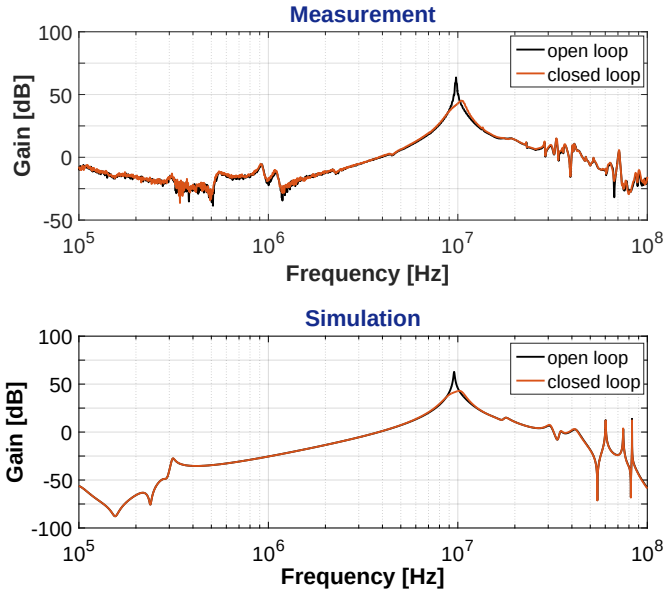

Figure 3.24: Comparison between measurements and simulations of the transfer function of the system at 10 MHz.

The simulations reproduce the behaviour of the local amplifier quite well, including the gain difference between 3 and 10 MHz due to the transformer losses. The simulations and measurements of the transfer function of the whole system at 3 MHz and 10 MHz, shown in Figs. 3.23 and 3.24 are also in a good agreement.

Chapter 4

The PS 10 MHz RF system upgrade

The upgrade of the 10 MHz system, described in the following, aims at increasing the loop gain of the RF amplifiers driving the PS 10 MHz cavities, still providing a stable operation and avoiding a complete re-design of the system. Sticking to the present electron tube technology is in fact preferred, because of its radiation hardness [48]. With the present architecture the main factors that limit the increase of the loop gain are:

- the maximum available power of the amplifier driving the system (150 W) and its harmonic content at high power;
- the maximum allowed voltage on the Pre-driver grid;
- the large phase shift introduced by the first stage and the feedback loops at 10 MHz.

In this chapter the solutions adopted to overcome the aforementioned limits are presented. The main hardware modifications are described into detail, posing a high attention on the improvements of the RF system stability, beside the expected cavity impedance reduction.

4.1 Change of RF tubes working point

The first step of the upgrade was focused on exploring the possibility to increase the open loop gain of the amplifier chain.
Higher gain has been achieved by changing the working point of the RF tubes, i.e. by changing their biasing conditions, while keeping the parameters of the tubes below the maximum ratings. The anode bias current and voltage values of the three stages with the original configuration and the modified one are reported in Tab. 4.1.

Stage	V_A **[V]**	I_A **[A]**
Pre-driver	800 → 600	0.7 → 0.9
Driver	1200 → 800	1.2 → 1.8
Final	15000	1.5 → 3

Table 4.1: Change of bias conditions of the tubes used in the three stages of the amplifier chain.

In the first two stages, the anode voltage and current have been changed keeping the anode dissipation constant. The anode voltage has been set sufficiently high to leave enough voltage swing to fully drive the following stage. The anode voltage of the Final stage could not be reduced otherwise the amplifier could not reach the required 10 kV_p on the anode. However, the anode current has been increased to 3 A, rising the anode dissipation to 45 kW. The consequent higher dissipation has required the redesign of the water cooling system of the tube. In fact, the new working point was chosen taking into account the maximum capacity of the cooling system (50 l/min water flow).
It is worth recalling that the gain of a tube amplifier is expressed by:

$$\mu = g_m \cdot Z_L \tag{4.1}$$

where Z_L is the anode load and $g_m = \Delta I_A / \Delta V_g$ is the tube transconductance (i.e. the incremental change in anode current divided by the incremental change in grid voltage, under the condition that all the other voltages remain unchanged [49]).
By changing the working point of the RF tubes the transconductance is increased, as well as the gain. Figure 4.1 shows the effect of changing the operating condition of the Final tube on its transconductance, defined as the slope of the tangent line to

the anode current curve as a function of the grid voltage, at the working point.

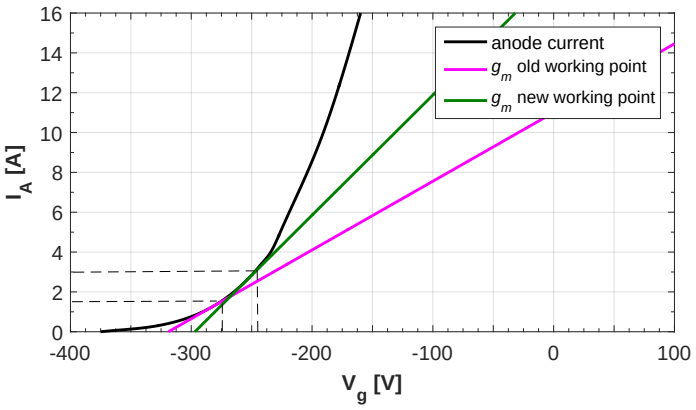

Figure 4.1: Anode current as function of the grid voltage of the Final tube, with V_A=15 kV. The two lines represent the tangent to the curve with the old operating condition (1.5 A, pink line) and with the new one (3 A, green line).

The resulting increase of gain has been evaluated by measuring the transfer function of the three stages, shown in Figs. 4.2, 4.3 and 4.4.

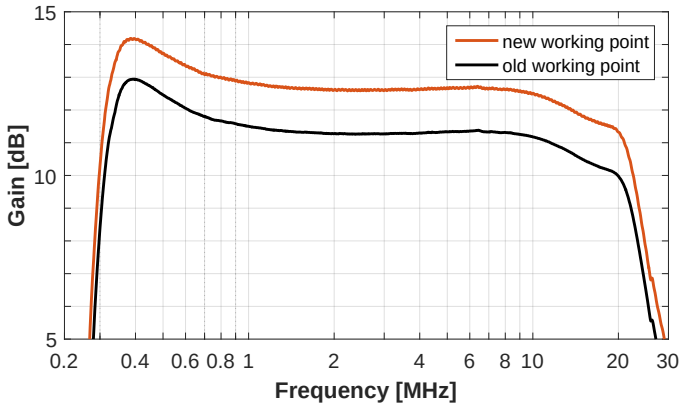

Figure 4.2: Gain of the Pre-driver stage with the old (back trace) and the new (orange trace) bias conditions.

About 2 dB of gain increase, obtained in each stage, could be observed, resulting in 6 dB additional overall gain.
Since the anode resistance is defined as the incremental change of the anode voltage

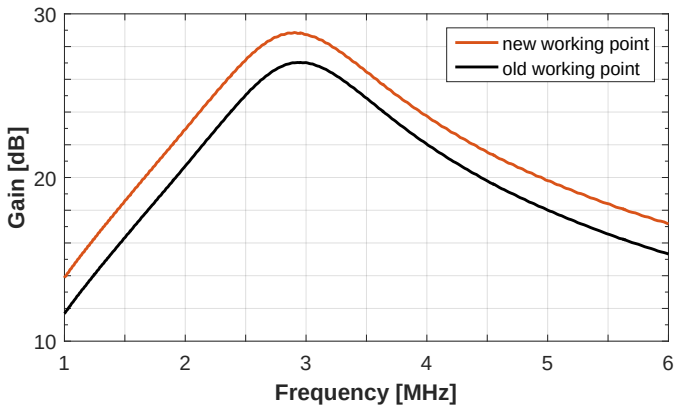

Figure 4.3: Gain of the Driver stage with the old (black trace) and the new (orange trace) bias conditions.

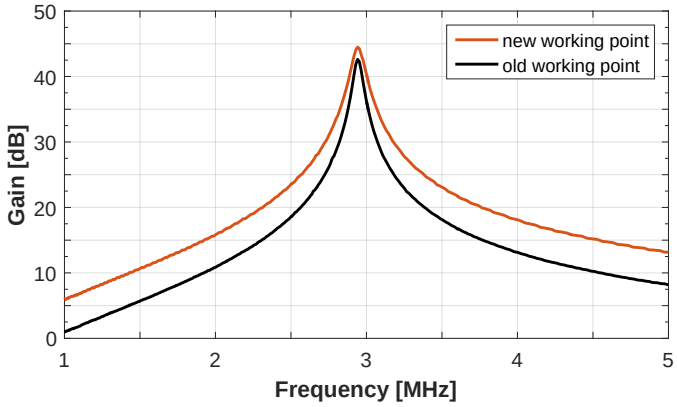

Figure 4.4: Gain of the Final stage with the old (black trace) and the new (orange trace) bias conditions. The larger bandwidth of the orange trace is the consequence of the anode resistance reduction.

divided by the respective incremental change of anode current:

$$R_F = \frac{\Delta V_A}{\Delta I_A} \tag{4.2}$$

another advantage is therefore obtained by changing the working point of the Final stage, the reduction of the anode resistance. Figure 4.5 is a plot of the anode current

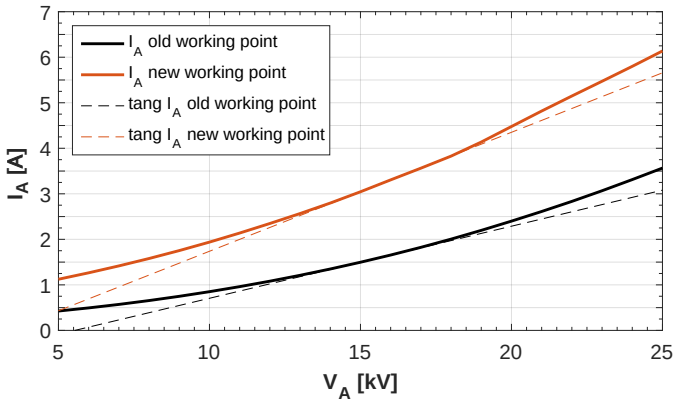

Figure 4.5: Anode current of the RS1084CJ tube as function of the anode voltage, with old operating conditions (V_g=-278 V, I_A=1.5 A, black trace) and the new ones (V_g=-245 V, I_A=3 A, orange trace).

of the Final tube with the old operating conditions (black trace) and the new one (orange trace). The slope of the tangent to the curve at the working point is $1/R_F$. A reduction of the anode resistance from 6.3 kΩ to 3.8 kΩ with the new working point has been achieved.

A loop gain of ∼28 dB have been achieved with the new operating conditions. However, the big phase shift between 3 and 10 MHz caused an asymmetry of the closed loop transfer function at 10 MHz, as shown in Fig. 4.6. This drove the amplifier to instability at 10 kV_p/gap.

In fact, the phase at the cavity resonance, when tuned at 10 MHz, was not exactly 180 ° and the large group delay led the phase dropping fast above 10 MHz (Fig. 4.7). Part of the increased forward gain (∼3 dB) had to be therefore used to improve the stability margins of the amplifier chain, by reducing as much as possible the phase shift in the operating frequency range.

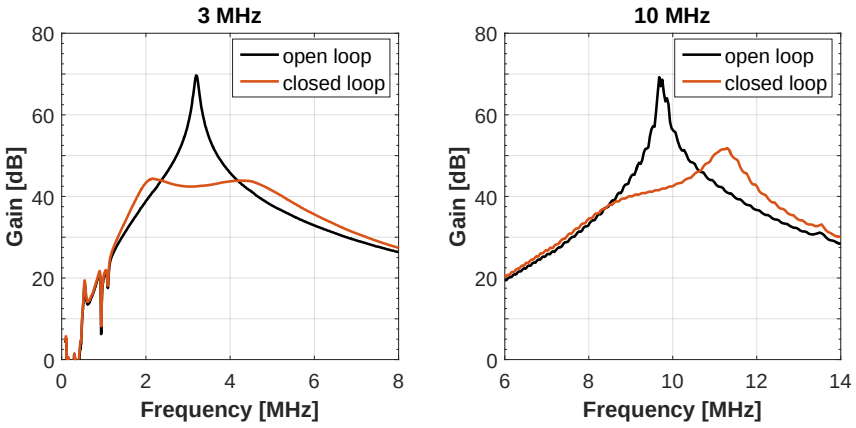

Figure 4.6: Transfer function gain of the whole amplifier when the feedback is open (black trace) and when it is closed (orange trace), at 3 MHz and at 10 MHz.

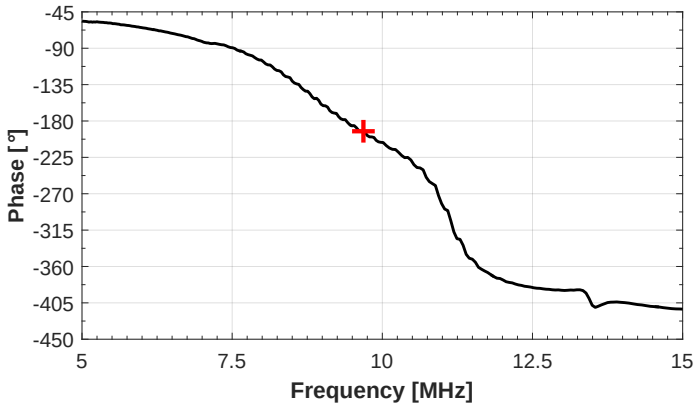

Figure 4.7: Closed loop transfer function phase of the whole amplifier at 10 MHz. The red marker is placed at the resonant frequency of the cavity.

4.2 Grid circuit upgrade

As already mentioned in Sec. 3.2.5, the Final grid resonator plays an important role in the stability of the amplifier chain. Measurements have shown that the transformed load at the primary of the transformer is not the same at 3 MHz and 10 MHz, leading to a lack of Driver gain at 10 MHz. Additionally, it is characterized by an high stray inter-windings capacitance and leakage inductance, which cause unwanted resonances at high frequencies. The response of the whole amplifier, at these frequencies, shows already a resonance (35 MHz) with quite high Q and gain, due to the line connecting

the amplifier to the cavity and which may lead the system to instability.
In order to analyze the circuit in details, the board housing the grid circuit has been dismounted from the amplifier and the device has been measured using the dedicated set-up illustrated in Fig. 4.8.

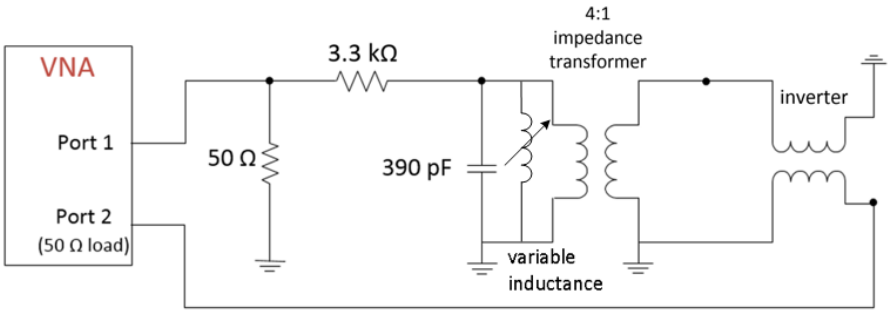

Figure 4.8: Testing set-up of the grid circuit. The output of the resonator is measured by injecting an RF current via a 3.3 kΩ resistor.

The 390 pF capacitor represents the input capacitance of the Final tube plus the output capacitance of the Driver tubes. The measurement of this device revealed several high-Q resonances between 30 and 40 MHz, which prevent the increase of the local feedback (Fig 4.9). Moreover, decreasing the local closed loop gain would require a further increase of the RF input power to reach 10 kV_p at the gap.

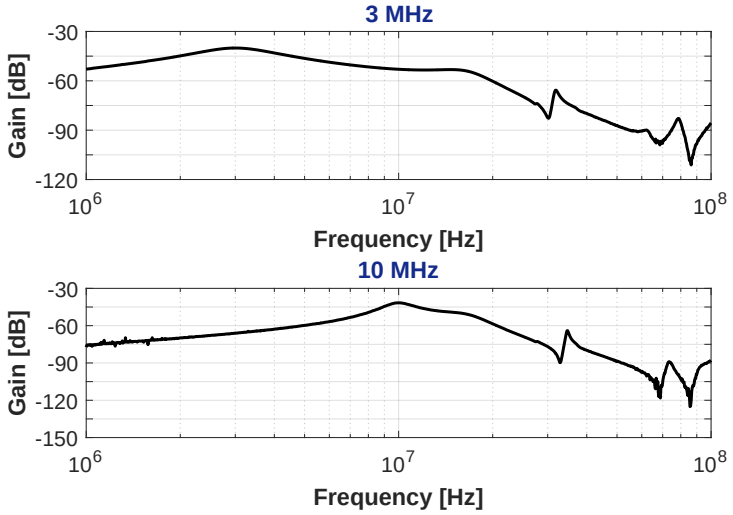

Figure 4.9: Response of the resonator tuned at 3 MHz and 10 MHz.

In addition, as shown in Fig. 4.10, another ∼15 ° of phase shift between 3 and 10 MHz was found to be introduced by the local inverter, due to the cable length. Due to the higher group delay introduced in the loop, it further decreases the stability margins.

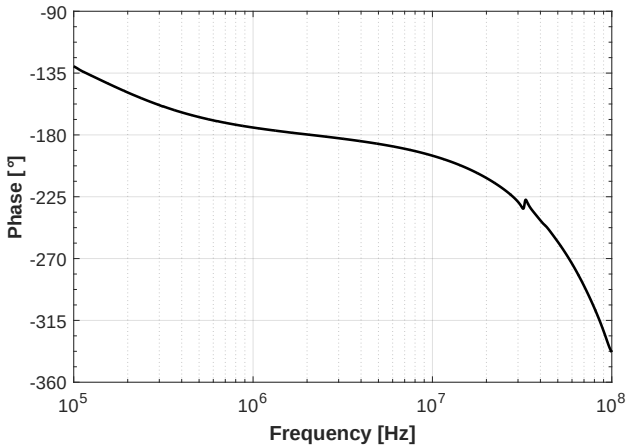

Figure 4.10: Phase shift introduced by the inverting balun of the grid circuit.

In summary, the analysis of the old grid circuit led to the final decision of replacing it with three independent devices [51], one for each function it is meant to accomplish, as shown in Fig. 4.11.

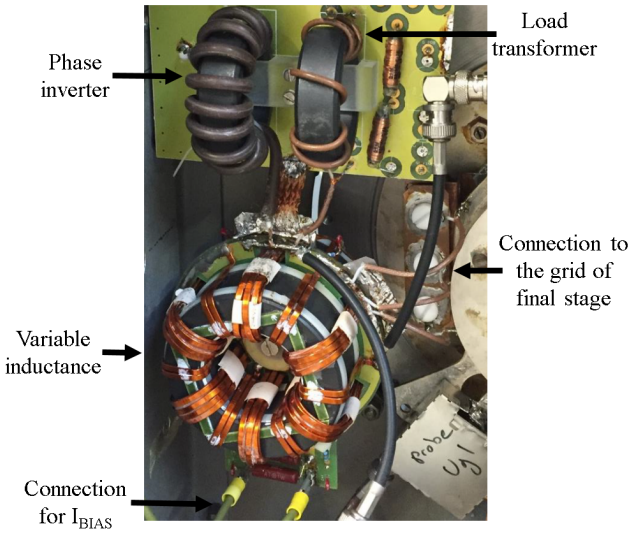

Figure 4.11: Prototype of the new variable inductance, transformer and inverter mounted in the amplifier.

The new transmission line transformer (50 to 200 Ω) is made of a coaxial cable wound on a ferrite core [50]. The new design features lower losses at 10 MHz: 178 Ω have been measured at the transformer output.

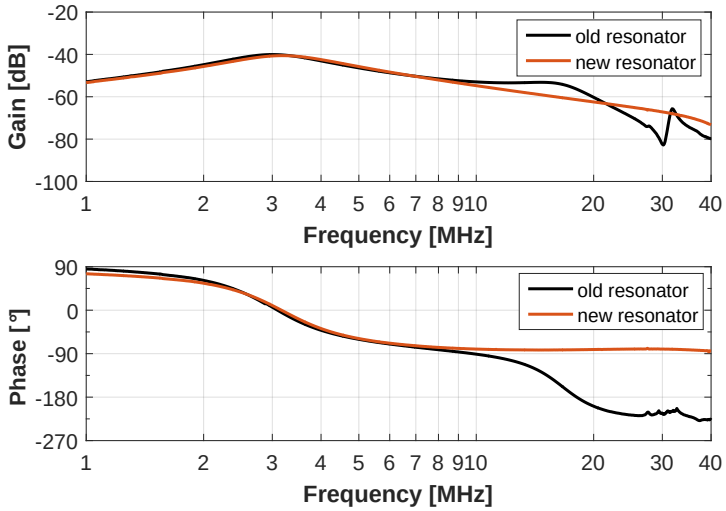

Figure 4.12: Comparison between the response of the old resonator and the new one.

Figure 4.12 shows both the response of the old and new equivalent resonator, measured using the aforementioned set-up (Fig. 4.8). Unwanted resonances have also been removed together with their contribution to the total phase shift. Moreover the reduction of the stray capacitance reduced also the current needed for the tuning.
Since the ferrite losses may increase when exposed to an high RF field, affecting the final performance of the grid circuit, the latter has been tested by driving it with an high amplitude RF input, using the set-up shown in Fig. 4.13. This test allows to verify the linearity of the circuit, and eventually evaluate the ferrite losses. The output across the resonator has been measured, while increasing the RF input power by steps of 6 dB and using an amplifier characterized by a linear gain in the power range needed for the tests. While at 3 MHz the behaviour of the system was found almost linear (Fig. 4.14), at 10 MHz the measurement in Fig. 4.15 shows ∼20 % of additional losses when increasing the input power.
In addition, the connection between the grid circuit and the grid of Final tube has been improved. The equivalent inductance of the connecting cable, in fact, resonates with the decoupling 10 nF capacitor of the grid of Final tube at ∼55 MHz. The

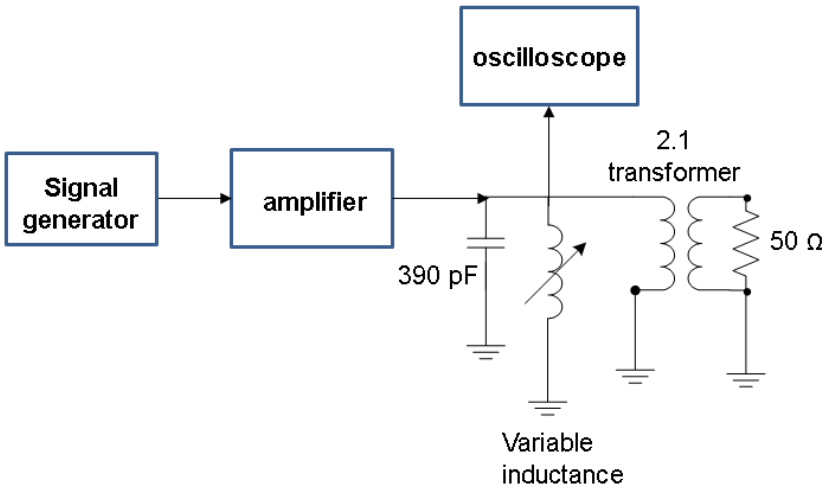

Figure 4.13: Set-up used to test the linearity of the grid circuit: an amplifier drives the transformer and the variable inductance. The latter resonates with the capacitances of the tubes (390 pF). The input power is increased by means of a signal generator. An oscilloscope measures the output across the device via a differential probe.

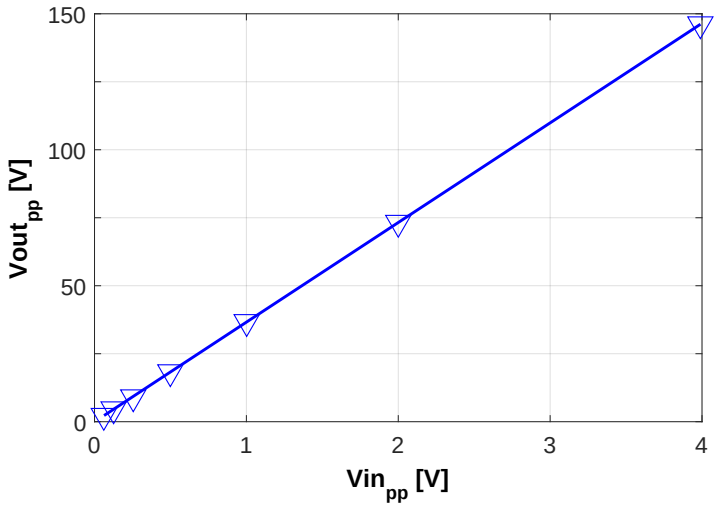

Figure 4.14: Response of the new grid transformer, when the grid circuit is driven by an increasing amplitude 3 MHz signal. Vin_{pp} is the input of the amplifier.

single cable has been replaced by three cables in parallel connected to three 3.3 nF capacitors. The equivalent inductance of the connection has been reduced, shifting this unwanted resonance to higher frequencies (Fig. 4.16).

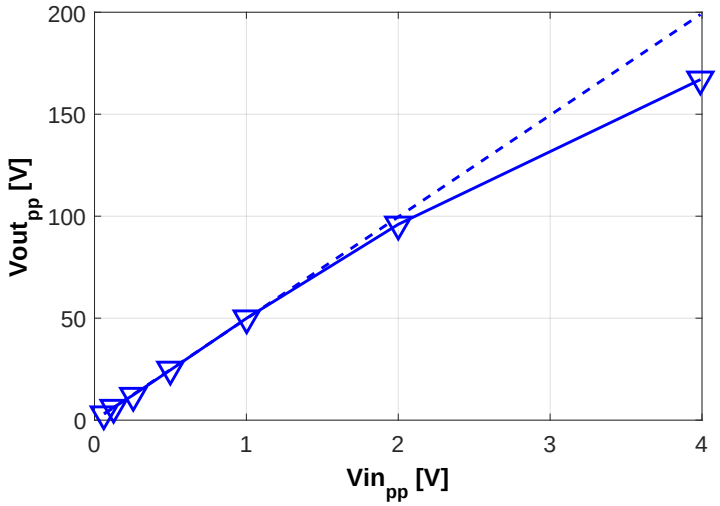

Figure 4.15: Response of the new grid transformer, when the grid circuit is driven by an increasing amplitude 10 MHz signal. Vin_{pp} is the input of the amplifier.

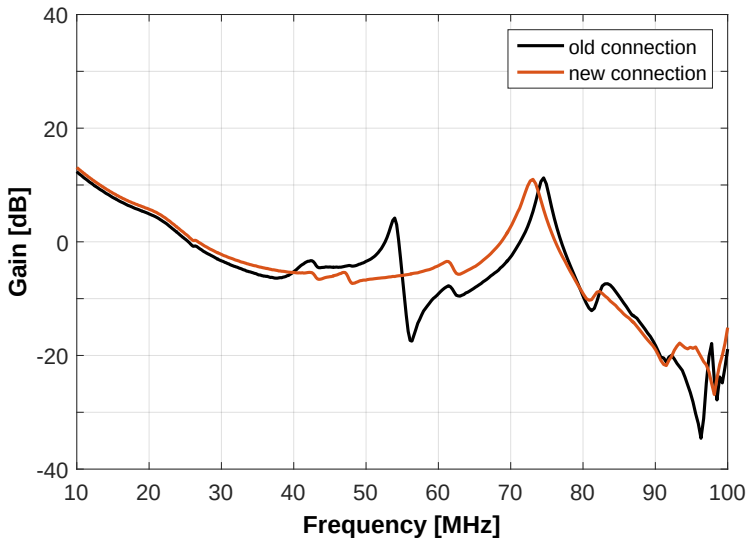

Figure 4.16: Response of the Driver connected to the Final with a standard cable (black trace) and with the improved connection (orange trance).

The new devices have been integrated in the amplifier and the consequent improvements on the local amplifier have been evaluated. Figures 4.17 and 4.18 show the measured transfer function of the local amplifier when the feedback is closed and open at 3 and 10 MHz.

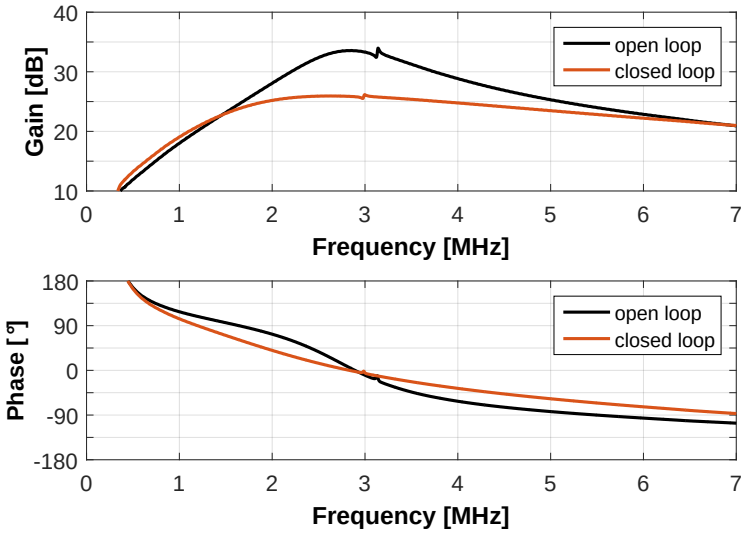

Figure 4.17: Gain and phase measurement of local amplifier at 3 MHz.

The values of gain, BW and Q extracted from the aforementioned measurement at 3 and 10 MHz are summarized in Tabs. 4.2 and 4.3.

	Gain [dB]	**BW [MHz]**	**Q**
loop open	33.57	1.36	2.09
loop closed	26	3.92	0.88

Table 4.2: Gain, BW and Q parameters of the local amplifier transfer function, when the feedback loop is open and closed at 3 MHz.

	Gain [dB]	**BW [MHz]**	**Q**
loop open	33.5	1.38	7.3
loop closed	25	3.4	2.9

Table 4.3: Gain, BW and Q parameters of the local amplifier transfer function, when the feedback loop is open and closed at 10 MHz.

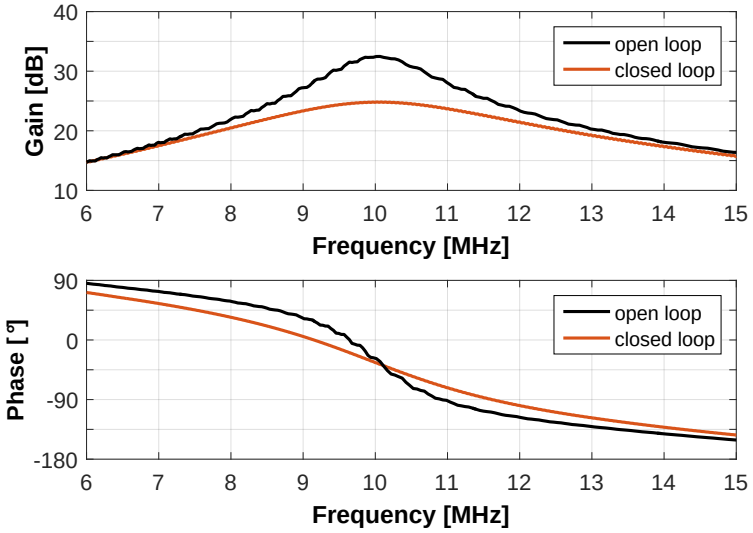

Figure 4.18: Gain and phase measurement of local amplifier at 10 MHz.

As a consequence of the listed modifications in this section, the Q of the closed loop transfer function of the local amplifier at 3 MHz has been reduced from 1.33 to 0.88. Additionally, in the new design of the local amplifier, the open loop gain at 3 and 10 MHz is almost the same, since the losses featured by the grid transformer at 10 MHz were reduced. Therefore, in the new design, the Q measured in open loop is higher, but because of the increased loop gain, the Q measured in closed loop is lower than in the previous configuration.

4.2.1 Stability margin measurements

After the installation of the new components, the stability margins of the local amplifier have been evaluated using a dummy circuit to reproduce the summing point circuit.

The loop gain has been measured as the transmission from the real to the dummy summing point, while the Final stage was not powered. The dummy circuit includes the input capacity of the Pre-driver tube, the biasing resistance and filter, the resistance of the generator, the load, the coupling capacity and the 40 dB attenuation probe components. The circuit reproduces quite well, in the range of frequency of interest, the behaviour of the real circuit. The measurements are shown in Fig. 4.19.

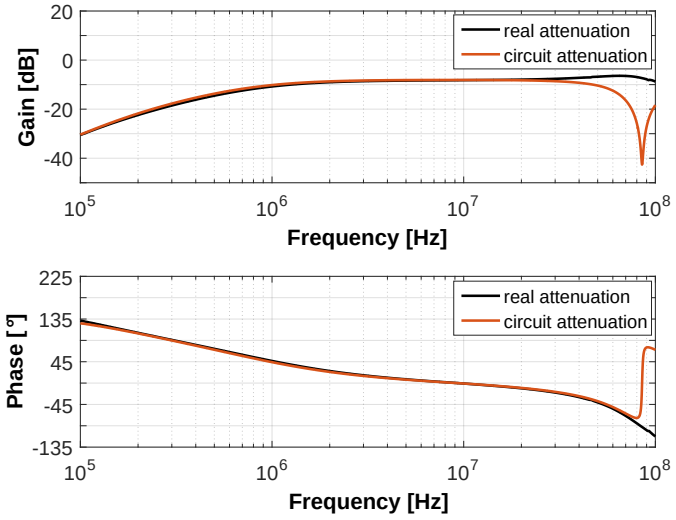

Figure 4.19: Comparison between the response of the real summing point and the dummy circuit.

The measurements of the local loop gain ($A \cdot \beta$) at 3 MHz and 10 MHz are illustrated in Figs. 4.20 and 4.21.

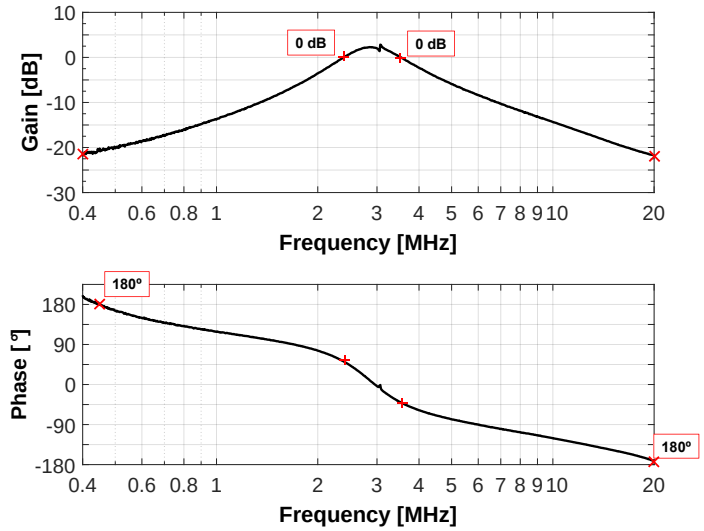

Figure 4.20: Loop gain and phase of the local amplifier at 3 MHz.

These measurements provide a better estimate of the loop gain. The latter, in fact,

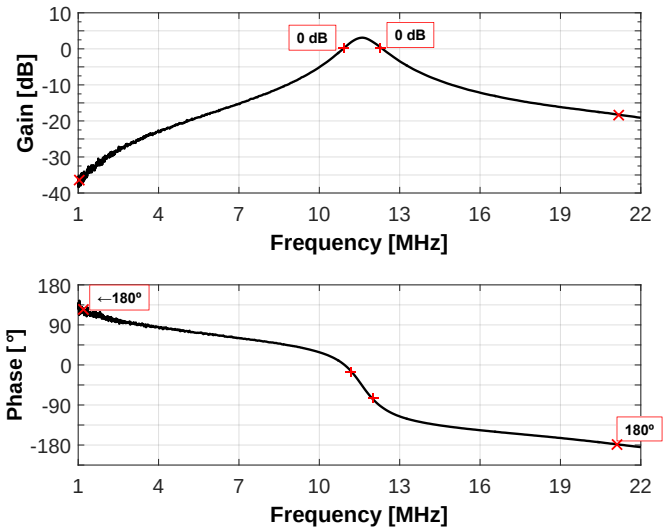

Figure 4.21: Loop gain and phase of the local amplifier at 10 MHz.

is normally evaluated as the ratio between the open loop gain and the closed loop gain at the resonance frequency. However, this approximation is only valid when $A \cdot \beta >> 1$. At 3 MHz the loop gain is ∼2.5 dB. The phase margins are evaluated measuring the phase, at the frequency where the loop gain is 0 dB:

$$m_{\varphi_{L,R}} = 180° - |\varphi(|A \cdot \beta| = 0\,\mathrm{dB})| \approx 145\,° \tag{4.3}$$

The gain margins are evaluated measuring the gain where the phase is 180 °:

$$m_{G_{L,R}}(\angle A \cdot \beta = 180°) \approx 20\,\mathrm{dB} \tag{4.4}$$

When the cavity in tuned at 10 MHz, the local resonator must be tuned at ∼12 MHz, in order to compensate the phase shift and keep the whole system stable, as already stated in Chap. 3.2.7. At this frequency, with a loop gain of ∼3.5 dB, the local amplifier is still stable, although the margins are lower.

$$\begin{aligned} m_{\varphi_L} &\approx 165\,° \\ m_{\varphi_R} &\approx 100\,° \end{aligned} \tag{4.5}$$

$$\begin{aligned} m_{G_L} &\approx 40\,\mathrm{dB} \\ m_{G_R} &\approx 20\,\mathrm{dB} \end{aligned} \tag{4.6}$$

The phase at the resonance frequency, in fact, is not zero, but $\sim 30\,^\circ$, which is the phase shift of the chain, mainly due to the Pre-driver phase shift and the length of the connecting cables.
The transfer function of the whole system has been measured (Fig. 4.22), in order to evaluate the new global loop gain.

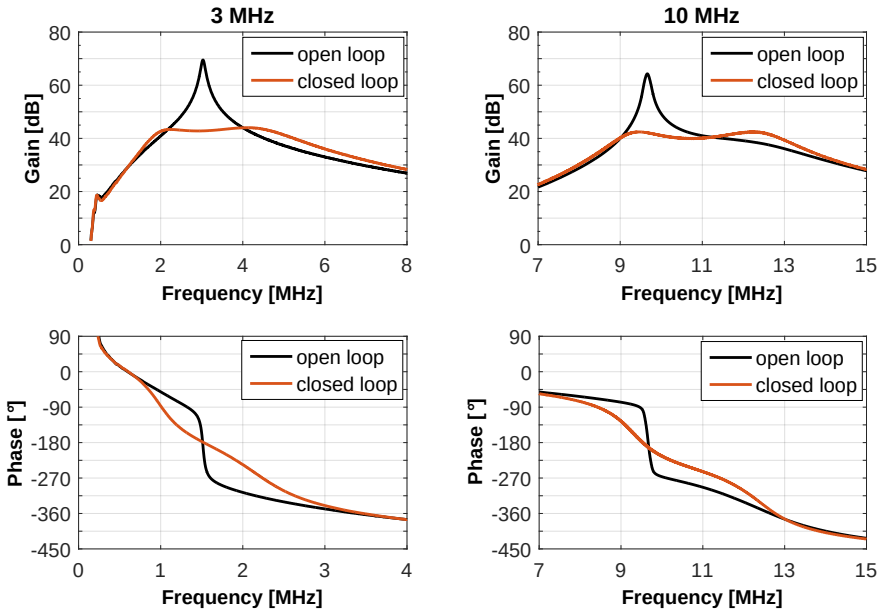

Figure 4.22: Whole amplifier transfer function in open and closed loop at 3 and 10 MHz.

On one hand, about 28 dB were obtained at 3 MHz. On the other hand, due of the large phase shift, only 23 dB of loop gain were reached at 10 MHz. It is worth noting that since the local resonator must be tuned at higher frequency, a consequent reduction of forward gain at the cavity resonance is observed.
In addition, the stability margins of the whole chain have been measured at 3 MHz (Fig. 4.23) and at 10 MHz (Fig. 4.24), using the dummy circuit.

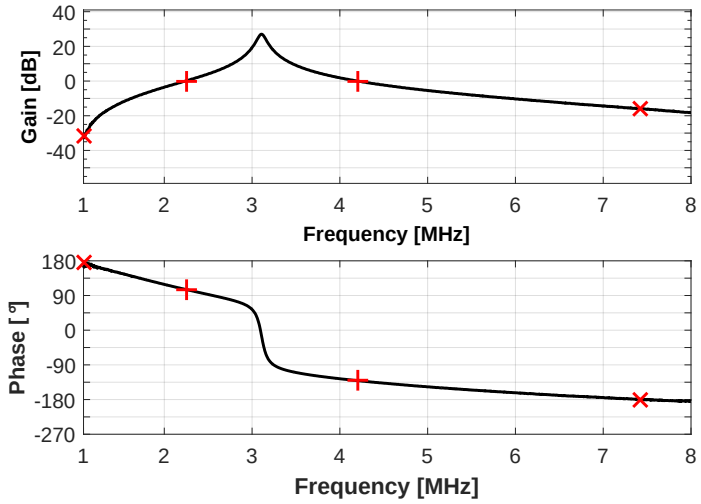

Figure 4.23: Loop gain and phase of the whole system at 3 MHz.

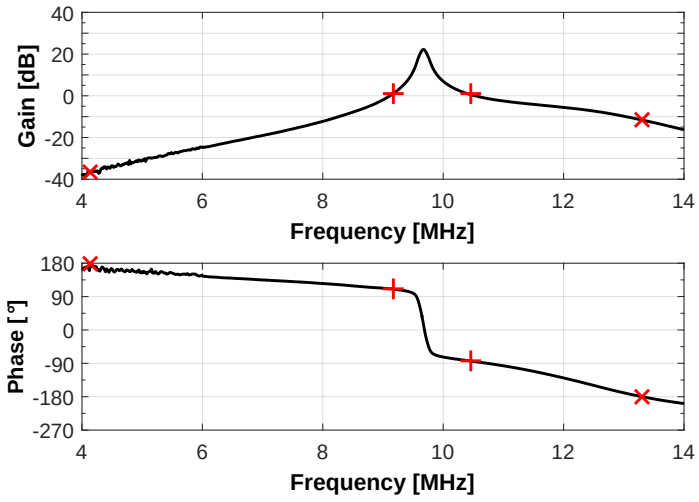

Figure 4.24: Loop gain and phase of the whole system at 10 MHz.

The measured stability margins are the following at 3 MHz:

$$\begin{aligned} m_{\varphi_L} &\approx 80\,^\circ \\ m_{\varphi_R} &\approx 52\,^\circ \end{aligned} \tag{4.7}$$

$$\begin{aligned} m_{G_L} &\approx 30\,\mathrm{dB} \\ m_{G_R} &\approx 17\,\mathrm{dB} \end{aligned} \tag{4.8}$$

and at 10 MHz:

$$\begin{aligned} m_{\varphi_L} &\approx 70\,^\circ \\ m_{\varphi_R} &\approx 100\,^\circ \end{aligned} \tag{4.9}$$

$$\begin{aligned} m_{G_L} &\approx 40\,\mathrm{dB} \\ m_{G_R} &\approx 12\,\mathrm{dB} \end{aligned} \tag{4.10}$$

Despite the amplifier is stable in the range of frequency of interest, higher loop gain is required at 10 MHz. The reduction of the impedance is crucial for the stability of the LHC-type beams, which are accelerated in the PS at this frequency.
In order to obtain higher loop gain at 10 MHz, an additional improvement, described in the following section, has been necessary.

4.3 New compensating network

The 30 ° phase shift between 3 and 10 MHz of the Pre-driver stage is one of the main limitations to the feedback improvement of the amplifier. In order to lower this phase shift and increase the bandwidth, the stage is equipped with a compensating network. The anode load of the Pre-driver consists of the input capacity of the Driver tubes in parallel with the Pre-driver anode choke, the 50 Ω load and the compensating network, as shown in Fig. 4.25. The 0.52 μH resonate with the capacitances at ∼12 MHz, reducing the Pre-driver phase shift between 9 MHz and 11 MHz by a few degrees. The impact of the compensating network on the Pre-driver gain and phase is shown in Fig. 4.26, where PSPICE simulation point out the difference between loading the Pre-driver stage with 50 Ω only (black trace) and with the compensating network (orange trace).

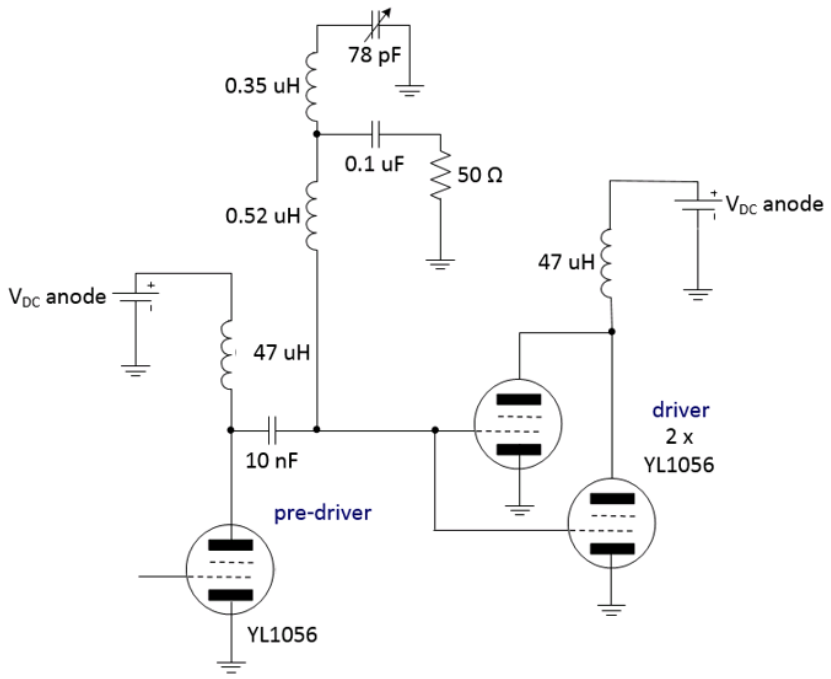

Figure 4.25: Pre-driver compensating network implemented in the standard configuration of the amplifier.

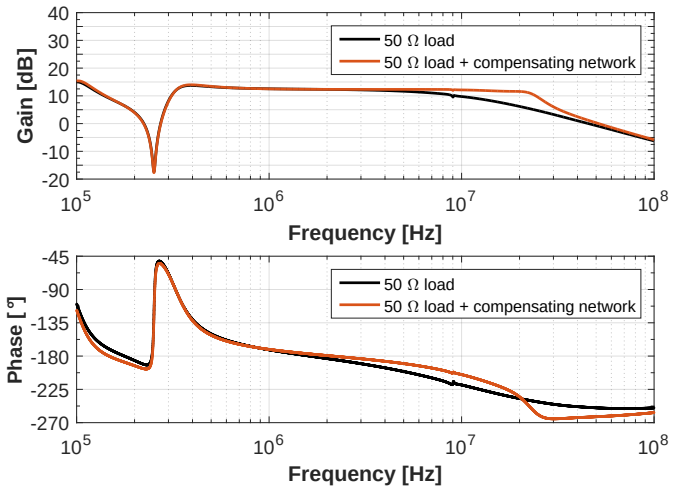

Figure 4.26: PSPICE simulations of the Pre-driver stage when loaded by the 50 Ω only (black trace) and by the compensating network used in the standard configuration of the amplifier (orange trace).

A further optimisation of this compensating network also took place; it has been modified to reduce the phase shift as much as possible. The new network is shown in Fig. 4.27.

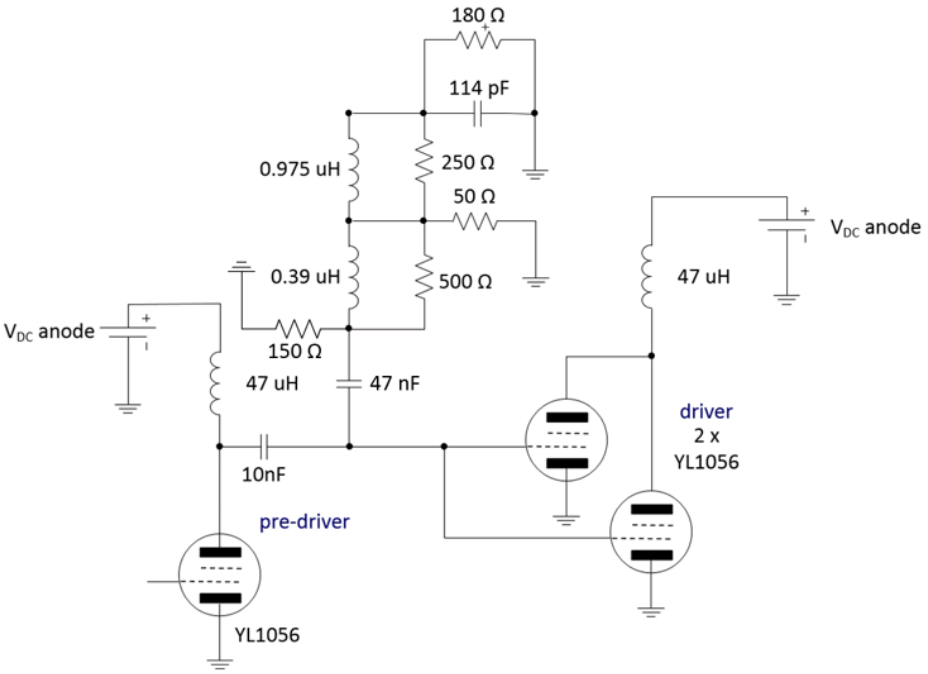

Figure 4.27: Circuital representation of the new compensating network.

The inductances and the capacitor of the network resonate with the tube input capacitance generating a resonance at about 15 MHz. The resistor values are chosen to adjust the Q of such a resonance, trying to keep as much as possible a constant gain of the stage in the operating frequency range. The equivalent resistive load of the Pre-driver is now reduced to $\sim 37\,\Omega$ and contributes to flatten the phase of the Pre-driver.

After the installation of the new compensating network, measurements confirmed that the shift between 3 and 10 MHz has been reduced from 30° to 5° (Fig. 4.28). The price of the improved phase of the first stage is a lower gain, featuring ~ 3 dB less than before.

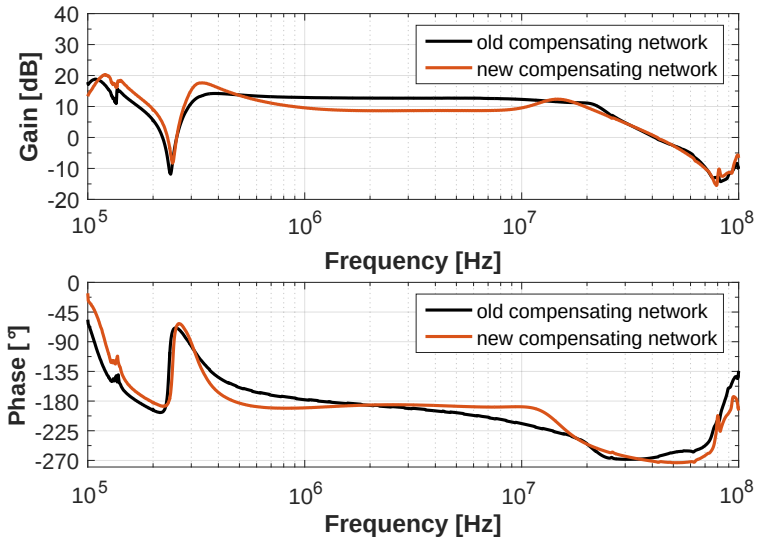

Figure 4.28: Measurements of the Pre-driver stage when loaded by the compensating network used in the standard configuration of the amplifier (back trace) and the new one (orange trace).

4.4 Further improvements

4.4.1 New 400 W driving amplifier

The 150 W Herfurth amplifier, that provides the RF input to the amplifier chain, has been replaced by a new driver, totally developed at CERN and able to deliver up to 400 W with a reduced harmonic content.

It is a solid-state based amplifier, which, differently from the old amplifier, has only one stage, made by two MOSFETs, used in push-pull configuration. The gain of the stage is 29 dB. In addition, it is coupled to a 4 W amplifier (33 dB gain) used as driver, in order to reach a total gain of 62 dB. Being close to the gain of the Herfurth amplifier, it allows keeping the same input signal amplitude. It is also characterized by a lower group delay if compared to the Herfurth amplifier.

The harmonic content is also reduced. Tabs. 4.4a and 4.4b show the values of H2 (second harmonic) and H3 (third harmonic) of the Herfurth and of the new driver, at 80 W output, which is the maximum power required at 10 MHz by a standard amplifier to reach 10 kV_p at the cavity gaps.

Freq	H2 [dBc]		H3 [dBc]	
	max	*min*	*max*	*min*
3 MHz	-27	-38	-20	-28
5 MHz	-24	-36	-22	-27
7.6 MHz	-23	-38	-22	-27
10 MHz	-22	-40	-23	-30

(a) Herfurth

Freq	H2 [dBc]	H3 [dBc]
3 MHz	-47	-36
5 MHz	-49	-32.8
7.6 MHz	-41.5	-27.2
10 MHz	-41.2	-30

(b) 400 W

Table 4.4: Harmonic content of the Herfurth and the new 400 W driver. In the first table the values of the maximum and the minimum values of the harmonic content, measured in the twelve Herfurth amplifier driving the PS cavities plus the spare and the test ones, are reported.

4.4.2 New BIAS system for the grid circuit

A new FPGA based circuit, that controls the biasing system of the new grid variable inductance, was built and installed. The control board converts a frequency input to a DC voltage controlling the power supply to provide the needed bias current to the grid circuit. This current changes the value of the grid inductance.
The resonant frequency of the grid circuit is not exactly the same of the resonant frequency of the cavity in the whole operating frequency range, but a detuning is necessary in order to compensate the phase shift accumulated in the chain.
In order to tune the equivalent grid resonator at the correct frequency for the stability of the whole amplifier, a look up table table was computed, containing the values of the needed bias current for the grid inductance to have a symmetric shape of the closed loop response of the whole amplifier chain. These values are measured in the operating range, from 2.7 MHz to 10.2 MHz every 500 kHz, and then fitted every 10 kHz, which corresponds to an increment of 12 mA.
The FPGA board has two inputs: the *coarse tuning* and the *fine tuning* currents of the bias circuit of cavity. The fine tuning current system, which is active once 700 V_p RF have been reached at each gap, compensates for the variations of the ferrite behaviour due to the changes of voltage amplitude on the gap.
The sum of the coarse and fine tuning current is scaled and converted to an equivalent current for the variable inductance, according to the computed table.

4.5 Results

The upgraded amplifier, implementing all the described modifications, is characterized by a loop gain of about 25 dB at 3 MHz and 29 dB at 10 MHz (Fig. 4.29).

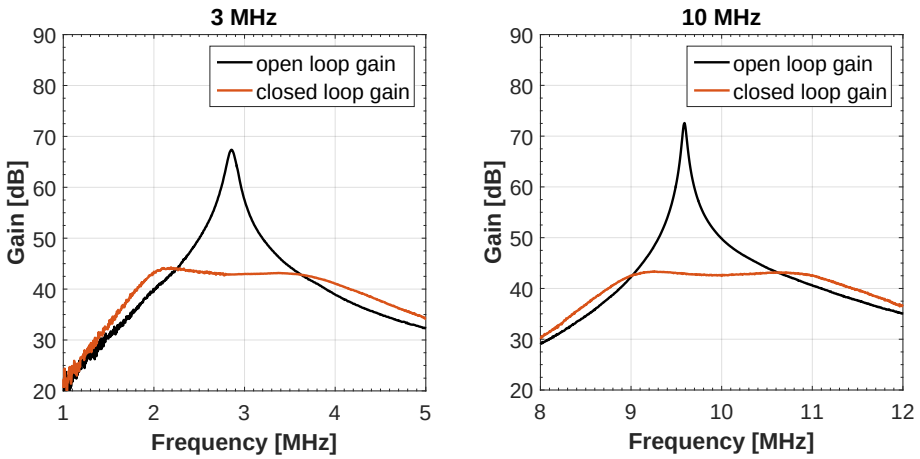

Figure 4.29: Open and closed loop gain of the amplifier at 3 and 10 MHz.

Measurements of the stability margins, illustrated in Figs. 4.30 and 4.31, have been performed at 3 MHz:

$$m_{\varphi_L} \approx 70\,^\circ \qquad m_{\varphi_R} \approx 60\,^\circ \tag{4.11}$$

$$m_{G_L} \approx 40\,\mathrm{dB} \qquad m_{G_R} \approx 23\,\mathrm{dB} \tag{4.12}$$

and at 10 MHz:

$$m_{\varphi_L} \approx 75\,^\circ \qquad m_{\varphi_R} \approx 70\,^\circ \tag{4.13}$$

$$m_{G_L} \approx 40\,\mathrm{dB} \qquad m_{G_R} \approx 15\,\mathrm{dB} \tag{4.14}$$

The amplifier can provide a stable operation even when operated at maximum input power.

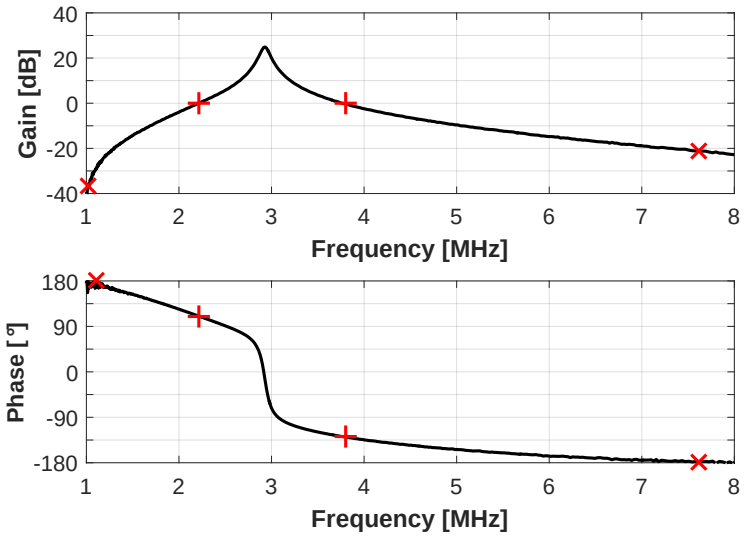

Figure 4.30: Loop gain of the new amplifier at 3 MHz.

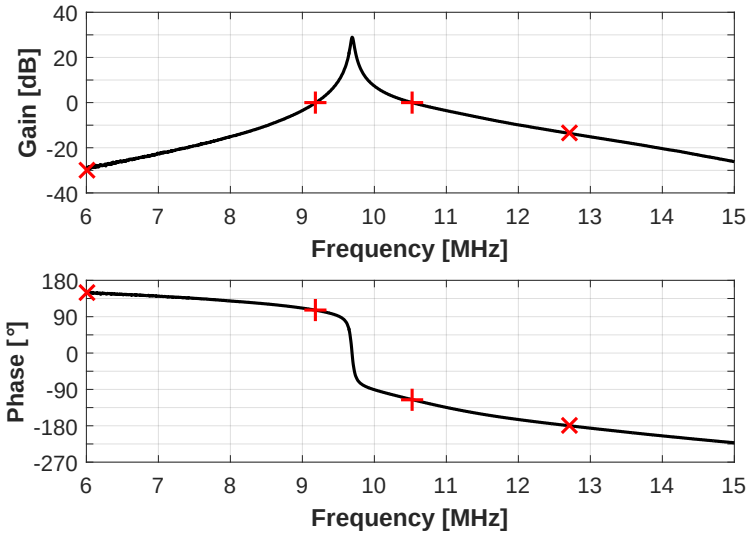

Figure 4.31: Loop gain of the new amplifier at 10 MHz.

In order to evaluate the impedance reduction achieved with the new amplifier, measurements were carried out using the set-up illustrated in Fig. 4.32.
The value of the measured gap impedance does not correspond to the impedance as seen by the beam. The latter is extracted using a correct interpretation of the beam-cavity interaction, which will be treated in the last chapter of this thesis. However, the measurement method remains valid to get an approximation of the cavity impedance reduction provided by the upgraded amplifier.

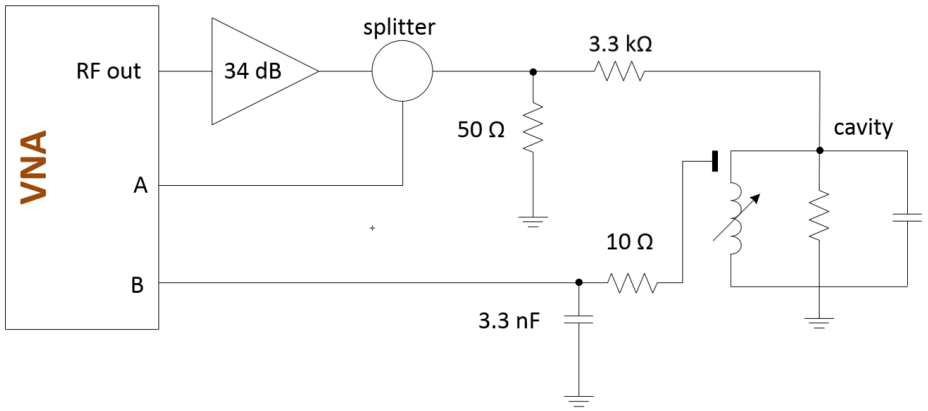

Figure 4.32: Test set-up for the cavity gap impedance measurements.

According to Fig. 4.32, an almost constant current is injected in the cavity gap via a 3.3 kΩ resistor. The voltage at the gap divided by the current, B/A, is measured: this is proportional to the equivalent gap impedance. The measurement is first performed with the amplifier switched off and one cavity gap is loaded by a 315 Ω resistor. This value corresponds to the impedance measured on a cavity with 20 dB of loop gain [40] and is used as reference for comparison. The resistor is then removed and the amplifier is switched on. The difference in dB between these two measurements allows to calculate the gap impedance reduction that has been achieved. The estimated error of the measurement amounts to ∼10 %, because of the finite value of the injecting resistor. The measured impedance is 130 Ω at 3 MHz and 100 Ω at 10 MHz, as shown in Fig. 4.33.
To crosscheck the impedance measurements, PSPICE simulations of the standard amplifier and of the upgraded one have been performed. As already stated, the highest impedance reduction with the standard architecture of the 10 MHz system, is

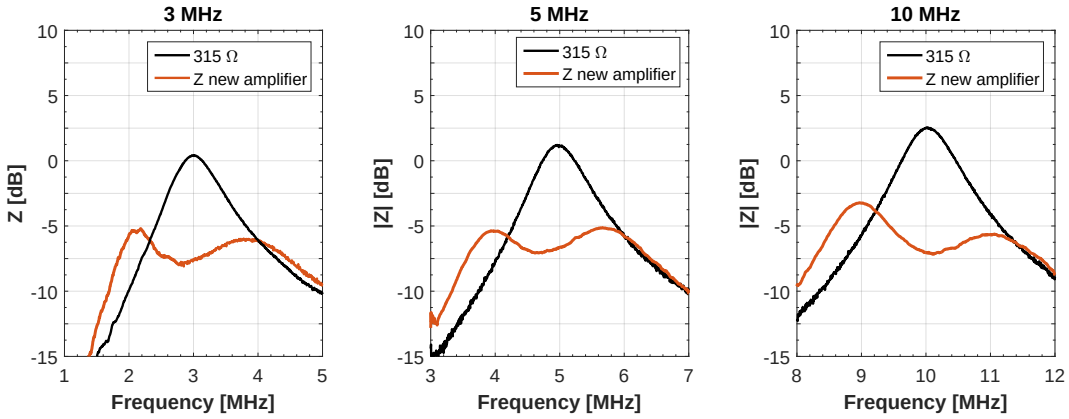

Figure 4.33: Measurements of the impedance reduction of the upgraded amplifier. The value of the impedance is evaluated using a 315 Ω resistor as a reference.

∼25-26 dB ($A \cdot \beta$). The value of β is already the maximum acceptable, being limited by the maximum power at the input of the amplifier chain.

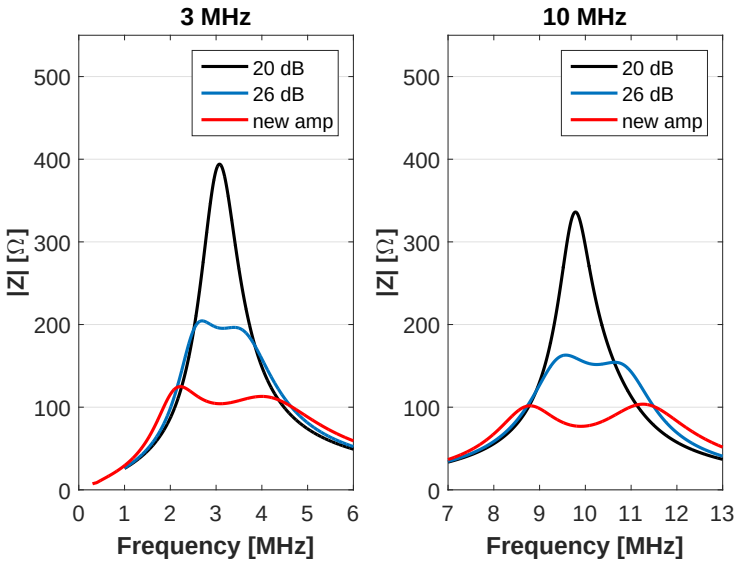

Figure 4.34: Simulations of the gap impedance of a standard amplifier with 20 and 26 dB of loop gain and the new amplifier.

Figure 4.34 shows a comparison of the gap impedance of a standard amplifier with 20 dB of loop gain and the new one. In addition, the results from simulations of a standard amplifier with ∼26 dB of loop gain are presented to better visualize the improvements.

Chapter 5

Ferrite studies

This chapter, in the context of the upgrade of the 10 MHz system, describes a new ferrite based grid resonator prototype that has been developed to replace the existing one. The analysis and the qualification of this prototype are detailed in the text. An accurate characterisation of the ferrite magnetic properties was essential during the development of the new device, to evaluate its tunability range and losses. To measure and evaluate the ferrite complex permeability and its dependence on external bias field a new technique has been developed. In addition, an alternative biasing technique was tested to reduce the resonator losses.
It is worth mentioning that this measurement technique has been applied for the measurements of the ferrite rings used as core of the 10 MHz cavity and helped for the development of an accurate numerical model, as it will be described in the next chapter.

5.1 Permeability definition

When a driving magnetic field H is applied to a magnetic material, the domains progressively align with it (magnetization process) [53]. The resulting flux density B is composed of both the contribution of the free space field and the aligned domains:

$$B = \mu_0(H + M) \tag{5.1}$$

where μ_0 is the permeability of the free space and M is the magnetization. The relative permeability of the material is defined as:

$$\mu_r = \frac{1}{\mu_0}\frac{B}{H} \tag{5.2}$$

The permeability observed when an RF magnetic field is superimposed on a static bias field H_{BIAS}, is called the incremental permeability and reads:

$$\mu_r = \frac{1}{\mu_0}\left[\frac{\Delta B}{\Delta H}\right]_{H_{BIAS}} \tag{5.3}$$

5.2 Evaluation of ferrite materials permeability

Ferrite materials are used in the accelerator field as core of the resonators to reduce the longitudinal size and for frequency tuning purposes. The application of the ferrite produces an increase of the losses and of the equivalent inductance, since ferrite materials are characterized by their complex permeability μ_r expressed by: $\mu_r = \mu' - j\mu''$, where μ' represents the inductance and μ'' represents the magnetic losses.
When exposed to a magnetic orthogonal or parallel bias field, a reduction of the ferrite incremental permeability can be observed. Since the resonant frequency varies with the relative permeability as $1/\sqrt{\mu_r}$, it is therefore possible to tune a resonator by applying an external field.
In the following, two different approaches used for the evaluation of the ferrites magnetic properties are described.

5.2.1 Coaxial line theory

A first approach is based on the coaxial line theory [54], according to which, the input impedance of a shorted coaxial line (Fig. 5.1) in the loss-less case reads:

$$Z(-l) = jX(-l) = jZ_0 \tan \beta l \tag{5.4}$$

with $X(-l)$ being the line reactance, β being the propagation constant, l being the line length and $Z_0 = 60\ln(\frac{D}{d})$ being the characteristic impedance of a cylindrical coaxial line, where D denotes the inner diameter of the outer conductor and d the outer diameter of the inner conductor.

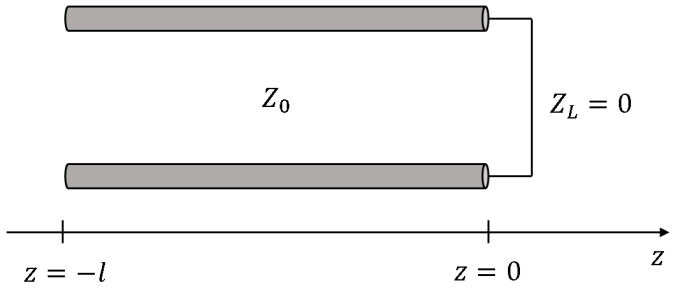

Figure 5.1: Shorted coaxial line.

The line impedance $Z(-l) = jX(-l)$ results inductive ($X(-l) > 0$) when $l < \lambda/4$. Assuming $X(-l) = \omega L_0$, from Eq. (5.4) one gets:

$$L_0 = \frac{X(-l)}{\omega} = \frac{Z_0}{\omega}\tan\beta l. \tag{5.5}$$

Moreover, the approximation $\tan\beta l \approx \beta l$ is valid when $l < \lambda_0/10$, then:

$$L_0 = \frac{Z_0\beta l}{\omega} = \frac{Z_0 l}{\omega}\frac{2\pi}{\lambda_0} = \frac{Z_0 l}{c}, \tag{5.6}$$

with $\lambda_0 = \frac{2\pi}{\beta}$ being the vacuum wavelength and c being the speed of light in vacuum. However, if the coaxial line is filled with ferrite its input impedance reads:

$$L_{eq} = \frac{Z_L l}{\omega}\frac{2\pi}{\lambda} = \frac{2\pi}{\omega}\frac{Z_0\sqrt{\frac{\mu_r}{\epsilon_r}}l}{\lambda_0\frac{1}{\sqrt{\mu_r\epsilon_r}}} = \frac{Z_0\mu_r l}{c} \tag{5.7}$$

where $Z_L = Z_0\sqrt{\frac{\mu_r}{\epsilon_r}}$ is the characteristic impedance of the line, and $\lambda = \frac{\lambda_0}{\sqrt{\mu_r\epsilon_r}}$ is the wavelength in the medium.

5.2.2 Rectangular cross section approximation

A second approach to evaluate the ferrite permeability uses the rectangular cross section toroid approximation (Fig. 5.2).

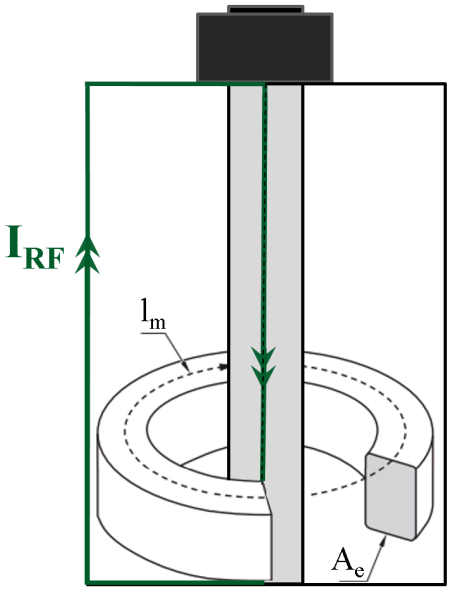

Figure 5.2: Shorted coaxial line filled with a ferrite ring. I_{RF} indicates the path of the RF current in the sample holder, l_{m_f} is the magnetic length and A_{e_f} is the section of the ring crossed by the RF field lines.

The inductance of a ferrite-cored coil is often described by:

$$L = N^2 \times A_L \tag{5.8}$$

with N being the number of turns of wire in the coil wound around the ferrite and A_L being the inductance factor, which describes the coil ability to provide inductance [53]. The inductance factor, A_L, depends on the length and the cross-sectional area of the ferrite toroid. In our particular case the equivalent number of turns made by the RF path (see Fig. 5.2) is equal to 1, thus the inductance of the ferrite toroid reads:

$$L = \mu_r \mu_0 \frac{A_{e_f}}{l_{m_f}}, \tag{5.9}$$

where μ_r is the ferrite magnetic permeability, μ_0 is the vacuum magnetic permeability,

A_{e_f} is the equivalent area crossed by the RF magnetic field lines and l_{m_f} is the equivalent magnetic length.

5.3 Permeability measurement technique

As observed in the previous sections the ferrite permeability could be extracted from the input impedance of a ferrite resonator. In the following, we describe our technique used for the input impedance measurement of a ferrite ring under test and the evaluation of its permeability, according to the two aforementioned approximations. Moreover, the measurements of the ferrite parameters have been carried out with and without a magnetic bias field.

5.3.1 Unbiased measurement

The measurement test-set consists in a copper coaxial line resonator with one shorted end, partially filled with one or more toroidal shaped samples. At the shorted end, where the toroids will be placed, the electric field is minimum, while the magnetic field is maximum easing the measurement of the magnetic properties [55].
In order to avoid resonance effects, the height of the sample under study (ferrite ring) and its holder have to be $< \lambda/4$. Ferrite samples of different shapes and materials have been characterized; that resulted in most of the cases in re-designing the sample holders to allow the implementation of the needed connections and a better fitting of the ferrite under test within the structure.
The ferrite characteristics are calculated from the input impedance of the device under test. The latter is inferred from the reflection coefficient measurements performed with a Vector Network Analyzer (VNA).
An OSM (Open-Short-Matched) one-port calibration on the N-type test cables is required to get accurate measurements. Fig. 5.3 is a schematic drawing of the coaxial line set-up.
The S_{11} parameter calculated at the short end is obtained by normalizing the measured reflection coefficient of the sample holder filled by the ferrite sample $S_{11_{filled}}$ to

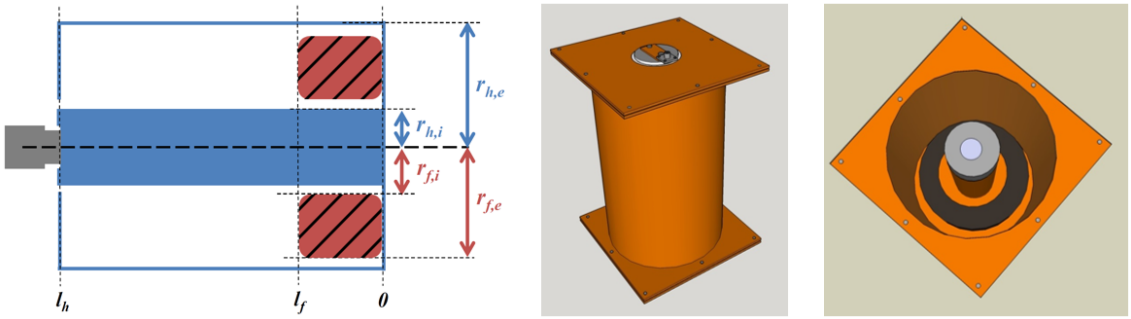

Figure 5.3: Schematic drawing of the experimental set-up. The metallic holder (blue) houses a toroidal shaped ferrite (red) and features a connector (grey) used for S_{11} measurements. The figures on the right show an example of shorted coaxial sample holder.

the one of the empty sample holder $S_{11_{empty}}$:

$$S_{11} = \frac{S_{11_{filled}}}{S_{11_{empty}}}. \tag{5.10}$$

Figures. 5.4 and 5.5 illustrate a typical result of the reflection parameter measurement for a shorted coaxial line partially filled with ferrite. As shown in Fig. 5.5, the equivalent length of a coaxial line increases when filled with the ferrite sample; similarly an increase of the losses is clearly visible (green curve Fig. 5.5). The effect of the normalization allows to move the reference plane from "l_h" to "l_f" in Fig. 5.3, since the electromagnetic properties of the ferrite ring (red curve Fig. 5.5) are contained between the planes "l_f" and "0".
The input impedance Z_f at the reference plane "l_f" is a complex number and can be calculated from the reflection coefficient:

$$Z_f = Z_c \frac{1 + S_{11}}{1 - S_{11}} \tag{5.11}$$

where $Z_c = 50\,\Omega$ is the characteristic impedance of the VNA and the connection cables.
Following the shorted coaxial line theory, described in Sec. 5.2, Z_f can also be ex-

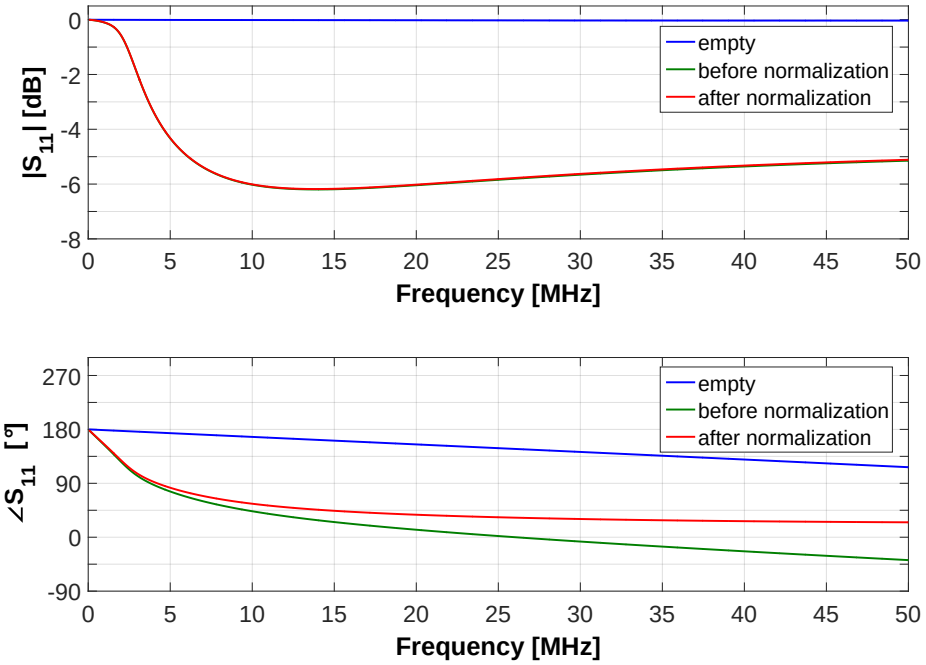

Figure 5.4: Example of S_{11} results for a shorted coaxial line.

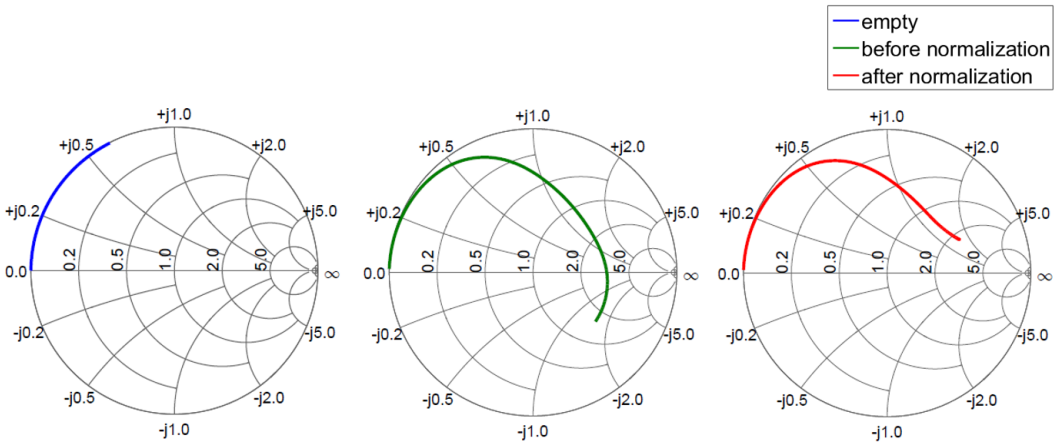

Figure 5.5: Smith chart format measurement results for a shorted coaxial line.

pressed by:

$$Z_f = jZ_s \tan(\beta_f l_f) \tag{5.12}$$

with $Z_s = Z_0\sqrt{\frac{\mu_e}{\epsilon_e}}$ being the impedance of a coaxial line filled with one or more ferrite rings, Z_0 the characteristic impedance of the empty sample holder (depending on its geometry), l_f the ferrite length and $\beta_f = \frac{2\pi}{\lambda_0}\sqrt{\mu_e\epsilon_e}$ the propagation constant where μ_e and ϵ_e are the permeability and the permittivity measured between the planes "l_f" and "0".

If the ferrite length is much smaller than the wavelength: $l_f < \lambda/10$, Eq. 5.12 can be approximated as:

$$\begin{aligned} Z_f &\simeq jZ_s\beta_f l_f \\ &= jZ_0\sqrt{\frac{\mu_e}{\epsilon_e}}\frac{2\pi}{\lambda}l_f \\ &= jZ_0\sqrt{\frac{\mu_e}{\epsilon_e}}\frac{2\pi l_f}{\lambda_0}\sqrt{\mu_e}\sqrt{\epsilon_e} \\ &= jZ_0\frac{2\pi l_f}{\lambda_0}(\mu_e' - j\mu_e''). \end{aligned} \tag{5.13}$$

Since Z_f is a complex number, one can calculate μ_e' and μ_e'' from the measured real and imaginary part of Z_f:

$$\Im(Z_f) = \omega L_{eq_{im}} = Z_0\frac{2\pi l_f}{\lambda_0}\mu_e' \tag{5.14}$$

$$\Re(Z_f) = \omega L_{eq_{re}} = Z_0\frac{2\pi l_f}{\lambda_0}\mu_e''. \tag{5.15}$$

Then:

$$\mu_e' = \frac{L_{eq_{im}}c}{Z_0 l_f} \tag{5.16}$$

$$\mu_e'' = \frac{L_{eq_{re}}c}{Z_0 l_f}. \tag{5.17}$$

Equivalently the magnetic properties of the ferrite material can be extracted from Z_f, by using the rectangular cross section approximation of Eq. 5.9, as shown in the

following:

$$\Im(Z_f) = \omega L_{eq_{im}} = \omega \mu_0 \mu'_e \frac{A_{e_f}}{l_{m_f}} \tag{5.18}$$

$$\Im(Z_f) = \omega L_{eq_{re}} = \omega \mu_0 \mu''_e \frac{A_{e_f}}{l_{m_f}}. \tag{5.19}$$

Then:

$$\mu'_e = \frac{L_{eq_{im}} l_{m_f}}{A_{e_f} \mu_0} \tag{5.20}$$

$$\mu''_e = \frac{L_{eq_{re}} l_{m_f}}{A_{e_f} \mu_0}. \tag{5.21}$$

The figure of merit for the ferrite material can be also calculated:

$$Q = \frac{\Im(Z_f)}{\Re(Z_f)} = \frac{\mu'_e}{\mu''_e}. \tag{5.22}$$

If the ferrite completely fills the sample holder, we obtain $\mu_e = \mu_r$. However, in our measurements set-up, a radial air gap between the ferrite ring and the inner and outer conductor has to be taken into account (Fig. 5.6). In order to get μ_r, a gap correction, computed following [56], must be applied.

5.3.1.1 Air gap correction

For a current i flowing in the coaxial line, the inductance per unit length L_t is:

$$\begin{aligned} L_t \cdot i &= \int_{r_1}^{r_4} B \, dr \\ &= \int_{r_1}^{r_2} \mu_0 \frac{i}{2\pi r} dr + \int_{r_2}^{r_3} \mu_r \mu_0 \frac{i}{2\pi r} dr + \int_{r_3}^{r_4} \mu_0 \frac{i}{2\pi r} dr \end{aligned} \tag{5.23}$$

where $B = \mu_0 \mu_e \frac{i}{2\pi r}$ is the magnetic field in a coaxial line at radius r, μ_0 is the free space permeability and μ_r the ferrite permeability. From Eq. 5.23 we obtain:

$$L_t = \frac{\mu_0}{2\pi} \ln \frac{r_4}{r_3} + \frac{\mu_r \mu_0}{2\pi} \ln \frac{r_3}{r_2} + \frac{\mu_0}{2\pi} \ln \frac{r_2}{r_1}. \tag{5.24}$$

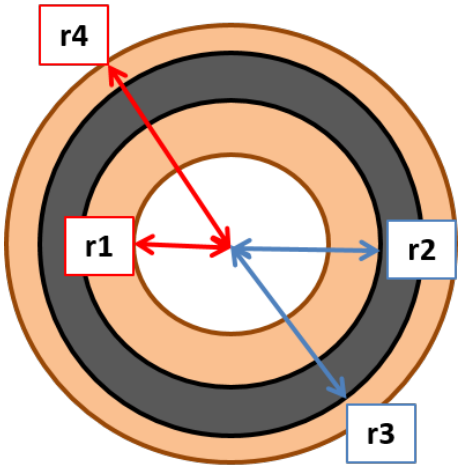

Figure 5.6: Radial air gap presence between the ferrite ring and the inner and outer conductor: the dark grey ring represents the ferrite toroid sit in the copper sample holder (bigger orange ring).

that can be also expressed as:

$$L_t = \frac{\mu_e \mu_0}{2\pi} \ln \frac{r_4}{r_1}. \tag{5.25}$$

Now we can finally calculate μ_r:

$$\frac{\mu_e \mu_0}{2\pi} \ln \frac{r_4}{r_1} = \frac{\mu_0}{2\pi} \ln \frac{r_4}{r_3} + \frac{\mu_r \mu_0}{2\pi} \ln \frac{r_3}{r_2} + \frac{\mu_0}{2\pi} \ln \frac{r_2}{r_1} \tag{5.26}$$

$$\mu_r = \frac{\mu_e \ln \frac{r_4}{r_1} - \ln \frac{r_4}{r_3} - \ln \frac{r_2}{r_1}}{\ln \frac{r_3}{r_2}}. \tag{5.27}$$

In the rectangular cross section approximation case, according to the set-up shown in Fig. 5.3, $A_{e_f} = l_f(r_{f,e} - r_{f,i})$ is the equivalent area of the ferrite sample crossed by the RF magnetic field lines and $l_{m_f} = \pi(r_{f,e} + r_{f,i})$ is the equivalent magnetic length of the sample. If the ferrite does not completely fill the sample holder, Eqs. 5.18 and 5.19 are no longer valid and the magnetic flux through the air gap must be taken into account.

In this case the equivalent inductance L_{eq} reads:

$$L_{eq} = L_f + L_{air} \tag{5.28}$$

where L_f is the equivalent inductance of the ferrite sample and L_{air} is the equivalent inductance of the portion of the sample holder filled of vacuum. It follows:

$$L_{eq} = \mu_0 \left(\frac{A_{e_{tot}}}{l_{m_{tot}}} - \frac{A_{e_f}}{l_{m_f}} \right) + \mu_0 \mu_r \left(\frac{A_{e_f}}{l_{m_f}} \right) \tag{5.29}$$

where $A_{e_{tot}} = l_f(r_{h,e} - r_{h,i})$ is the surface of the sample holder, between the planes "l_f" and "0" of Fig. 5.3, crossed by the magnetic field lines and $l_{m_{tot}} = \pi(r_{h,e} + r_{h,i})$ is the magnetic length of the sample holder.

5.3.1.2 Measurements results

In order to crosscheck the validity of the technique, the magnetic properties of a chosen ferrite have been evaluated using both the two aforementioned approaches (coaxial line vs. rectangular cross-section approximation) and an independent data analysis method [57], that takes into account more parameters of the test set geometry. The results of the comparison are reported in Fig. 5.7.
It is worth noting that the three approaches provide coherent estimations of μ_r' and μ_r'' and are in good agreement with each other; however the coaxial line theory was adopted throughout the rest of the analysis presented in this study.

5.3.2 Biased measurement technique

Since we were interested in the characterization of the ferrites at different working frequencies, for our cavity and the amplifier studies, we have developed a measurement technique that allows to change the ferrite properties with an external magnetic field. The orientation of the external DC field applied can be either orthogonal or parallel with respect to the magnetic RF field.
For the parallel bias case ($H_{RF} \parallel H_{BIAS}$), the effective RF permeability is the well known result:

$$\mu_e = \frac{1}{\mu_0} \frac{\partial B}{\partial H} \tag{5.30}$$

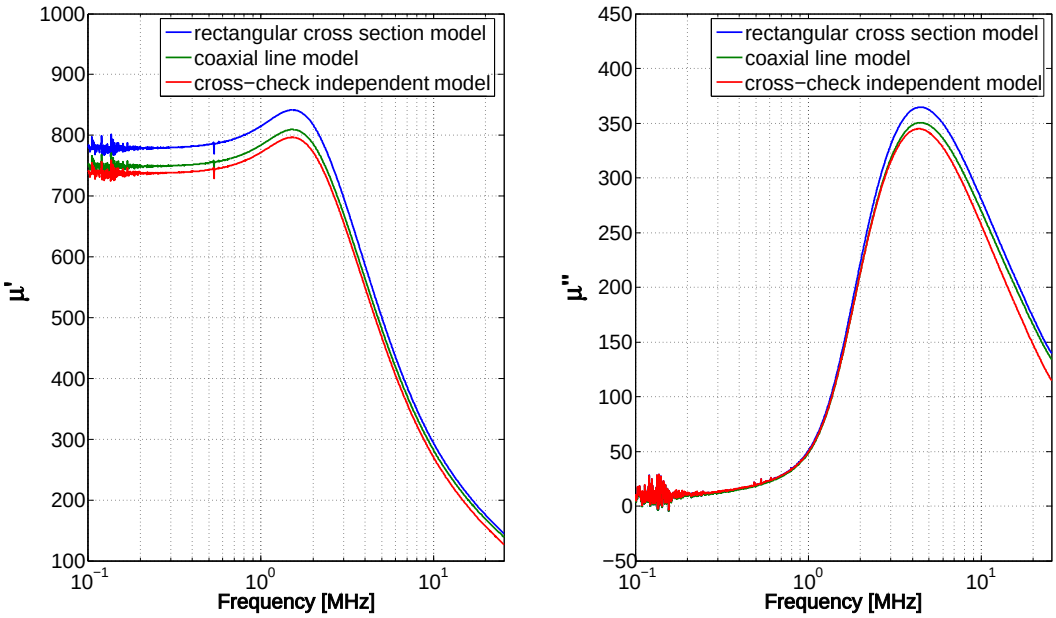

Figure 5.7: 4s2 ferrite parameters evaluated through three different methods.

The permeability is therefore proportional to the slope of the tangent line to the B-H curve (Fig. 5.8).

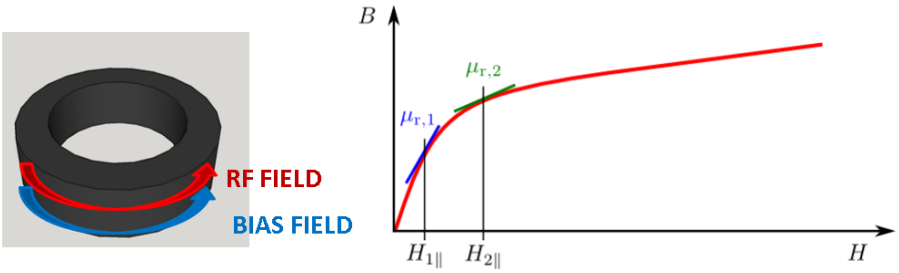

Figure 5.8: Case 1) Bias field parallel to the RF field. In the B-H curve, increasing $H_{1\parallel}$ to $H_{2\parallel}$ shifts $\mu_{r,1}$ to $\mu_{r,2}$.

In the perpendicular bias case ($H_{RF} \perp H_{BIAS}$), the relative permeability reduces to the expression:

$$\mu_e = \frac{1}{\mu_0}\frac{B}{H} \tag{5.31}$$

The permeability is in this case proportional to the slope of the secant from origin to

the B-H curve (Fig. 5.9) [58].

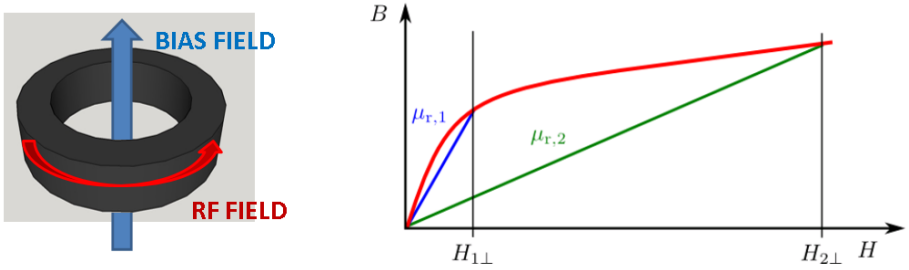

Figure 5.9: Case 2) Bias field perpendicular to the RF field. In the B-H curve, increasing $H_{1\perp}$ to $H_{2\perp}$ shifts $\mu_{r,1}$ to $\mu_{r,2}$.

Operating in the perpendicular bias mode would require a significantly larger bias field range and would make the design of the bias power supply more difficult and expensive.
Ferrite materials are magnetically lossy at low magnetization and the losses become smaller at high magnetization. This reduction is more significant when an orthogonal bias field is applied, because the operating point is closer to saturating magnetization values [59].
For our studies, the parallel bias has been introduced using a special set-up where a power supply is used to provide the current to the sample holder along with the RF through a T-connection, as sketched in Fig. 5.10.
Since the RF impedance of the DC power supply is below 5 Ω in the frequency range of interest, an RF choke coil is necessary to block the RF propagating towards the output of the power supply. Such a set-up can withstand a DC current up to 50 A.

5.3.2.1 Measurements results

Figures 5.11 and 5.12 show the results of the measurements performed following the described technique and the resulting permeability variation due to the application of a bias current up to 40 A on several ferrite samples.
It is important to note that an accurate VNA calibration is crucial for the measurement accuracy, which is not easy to perform since it is sensitive to bad contacts or instrument drifts.

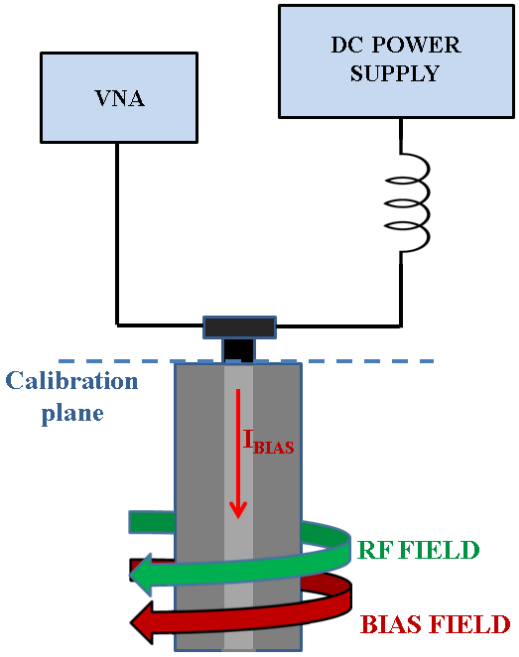

Figure 5.10: Set-up used for measuring ferrite characteristics, with a parallel bias field (current up to 50 A).

The perpendicular bias option was also used for our studies and it was provided either by means of a cylindrical solenoid or by windings put around the resonator. In particular, this option was investigated for the development of a new device, described in the following section, during the upgrade process of the 10 MHz feedback amplifier.

5.4 3-10 MHz PS grid resonator

In the framework of the upgrade of the PS 10 MHz system a Final grid resonator tunable in a frequency range from 3 to 10 MHz was designed.
In the early design of the upgraded prototype amplifier, the original Final grid circuit, described in Chap. 3.2.4, was replaced by three independent devices based on the transmission line technology:

- the 50 to 200 Ω transformation was provided by a 1:2 Ruthroff transformer [50];

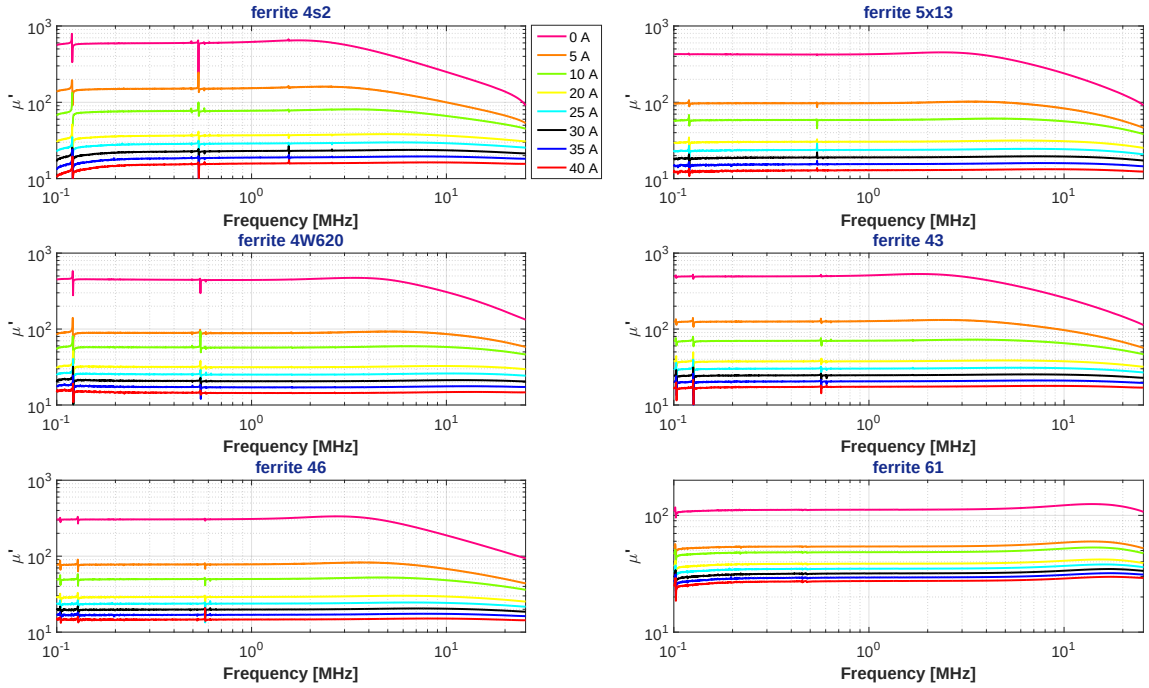

Figure 5.11: μ' variation of several ferrite samples, due to the application of a parallel bias field.

- the phase inverter consisted of a coaxial cable wound by ferrite;
- the new variable inductance was made of two brass coaxial lines shorted on one end, both lines completely filled with ferrite rings.

A prototype of the variable inductance is shown in Fig. 5.13.
A PCB was designed to connect the two lines in parallel. It also includes the sockets for the bias current connections, the capacitors decoupling the DC current from the RF paths, and the pins for the connections to the other devices of the resonator (Fig. 5.14).
The bias field was applied in opposite directions on each line, to reduce to zero the total RF voltage induced in the DC biasing path. It is worth mentioning that the two lines solution was adopted to keep the dissipated power per volume unit below the ferrite limits.
At an early stage of the variable inductance design, the two coaxial lines were biased by means of orthogonal fields generated by windings around each resonator. To

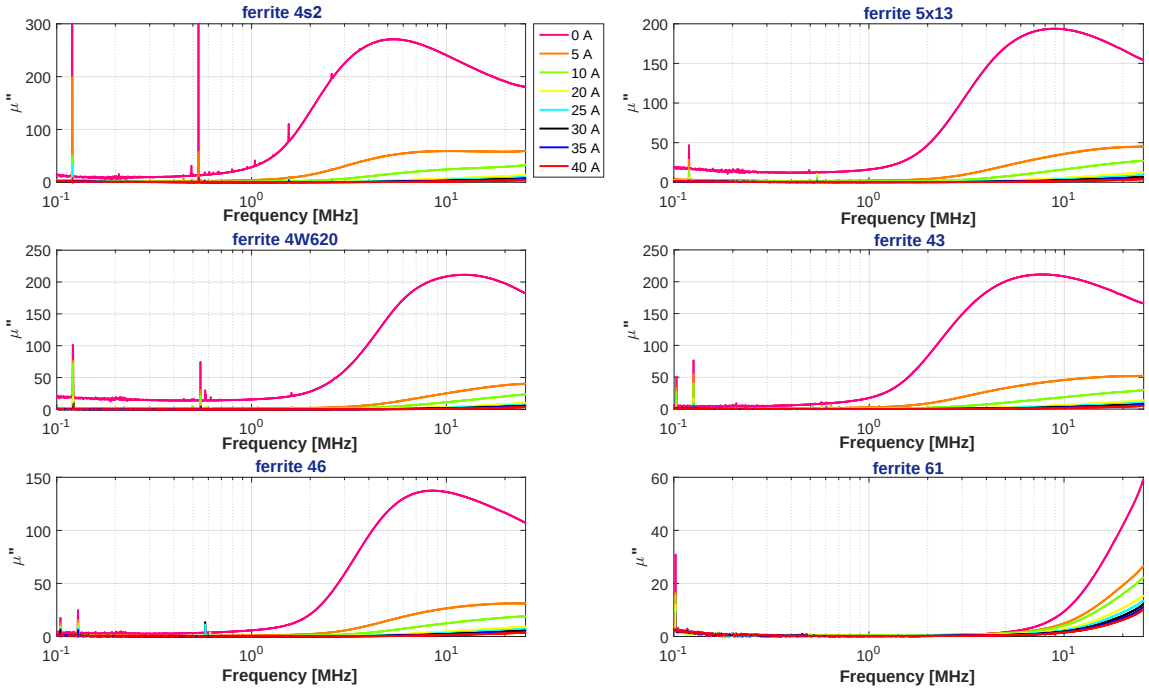

Figure 5.12: μ'' variation of several ferrite samples, due to the application of a parallel bias field.

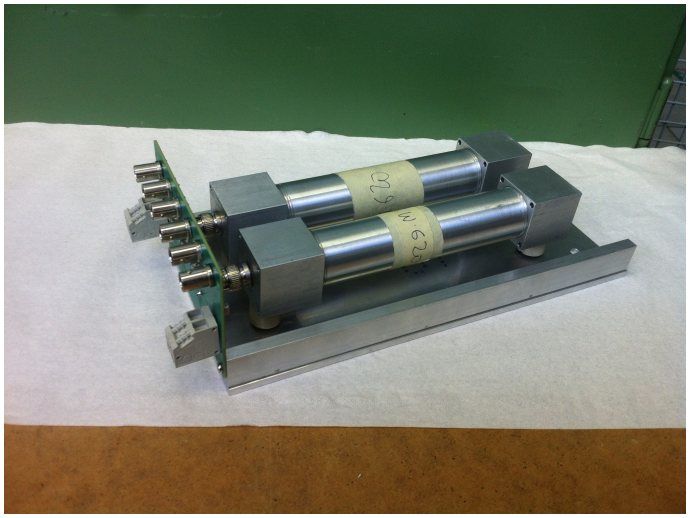

Figure 5.13: Prototype of the grid variable inductance. Two shorted coaxial line are in parallel with respect to the RF path and connected to a PCB. The latter contains the sockets for the bias connections, the capacitors decoupling the DC from the RF paths, and the pins for the connections to other devices.

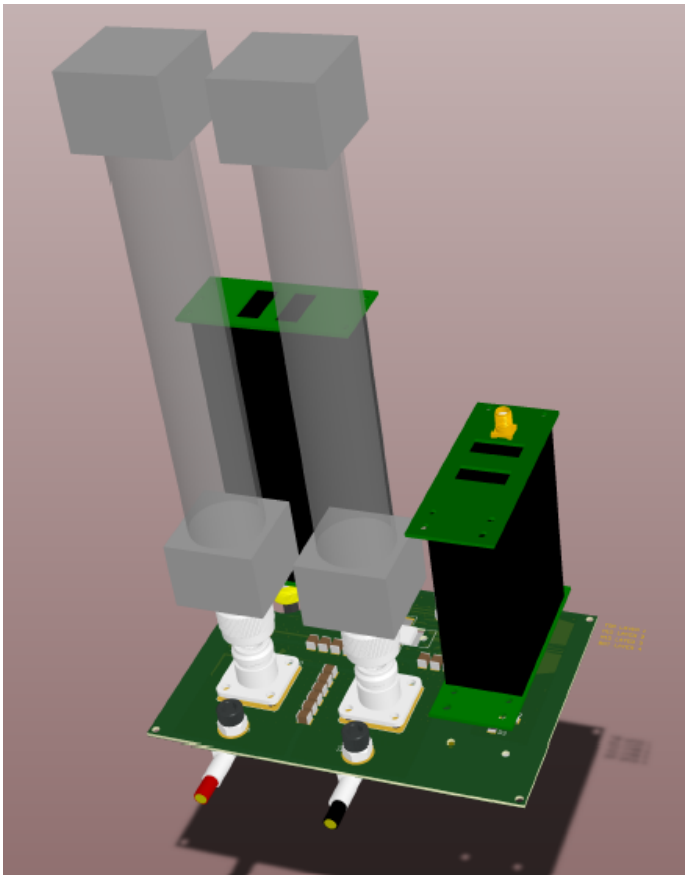

Figure 5.14: Sketch of the three devices forming the Final grid resonator. The drawing shows how they are assembled together and connected to the PCB.

achieve the required tuning specifications, the needed current range was found high (>70 A) and led to an excessive heating of the structure. Therefore, this design was abandoned in favor of a parallel biasing, since the induced change of μ_r for a given value of the current is greater compared to that of a perpendicular bias field.
The process of choosing the suitable ferrite to be installed in the resonator consisted in characterizing several ferrite samples with the aforementioned techniques, searching those featuring the lowest losses in the required frequency range (Table 5.1 and Figs. 5.11 and 5.12).
The variable inductance, in fact, is electrically connected in parallel to the grid transformer: if its losses are considerably high they affect the total Driver load.
The ferrite type 4w620 was chosen as the most suitable ferrite for our purposes, since

Table 5.1: Permeability values of several ferrite material under test. The table contains the μ' evaluated on samples with some magnetic remanence and after a demagnetization process.

Ferrite material	μ' **demagnetized**	μ' **remanence**	μ' **datasheet**
4s2	780	640	850
5x13	520	410	N/A
43	600	500	800
46	450	300	500
61	135	110	125
4w620	540	430	620
c2010	310	280	350
4L2	200	190	200

for parallel bias current of ∼30 A, at 10 MHz, the μ'' was found to be < 2 .
Nevertheless, the ferrite samples selected for the resonator configuration still presented excessive losses at 10 MHz.
In fact, dedicated tests for measuring the losses featured by the variable inductance in the operating frequency range were performed. The device was connected to a 390 pF capacitor, representing the total capacitance in parallel to the variable inductance of the 10 MHz amplifier. While at 3 MHz 1 A DC current was sufficient to tune the resonator, 31 A DC were necessary to reach 10 MHz.
With measured losses of ∼540 Ω at 3 MHz and ∼360 Ω at 10 MHz the Driver load resulted ∼140 Ω at 3 MHz and ∼126 Ω at 10 MHz.
To further reduce the losses of the variable inductance, a superposition of both parallel and orthogonal bias was tried. At an early stage, the sample holder was put into a cylindrical solenoid providing the orthogonal external field (Fig. 5.15).
This method, according to [58] and [60], allows to enlarge the available tuning range reducing garnets losses in the given frequency range.
The results of the tests found an optimum combination of the two bias fields (Tab. 5.2) that reduces the losses amplitude by a factor of 2 for the ferrites under test.
To ease the integration of this resonator in the PS amplifier, reducing its space occupancy, the perpendicular bias was provided by winding the two coaxial lines with a copper wire (Fig. 5.16). The thickness and the number of windings was chosen to

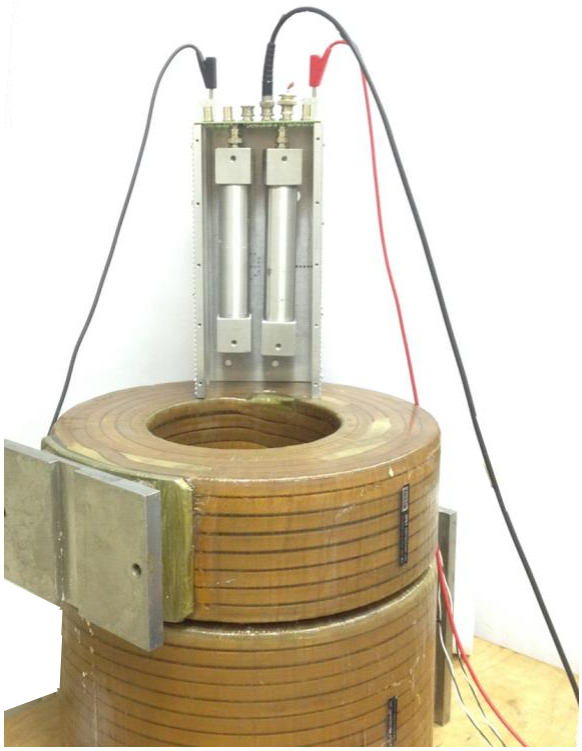

Figure 5.15: Combined bias measurement set-up: an aluminum box holding the resonator put in a big solenoid.

	$\mathbf{I_{BIAS\parallel}}$	$\mathbf{I_{BIAS\perp}}$
3 MHz	1 A	17 A
10 MHz	36 A	43 A

Table 5.2: Values of the combined bias parallel and perpendicular currents needed to tune the resonator at 3 MHz and at 10 MHz.

generate the same field provided by the big solenoid with the same bias current.
It is worth mentioning that, when both orthogonal and parallel bias are used, a bias field lines relative orientation was be found to provide the lowest losses.
Measurements of the impedance of the resonator at 3 and 10 MHz have been performed to evaluate the ferrite losses. Since the variable inductance resonates in parallel with the ∼390 pF capacitance of the amplifier tubes, the total impedance reads:

$$Z_{res} = \frac{1}{\frac{1}{R_p} + j(\omega C_p - \frac{1}{\omega L_p})} \tag{5.32}$$

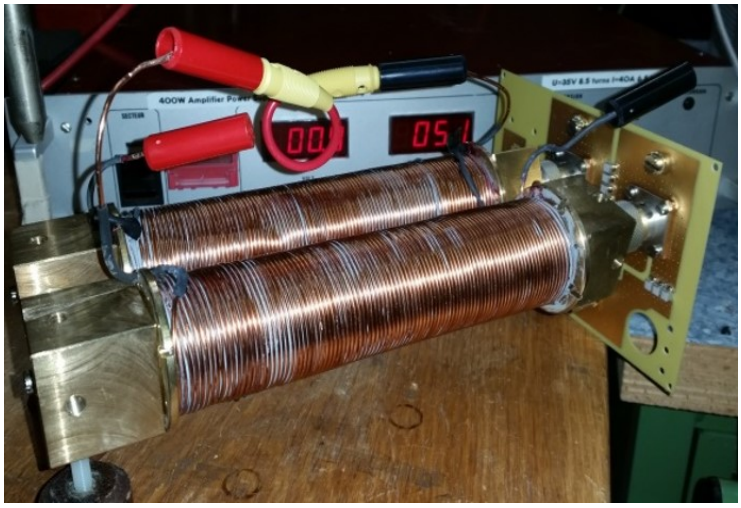

Figure 5.16: Prototype of the grid variable inductance. Two shorted coaxial line are in parallel with respect to the RF path and connected to a PCB. The latter contains the sockets for the Bias connections, the capacitors decoupling the DC from the RF paths, and the pins for the connections to other devices.

therefore the higher is the real part of the impedance, the lower are the ferrite losses.

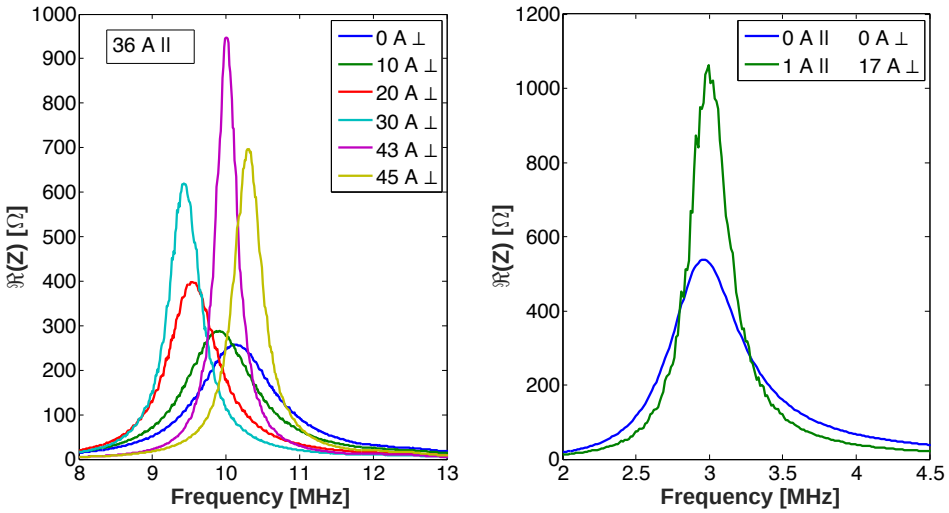

Figure 5.17: Results of the application of combined bias at 10 and 3 MHz. Since the variable inductance resonates in parallel with a capacitor the maximum of the real part of the impedance corresponds to the minimum of ferrite losses.

Figure 5.17 shows that varying the orthogonal bias field at a fixed operating point given by the parallel bias, the resonant frequency changes and the ferrite losses are

reduced: while the orthogonal bias current is increased the resonant frequency first increases and then decreases. At the same time, the ferrite losses gradually decrease, reaching a minimum, and then increase again.
The superposition of perpendicular and parallel magnetic fields, usually used for garnets, was found promising also for our purpose.
Tests of the performance of the new resonator under high field condition were performed, by using the set-up shown in Fig. 4.13. The voltage measured across the resonator, at 3 and 10 MHz, while increasing the input of the resonator by steps of 6 dB, is shown Fig. 5.18. More than 20% additional losses due to the increasing RF

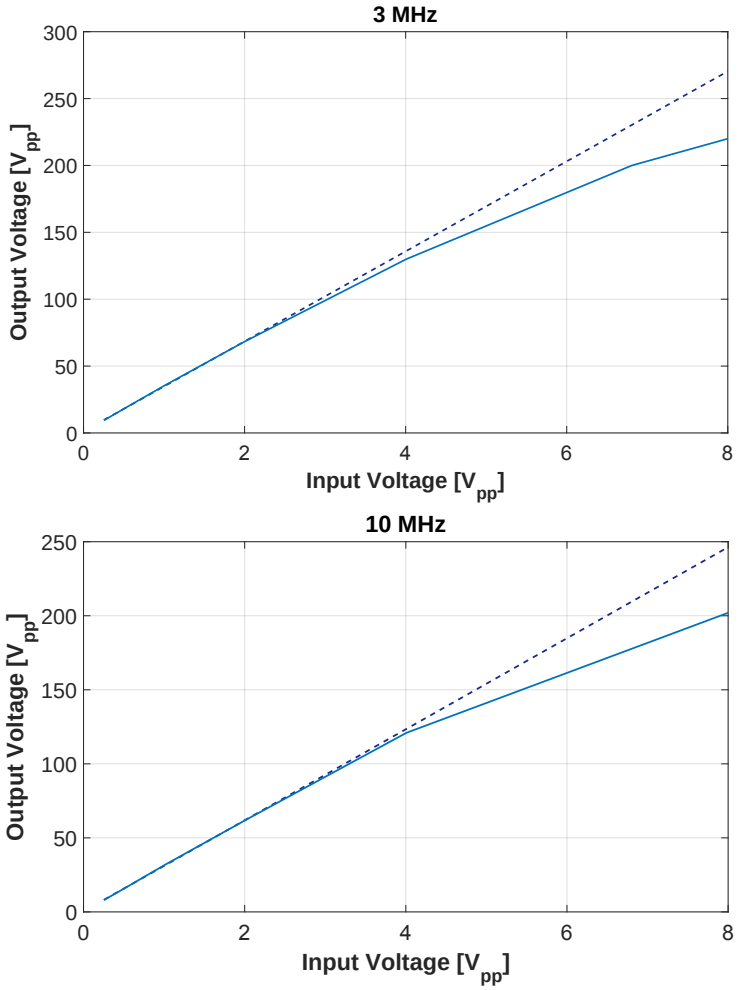

Figure 5.18: Test of the linearity of the grid resonator with an increasing input power.

input were measured. As a consequence, different bias conditions, shown in Tab. 5.3, were required to find the optimum combination of parallel and perpendicular current which could cover the necessary tuning range and, at the same time, reduce the losses as much as possible.

	$\mathbf{I_{BIAS\ \parallel}}$	$\mathbf{I_{BIAS\ \perp}}$
3 MHz	4 A	20 A
10 MHz	42 A	76 A

Table 5.3: Values of the combined bias parallel and perpendicular currents needed to tune the resonator at 3 MHz and at 10 MHz.

Despite the promising performance the device was not considered suitable for being installed in the amplifier chain. The higher current, in fact, would have required the design and the installation of a cooling system to compensate for the high heat dissipation. In addition mechanical changes of the amplifier would have been necessary to install it in the amplifier chain.
For these reasons the work on the device was abandoned in favour of the resonator described in the previous chapter and finally replacing the old one.

Chapter 6

Beam-cavity interaction studies

The eleven accelerating cavities of the PS consist of two ferrite-loaded coaxial $\lambda/4$ resonators each. Both resonators oscillate in phase, as their gaps are electrically connected by short bars. They are, in addition, magnetically coupled via the bias loop used for cavity tuning. The cavities are equipped with a wide-band feedback system, reducing the beam induced voltage, and a further suppression of the beam loading is achieved by two relays which short-circuit each half-cavity gap when the cavity is not in use. Asymmetries of the beam induced voltage in the two half-cavities were observed during Machine Development (MD) studies. They indeed indicated that the coupling between the two resonators is not as tight as expected, and as a consequence the total cavity impedance coupling to the beam may be affected differently by the contributions of both resonators. A dedicated measurement campaign with high-intensity proton beams, in comparison to numerical simulations was carried out to investigate the beam-cavity interaction. This chapter reports the results of the study and the work aiming at the development of a model of the system, including the wide-band feedback, which reproduces the measured beam-cavity interaction and provides a correct evaluation of the beam coupling impedance [61].

6.1 Beam-cavity interaction in the 10 MHz RF system

A beam travelling in a synchrotron loses part of its energy at each turn; part of this energy loss generates an electromagnetic (EM) wake field that acts back on the beam itself. Depending on the beam intensity, this may cause significant modification to the dynamics of the particle motion [18]. A cavity, like any other equipment installed in the beam line, can be modeled as a complex impedance Z. When a beam of current I_b travels across the cavity, a beam induced voltage V_b develops at the cavity gap [62]:

$$V_b = -Z \cdot I_b, \tag{6.1}$$

where the minus sign indicates that the induced voltage leads to an energy loss.
The evaluation of the 10 MHz cavity impedance has to take into account the effect of the electronics of the amplifier driving the cavity, including the action performed by the wide-band feedback.

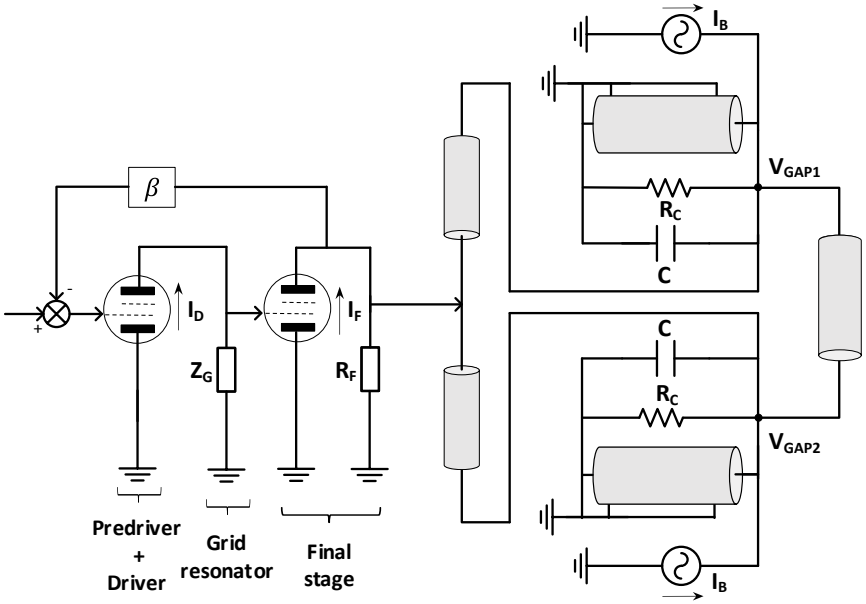

Figure 6.1: Simplified model of the 10 MHz RF system, including two shorted coaxial line resonators and the driving amplifier.

Since the beam crosses both gaps in series, it can be modeled with two current

sources, acting independently on the two cavity gaps. From the equivalent circuit of the amplifier cavity-system, shown in Fig. 6.1, the total impedance seen by the beam can be approximated as:

$$Z(\omega) = 2 \cdot \frac{2 \cdot \frac{R_F \cdot Z_c(\omega)}{2R_F + Z_c(\omega)}}{1 + \beta \cdot Z_G(\omega) \cdot g_D \cdot g_F \cdot \frac{R_F \cdot Z_c(\omega)}{2R_F + Z_c(\omega)}}, \tag{6.2}$$

with $Z_G(\omega)$ being the impedance of the grid resonator loading the Driver stage, g_D and g_F the transconductances of Driver and Final amplifier, R_F the anode resistance of the Final stage, $Z_c(\omega)$ the impedance of a cavity half, β the feedback factor. The factor 2 indicates that beam sees the two gaps in series and excites both simultaneously.

6.1.1 CST simulations

A method for the evaluation of the 10 MHz cavity impedance, described into detail in [63] and [64], was already developed and used for the studies of coupled-bunch instabilities. It was based on a different model of the beam-cavity interaction: the total cavity impedance was evaluated from the transfer function measured on a gap, considering the beam as one current source only. This led to an underestimation of the effective cavity impedance by a factor 4.
The model of the beam-cavity interaction and the consequent evaluation of the system impedance introduced in the previous section will be largely used in this chapter, replacing the existing one and leading to the development of a consistent numerical model of the 10 MHz system impedance. In order to validate our model through an electro-magnetic characterization of the system, we have developed a CST [65] model of the cavity, which could benchmark our assumptions, by analysing the effect induced by a bunch circulating in the cavity.
The ferrite properties and their variation in the frequency range, measured as described in Chap. 5, can be included in the model of the cavity. The dispersive parameters of the 4L2 material, used for the cavity ferrite disks, have been defined in CST, importing μ' and μ'' measured data.
Frequency and time domain simulations can be performed. In time domain simula-

tions, CST offers the possibility to define and automatically fit a specific magnetic material dispersion curve from imported data, by using a general N-th order polynomial. As for the frequency domain case, the program can either directly implement the imported material data or use the dispersive model fit. The relative dielectric permittivity of 4L2 ferrite was set to $\epsilon_r = 10$, according to the technical specifications [66] of the ferrite rings used as core of the 10 MHz cavities. A comparison between the measured and fitted μ' and μ'' parameters is shown in Fig. 6.3.

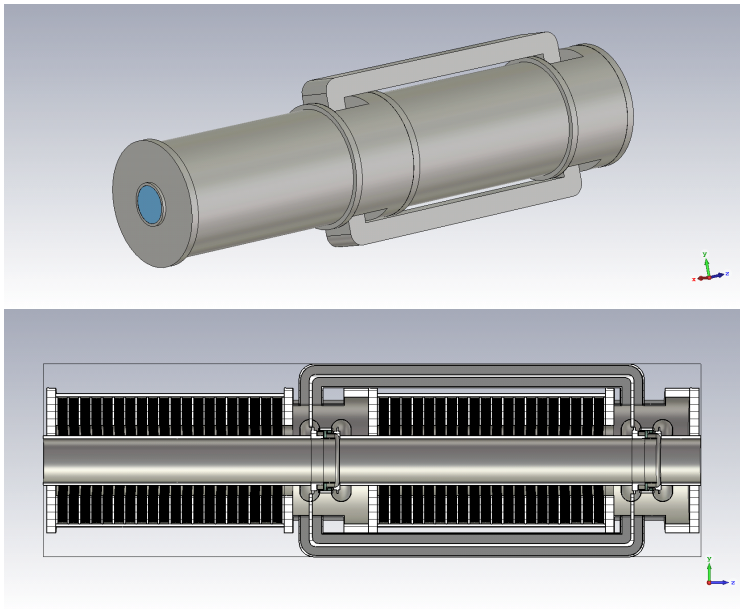

Figure 6.2: CST model of the PS 10 MHz cavity.

The model was developed from cavity drawings and includes the two variable capacitors mounted in parallel to the gaps, which fix the resonant frequency of the bare resonators. Figure 6.4 shows the gap design in detail. The green piece represents the ceramic gap, across which the electric field is generated. The gap is connected via the flanges to the vacuum chamber of the cavity. The two electrodes with a potential of 10 kV_p protect the ceramic from ions, which could otherwise generate breakdowns. Behind the gap the variable capacitor is modeled as a disc capacitor, whose surface and dielectric properties are chosen to let the structure resonate at ~2.6 MHz, which is the measured resonance of the cavity in the absence of tuning current.
In order to demonstrate the correct impedance evaluation and verify how the coupling between the gaps and the cavity geometry contribute to the effective impedance, we

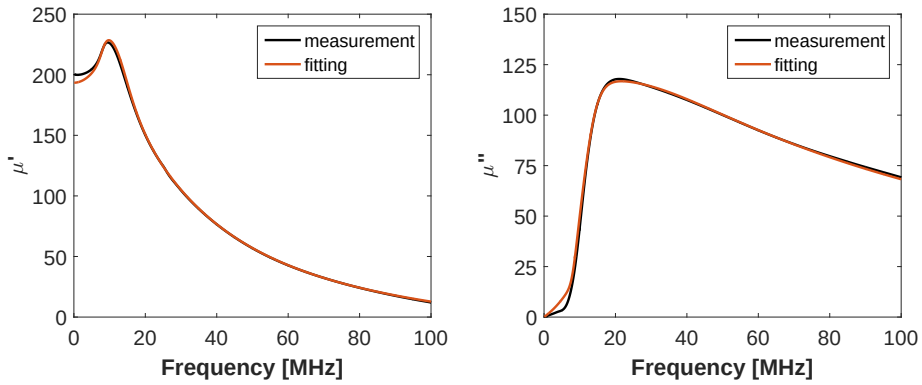

Figure 6.3: Dispersive parameters of 4L2 ferrite measured and fitted by CST.

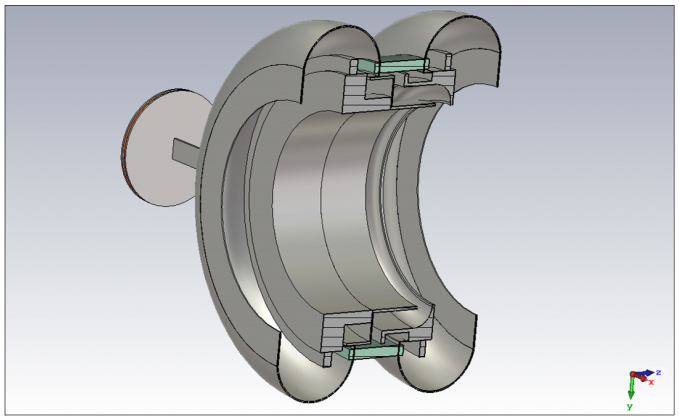

Figure 6.4: Detailed view of the CST model of the 10 MHz cavity gap.

started our analysis from a simplified geometry, studying only a single cell cavity, shown in Fig. 6.5.

For each CST Microwave Studio (MWS) structure two fundamentally different views of the model exist: the standard and the schematic views. The standard view is the 3D model representation which is visible by default. In addition, the schematic view can be activated, where lumped elements can be connected to the 3D model. In this schematic, the cavity is represented as a *CST MWS block*. To validate our argumentation the results coming from two CST simulation tasks are compared:

- AC simulations, available from the schematic view. They provide voltage and current as a function of the frequency inside the specified range for all external ports. In fact, in order to validate our model, a coaxial waveguide port has

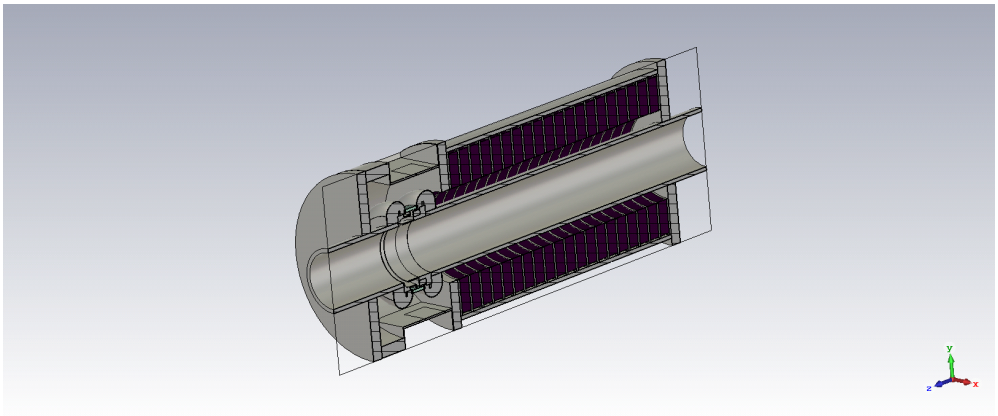

Figure 6.5: Single cell model of the 10 MHz cavity.

been added to the tank covering the gap, and used as a port to drive the gap by means of a current source (Fig. 6.6). A short bar is connected to the gap electrode and represents the inner conductor of the coaxial port.
The resulting voltage evaluated at the port is equivalent to the cavity gap impedance, being the current amplitude 1 A.

- Wakefield simulations, used to evaluate the wake potential generated by a Gaussian bunch circulating inside the cavity model. The beam coupling impedance is then evaluated as the Fourier transform of the wake potential.

For the wakefield simulations, the bunch length, defined in terms of σ_b (standard deviation of the Gaussian shaped bunch) and the length of the wake have been chosen to obtain a good resolution in the frequency domain. Furthermore for this analysis the dispersion properties have been simplified: the same μ' has been kept, while higher μ'' has been used in order to reduce the equivalent impedance of the cavity, and thus obtain a good resolution with lower wake length. A bunch length of 550 cm was assumed. The wake potential has been evaluated through the Indirect Test Beam integration method. The indirect method computes the longitudinal wakes generated by the interaction of test beams with the wall of the beam pipe structure to get the longitudinal wake everywhere in the cross section of the cavity and it is considered the most accurate calculation method presently available [67]. All the surface boundaries have been defined as Perfect Electric Conductor (PEC) on the whole surface, excepted for the beam entrance and exit planes that have been defined as free space at the

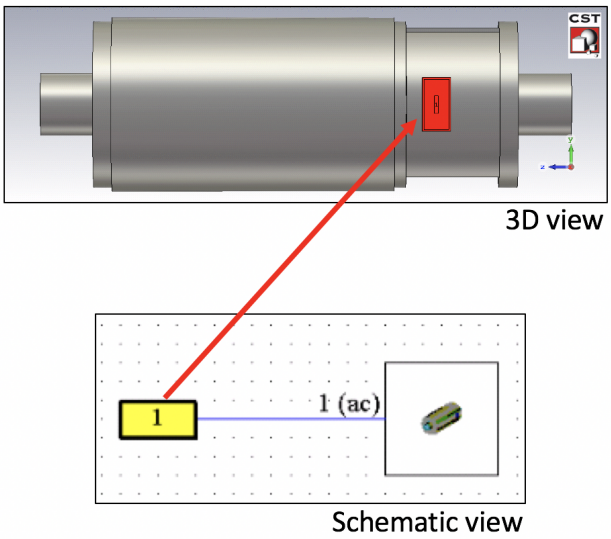

Figure 6.6: Schematic and 3D views of the AC simulation set-up of a single cell model of the 10 MHz cavity.

beam pipe aperture.
The results of the AC and wakefield simulation of a single cell structure are compared in Fig. 6.7, showing a good agreement. This confirms that both models and simulation tools can reproduce the beam cavity interaction properly.

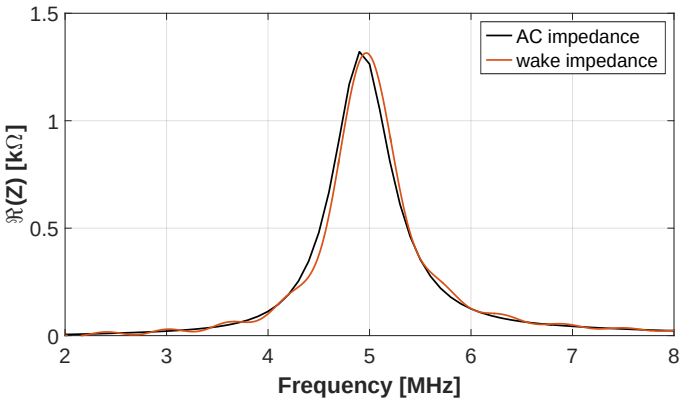

Figure 6.7: Impedance resulted from CST wake field simulations and AC simulations of a single cell 10 MHz cavity.

The analysis continued afterwards, with a slightly more developed structure, modeling a cavity consisting of two identical half resonators. In an early stage, the bar coupling

the two cavity halves is not included in the model (Fig. 6.8).

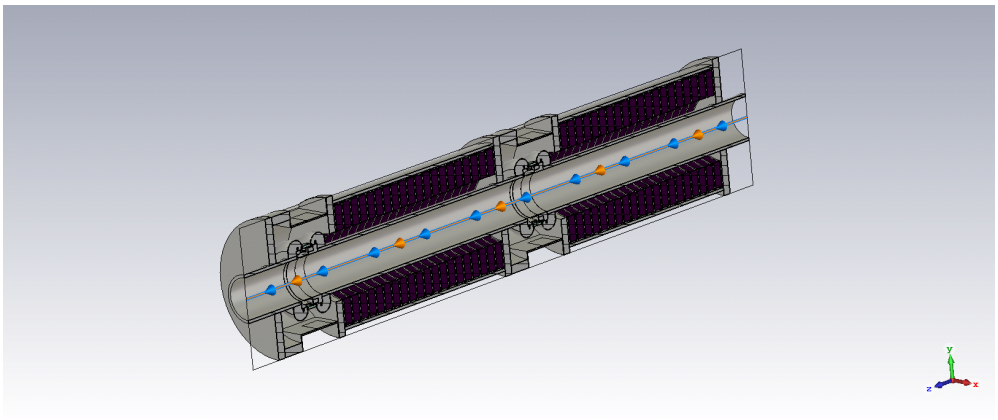

Figure 6.8: CST model of the 10 MHz cavity with uncoupled gaps.

Simulations have been performed defining again a beam source for the wakefield calculation and a current source on each gap for AC simulations. The two resonators are independent from the current source point of view, thus the measured AC impedance is equivalent to the single cell case. The total impedance can be approximated as twice the single gap impedance and this is confirmed by the wakefield simulation results (Fig. 6.9). The latter, in fact, show a factor 2 of difference, which is due the beam crossing the gaps in series.

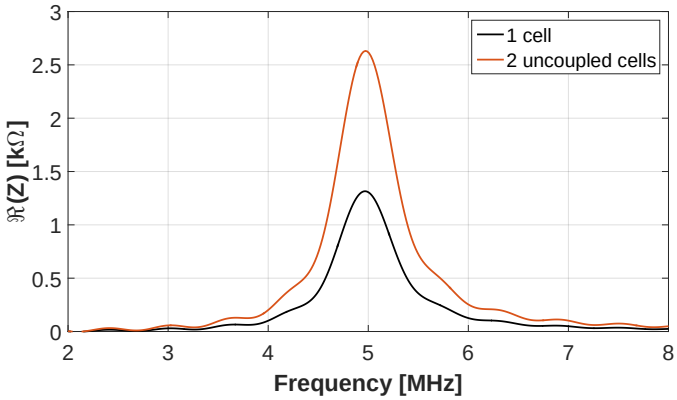

Figure 6.9: Impedance resulted from CST wake field simulations of a single cell and double cell structure with uncoupled gaps.

To simulate the effective 10 MHz cavity geometry, another simulation taking into

account the presence of the bar coupling the gaps was carried out. The simulation results, shown in Fig. 6.10 are equivalent to the previous case.

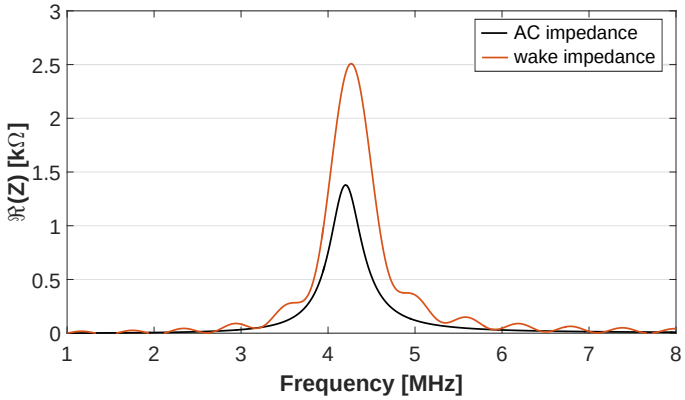

Figure 6.10: Impedance resulted from CST wake field simulations and AC simulations of the 10 MHz cavity with coupled gaps.

For sake of completeness, the coupling line has been modeled as a transmission line in the schematic view of CST and connected to the gaps via two coaxial ports, which are placed on the cavity tank and connected to the gaps. Wakefield simulations have been performed by varying the delay of the line. The results, as expected, show no influence of the coupling line delay in the evaluation of the wake impedance. When the gaps are coupled, in fact, the two cavity halves are equivalent, thus the same voltage is induced on both gaps and no beam induced current flows through the connecting bars, making the role of the coupling bar geometry irrelevant.
In conclusion, in the wake impedance computation, based on the integration of the induced field along the whole structure, the bunch travelling along the structure excites simultaneously two equivalent coupled gaps, resulting in twice the wake field acting on a test charge. The assumption of using two current sources to excite the cavity is therefore justified.

6.1.2 Beam induced voltage measurements

To evaluate the effective impedance as seen by the beam, a measurement campaign was carried out. The beam current can be measured via a beam current transformer.

The measured signal $I_{meas}(t)$ is proportional to the instantaneous beam current $I_b(t)$ and must be scaled by the attenuation of the transformer and of the cables.
The attenuation constant k can be computed from the total bunch charge, given by the charge of a proton e_0 multiplied by the number of protons per bunch N_p, which is constant and known: $Q = e_0 \cdot N_p = 1.6 \cdot 10^{-19} \cdot 8 \cdot 10^{12} \approx 1.3 \cdot 10^{-6}[C]$.
The total charge of the bunch is equal to the integral of the beam current along the bunch length:

$$Q = \int I_b(t) \cdot \mathrm{d}t = k \cdot \int I_{meas}(t) \cdot \mathrm{d}t \; [C] \tag{6.3}$$

Similarly, the induced voltage on the gaps is measured via a probe characterized also by its own attenuation. The latter is computed by measuring the gap voltage along the cycle when the cavity is pulsed at full voltage in absence of beam. The attenuation factor is calculated as the ratio between the measured value and the programmed value on the gap. The programmed voltage of a 10 MHz cavity reaches $\sim$20 $\mathrm{kV_p}$ (10 $\mathrm{kV_p}$ per gap) at flat top, as shown in Fig. 6.11 (black trace).

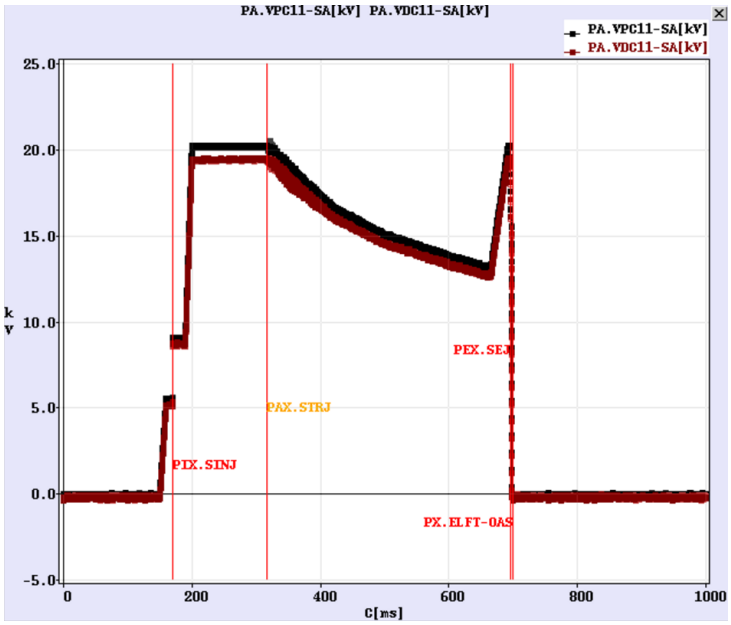

Figure 6.11: Total programmed (black trace) and detected (red trace) voltage of the cavity in the PS straight section 11, during an n-ToF cycle, at $h = 8$ ($\sim$3.5 MHz).

The cavity impedance has been extracted from the measurements of the voltage induced on the 10 MHz cavities by a high-intensity single bunch circulating in the

machine, usually sent to the n-ToF experiment, with $\sim 8 \cdot 10^{12}$ protons, at fixed harmonic.

The cavities under test are presently operated by a standard amplifier. The tests have been performed when the cavities are only driven by the beam and the drive power of the amplifier is zero. The gap voltage and the beam current have been measured via an oscilloscope at three stages of the beam cycle: injection, transition and ejection (Fig. 6.12).

The bunch length and thus the beam spectrum significantly change during the cycle and, consequently, the measured beam induced voltage also varies. The highest attention is put on the effects observed during transition, as the bunch presents the shortest length, thus the highest harmonic content, throughout the acceleration cycle.

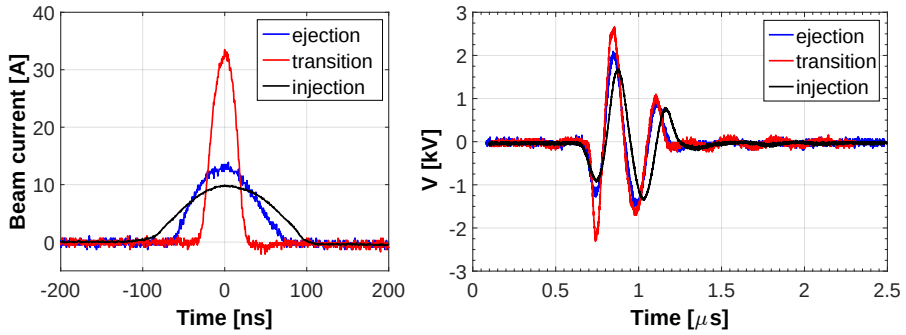

Figure 6.12: Measurements of the bunch current and of the induced voltage across a cavity gap, at h=8, at injection, close to transition crossing and close to ejection.

From these measurements the contribution of the beam harmonic content to the cavity gap impedance is therefore evaluated, according to the equation [18]:

$$\Re\left(Z(\omega)\right) = -\Re\left(\frac{V(\omega)}{I(\omega)}\right) = -\Re\left(\frac{FFT\left(V_{gap}(t)\right)}{FFT\left(I_{bunch}(t)\right)}\right) \tag{6.4}$$

where V_{gap} is the voltage induced on one gap and I_{bunch} is the beam current. We can either measure the voltage on the right or on the left gap, as they are geometrically equivalent and electrically connected. The total cavity impedance can be approximated as twice the impedance evaluated across a gap. The accuracy of Eq. 6.4 is higher, the wider the spectrum is of the beam harmonics.

Figure 6.13 shows the results of the calculation of the gap impedance of three cavities as observed from beam induced voltage, after transition crossing.

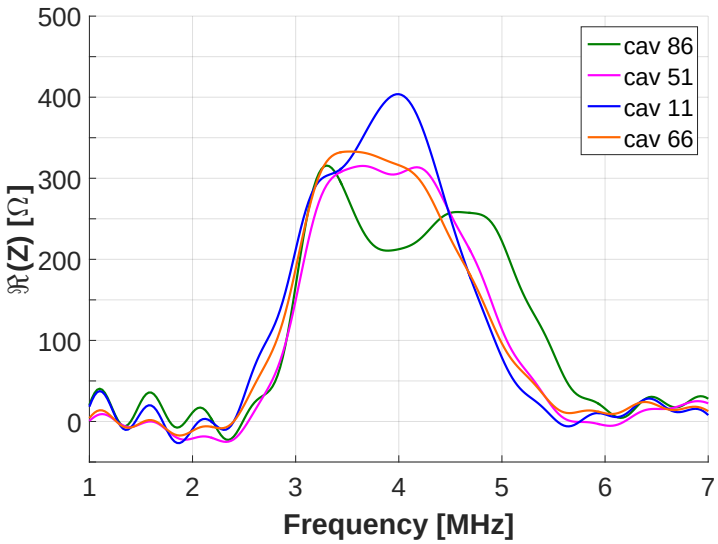

Figure 6.13: Measured gap impedance of cavities in straight sections 11, 51, 66, 86 at h=8 close to transition crossing.

Since the measurements are performed with a zero voltage program, the cavity fine tuning system cannot be active. This can lead to some distortions in the shape of the impedance, as observed in the measurements of cavity 11, since the local grid resonator and the cavity are not aligned to the same frequency to produce the correct phase of the feedback signal at the cavity resonance.
If the feedback attenuation is too small and the stability margins are low, the shape of the impedance around the main harmonic is not flat: the impedance is lower at the main harmonic, but increases towards the side lobes, as observed in cavity 86 measurements.

6.1.3 PSPICE simulations

In order to identify the main contributors to the total cavity impedance and to benchmark the measurement method, PSPICE simulations and additional measurements have been carried out in parallel and compared.
The PSPICE model, which was already able to reproduce the system behavior, has been significantly optimized for this study, increasing its accuracy. In the model, the beam, which crosses the two gaps in series, is represented by two current sources

delayed in time by 4 ns, which corresponds to the time of flight between the two gaps. As described in Chap. 3, it is worth recalling that the cavities are split in four tuning groups to allow beam manipulations. In our case of study, for calculating the beam coupling impedance, a high-intensity single-bunch beam (n-ToF) was chosen, to avoid multi-bunch interaction effects on the impedance. The programmed RF voltage (max voltage ∼200 kVp) is calculated for the required energy increase; the desired beam energy can therefore be achieved if each of the ten PS cavities provides 10 kV_p per gap (i.e. 20 kV_p per cavity) and they are tuned at h=8. Measurements at harmonics higher than h=8 cannot be performed on all the cavities, because it would force the cavities belonging to the same group to be tuned at a different frequency with respect to the accelerating harmonic, leaving insufficient RF voltage for acceleration at h=8. Therefore, in order get a full understanding of the beam-cavity interaction and its variations in the operating frequency range, we focused our attention on cavity 11, which has its own tuning power supply.
Figures 6.14 and 6.15 show that the measured and simulated transfer function of amplifier-cavity 11 system, at 3 and 10 MHz are in good agreement.

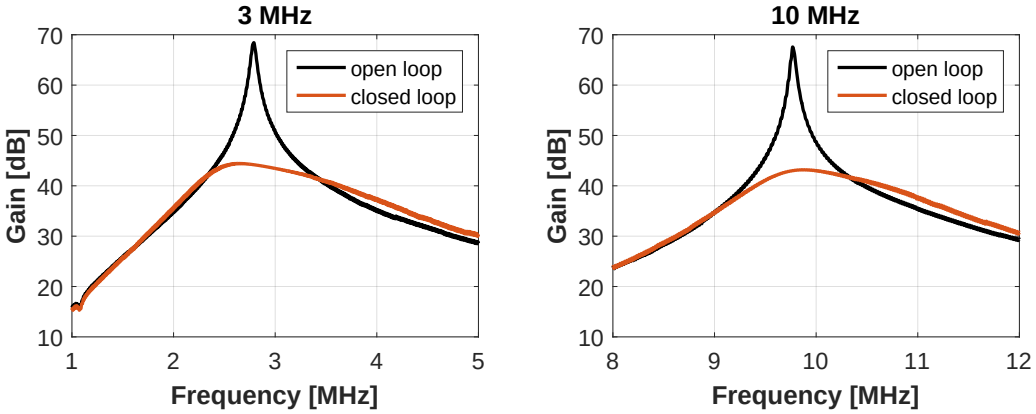

Figure 6.14: Measured transfer function of cavity 11 at 3 MHz and 10 MHz.

Once the behaviour of the cavity under test was well modeled and reproduced, time domain simulations of the beam induced voltage at the different stages of the cycle and at different harmonics were carried out. Figures 6.16, 6.17, 6.18, show the very good agreement that was obtained at the three harmonics 8,16 and 21.
Using Eq. 6.4, the impedance of cavity 11 can be computed from measurements and simulations of the beam induced voltage. The impedance has been evaluated close to

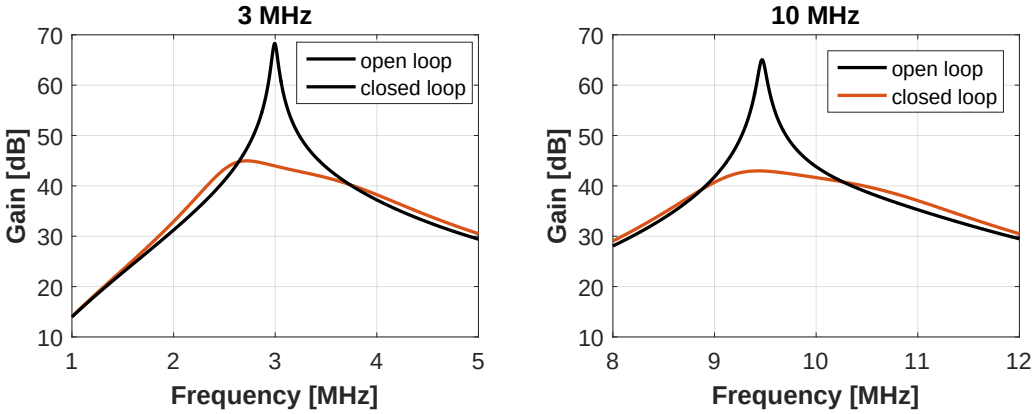

Figure 6.15: Simulated transfer function of cavity 11 at 3 MHz and 10 MHz.

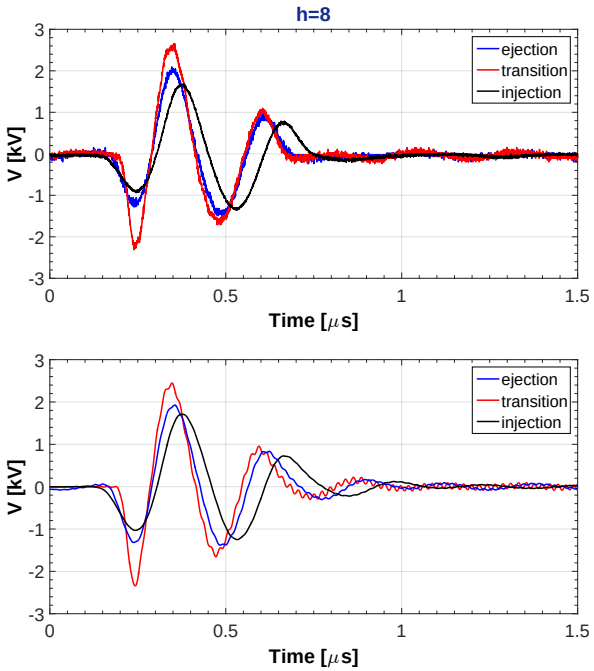

Figure 6.16: Measurements (top) and simulations (bottom) at h=8 of the induced voltage across one gap at injection, close to transition crossing and close to ejection.

transition crossing at different harmonics and then compared with simulation results obtained from time domain simulations, in Fig. 6.19.

While the frequency domain solver performs a small-signal linearization [68], the time domain analysis allows to account for the tubes non-linearities in its results. As illustrated in Fig. 6.20, a small resonance was measured at ∼7 MHz. However, only

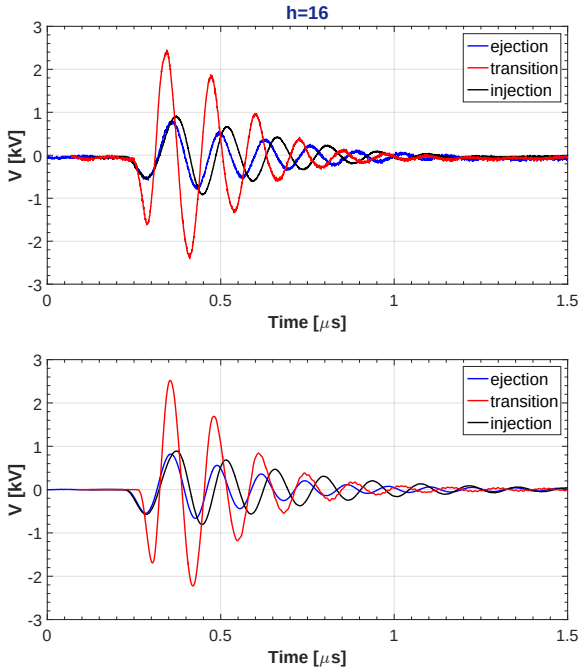

Figure 6.17: Measurements (top) and simulations (bottom) at h=16 of the induced voltage across one gap at injection, close to transition crossing and close to ejection.

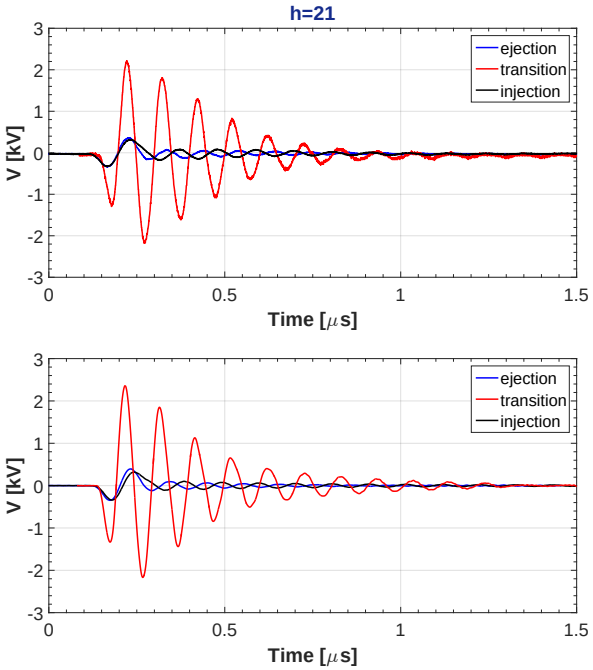

Figure 6.18: Measurements (top) and simulations (bottom) at h=21 of the induced voltage across one gap at injection, close to transition crossing and close to ejection.

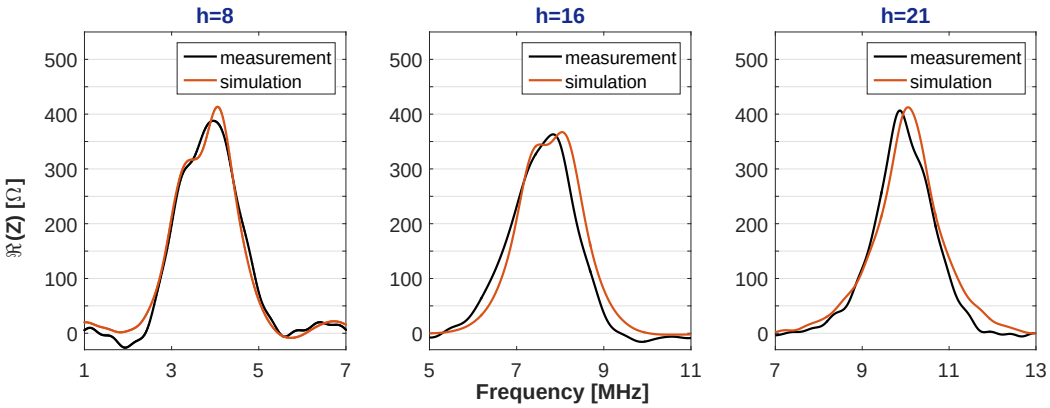

Figure 6.19: Gap impedance of cavity 11 at h=8, 16, 21 measured and simulated for the conditions close to transition crossing.

time-domain analysis of the system allowed reproducing these observation, since it is caused by the higher harmonics generated by the non-linearities of the electron tubes.

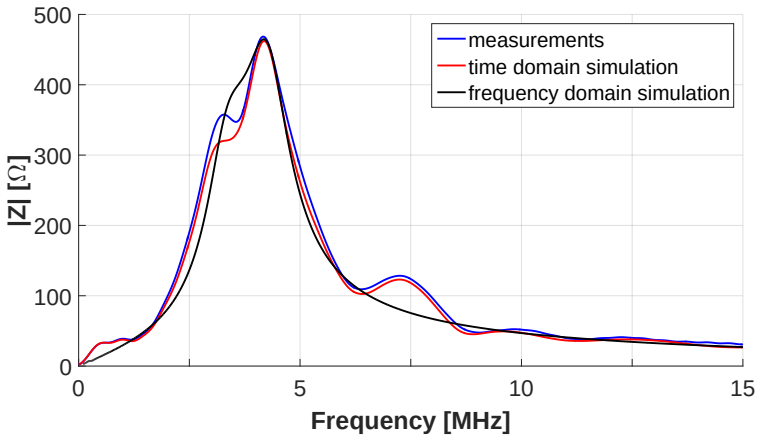

Figure 6.20: Comparison between measurements, time domain simulations, and frequency domain simulations of the gap impedance of cavity 11.

6.1.4 Combined PSPICE-CST simulations

With the purpose of taking advantage of the effectiveness of PSPICE in describing the amplifier chain behavior and the accuracy of CST in modeling the cavity resonator, we have decided to combine the two descriptions into an innovative model that could

run in the CST environment.
As already mentioned CST provides two fundamental views, the 3D and the schematic one. In the schematic view of CST the cavity is already represented as a *CST MWS block*. In addition a *SPICE block* can be included and imports a circuit from a file, allowing the user to choose between SPICE dialects (i.e. SPICE3f4, PSPICE, etc..). The PSPICE netlist of the amplifier model, which is proven to well reproduce the behavior of the real one, has been included in a block and connected to the cavity via a coaxial waveguide port on the bottom bar of the cavity model. The schematic view of the full amplifier-cavity model developed in CST is shown in Fig. 6.21.

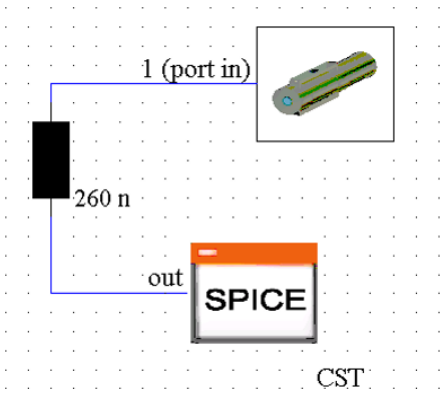

Figure 6.21: CST schematic view. The SPICE block contains the netlist generated by the electrical model of the feedback amplifier. The 260 nH is the inductance modeling the line connecting the amplifier to the cavity. The cavity is represented as a CST MWS block.

In order to validate the model the simulated transfer function of the system has been evaluated, by using a S-parameter simulation task.
The simulations performed with CST MWS, compared with measurements in Fig. 6.22 show a good agreement.
Once the validation of the model completed, the impedance of the cavity has been evaluated using the AC simulation task. A waveguide port has been connected to each gap, and used to feed the cavity via a AC current excitation of 1 A amplitude, as illustrated in the set-up in Fig. 6.23.
In addition, a transient EM/circuit co-simulation task has been performed to evaluate the wake potential generated by a Gaussian bunch circulating inside the cavity. To compare the simulation results with measurements performed at h=8, the ferrite

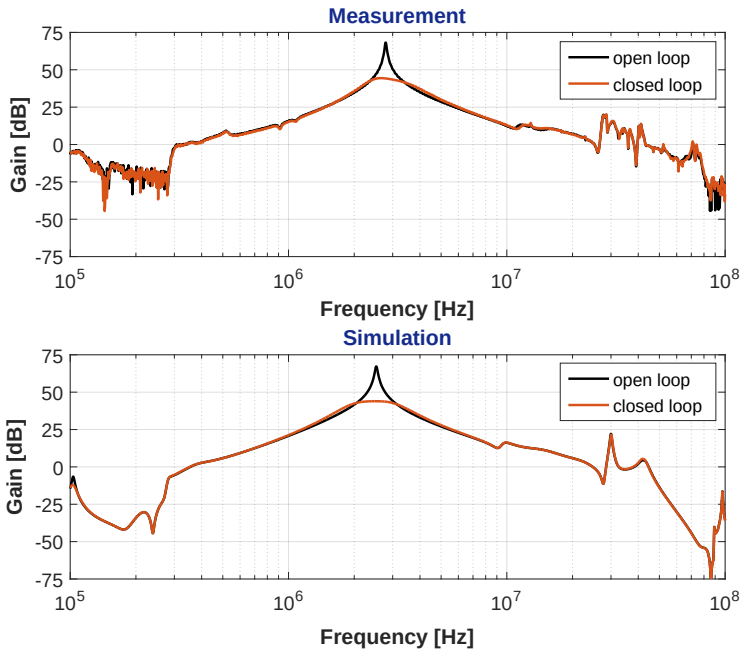

Figure 6.22: Transfer function of the cavity-amplifier system measured (top, resonant frequency $\approx 3\,\mathrm{MHz}$) and simulated (bottom, resonant frequency $\approx 2.6\,\mathrm{MHz}$).

dispersive properties have been scaled to make the structure resonating at $\sim$4 MHz, according to:

$$\frac{f_{(4\,\mathrm{MHz})}}{f_{(2.6\,\mathrm{MHz})}} = \frac{1/\sqrt{C \cdot L_{(4\,\mathrm{MHz})}}}{1/\sqrt{C \cdot L_{(2.6\,\mathrm{MHz})}}} \approx \frac{\sqrt{\mu_{(2.6\,\mathrm{MHz})}}}{\sqrt{\mu_{(4\,\mathrm{MHz})}}} \tag{6.5}$$

For the wakefield simulations, the same setting used for the analysis described in the previous section have been kept.

The results of both simulation tasks are presented in Fig. 6.24 and compared with the measurements. The value of the impedance evaluated by modeling the beam as two current sources (AC simulation) are in good agreement with the measurements. The difference of bandwidth comes from to the discrepancies between the real ferrite losses and the ones computed by approximation, using the Eq. 6.5. As expected, the coupling impedance resulting from wake simulations, is twice the impedance evaluated from the measurements and AC simulations.

By combing the lumped element model of the amplifier, which takes into account the amplifier non-linearities, and the 3D electromagnetic model of the cavity, including

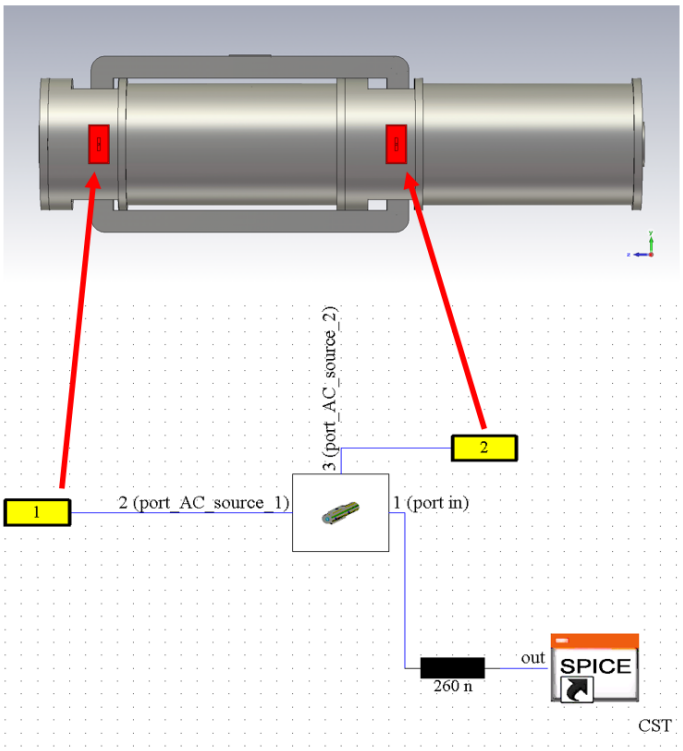

Figure 6.23: Schematic of the combined PSPICE-CST model set-up, used for the evaluation of the cavity impedance. Port 1 and 2 are used to excite and to detect the voltage on both gaps.

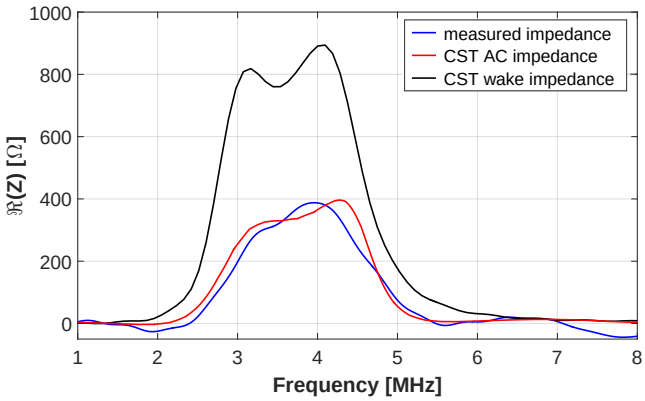

Figure 6.24: Comparison between the measured impedance and the one evaluated from CST simulations.

ferrite dispersive properties, it is therefore possible to understand how the beam actually interacts with the cavity including the whole electronics (amplifier and feedback loops). In addition, the results of simulations confirm the validity of approximation used to evaluate the system impedance from the beam induced voltage measurements, according to Eq. 6.4.

6.2 Gap relays

When the cavities are not in use, two gap relays (one for each cavity half) short-circuit the gaps to strongly reduce the impedance and, as a consequence, the voltage induced by the beam. The gap relay and its position in the cavity gaps are shown in Fig. 6.25.

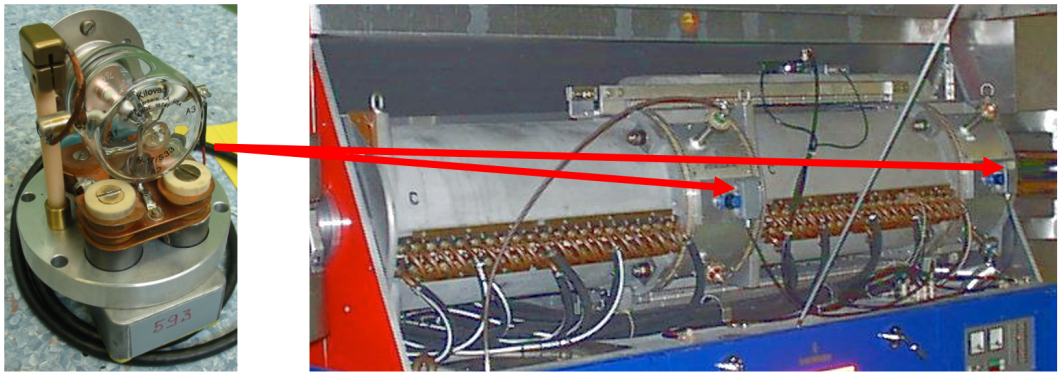

Figure 6.25: Gap relay.

Figure 6.26 shows the impedance measured across the two gaps of cavity 11, when both gaps are open and when they are short-circuited by relays. When the gap relays are in use, in addition to a reduction of the impedance by more than a factor of 4, a shift of the cavity resonant frequency to frequencies higher than the 3-10 MHz operative range, is visible.
Originally, both gaps were equipped with gap relays, but in 1991 the second relay was removed to reduce maintenance costs. Considering that the two half cavities are strongly coupled, we would expect to observe almost equal beam induced voltage at both gaps. However an asymmetric behavior was observed [64] and the cavities have been re-equipped with a second gap relay. The distribution of the beam induced

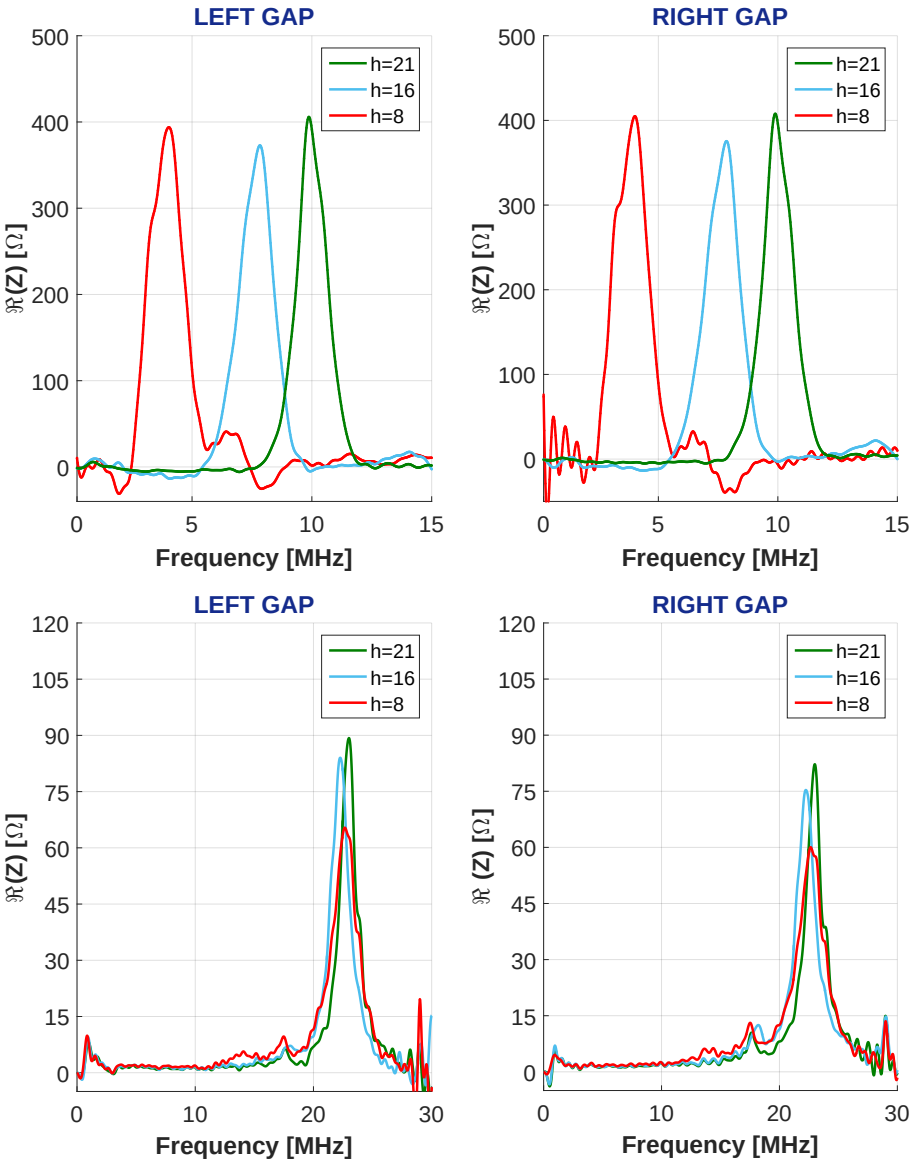

Figure 6.26: Impedance measured across the right and the left gap of cavity 11, when both gaps are left open (top) and when they are shorted (bottom).

voltage in both resonators has therefore been analyzed in more details: measurements and simulations were carried out in parallel to investigate the main causes of the observed asymmetry. The beam induced voltage along the acceleration cycle, measured across the left and right gaps, when only one or both relays are closed, is shown in Fig. 6.27.

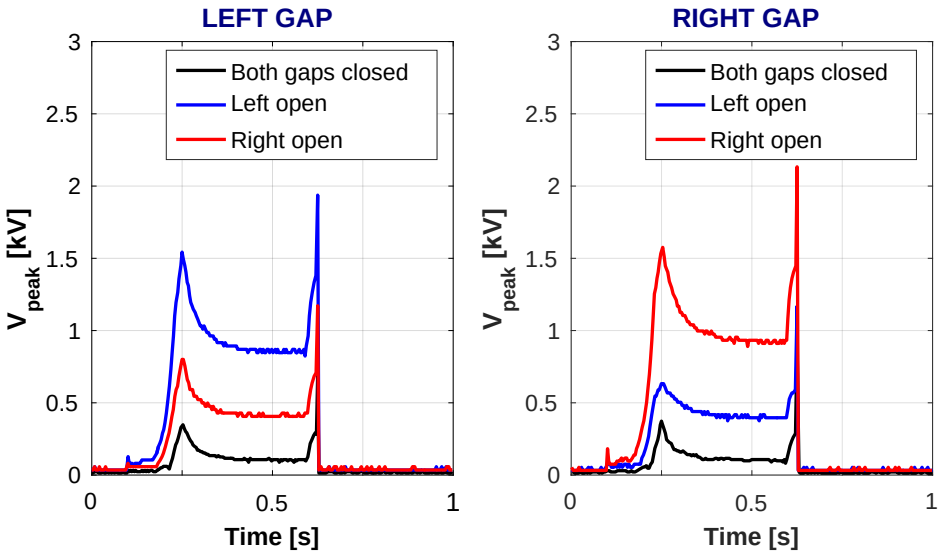

Figure 6.27: Beam induced voltage on left and right accelerating gaps of cavity 11 during the acceleration of a single high intensity bunch. The first peak is at transition crossing and the second comes from bunch rotation before extraction.

The induced voltage is higher in the gap not shorted by the relay: a reduction of the voltage by more than a factor of 2, due to the second gap relay is observed. Moreover the voltage measured at the shorted gap is about half of the voltage at the open gap. It is worth noting that the same asymmetry of the beam induced voltage distribution is present for all cavities and at different harmonics. The gap relay effect on the gap voltage and the voltage distribution has been analyzed through numerical simulations.

A gap relay can be modeled as a series $R-L-C$ circuit, where L represents the leakage inductance due to the connection of the device to the gap, C is the capacitor decoupling the DC voltage, and R is a damping resistor which reduces the cavity impedance over the whole operating frequency range. In order to simulate the gap relay effect on the cavity, a series $R-L-C$ (R=2 Ω, L=150 nH, C=67.2 nF) circuit has been included in the PSPICE model, in parallel to each gap. The device increases the resonant frequency of the cavity, due to the inductance L added in parallel to the cavity, and reduces the real part of the cavity impedance because of the damping resistor.

Figure 6.28 shows a comparison between measurements and simulations when only

the left gap is shorted, when the cavity is tuned to h=8.

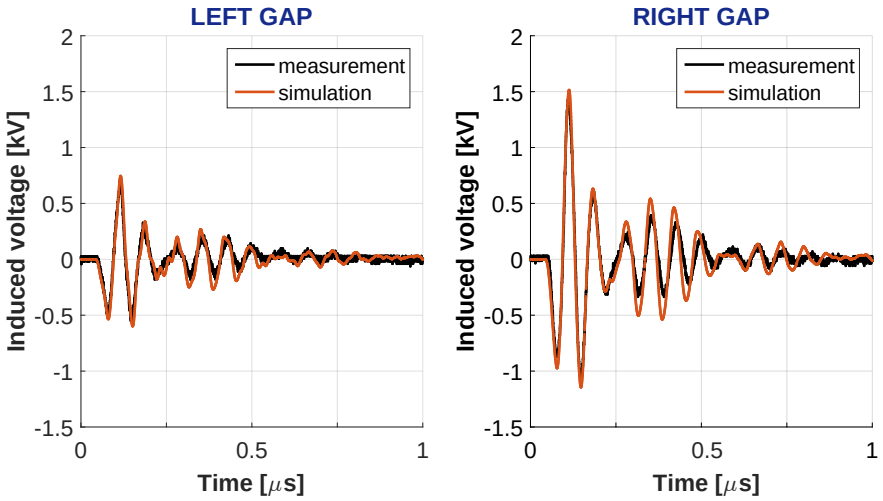

Figure 6.28: Beam induced voltage across the two gaps of cavity 11 tuned to h=8, when only the left gap is shorted.

An oscillation at ∼15 MHz is visible, as well as a modulation of the voltage due to a beat between two frequencies. According to both measurements and CST simulations, the cavity transfer function is characterized by its main resonant frequency and by additional parallel and series resonances due to the cavity geometry and ferrite properties. If the parallel resonant frequency of the cavity tuned to h=8, but shorted by the relay, is close to one of the cavity series resonances, an additional reduction of the induced voltage and thus of the impedance seen by the beam is observed.
In fact, as figure 6.29 shows the measured gap impedance of the cavity, when only one gap relay is in use (the right gap open, left gap shorted), when the cavity works at h=8, 16 and 21. At h=8 the impedance is significantly reduced, if compared with the impedance measured at h=16 and 21.
The beam-cavity interaction, when gap relays are in use, has been also analyzed through CST simulations. The gap relay is modeled as an R-L-C circuit in the schematic view of CST and connected to the MWS block of one cavity gap via a waveguide port connected to the gap.
AC simulations were carried out and as see in Fig. 6.30 the results reproduce the observed asymmetry in the distributions of the induced voltage between the gaps and a qualitative agreement is found with the measurements presented in Fig. 6.29.

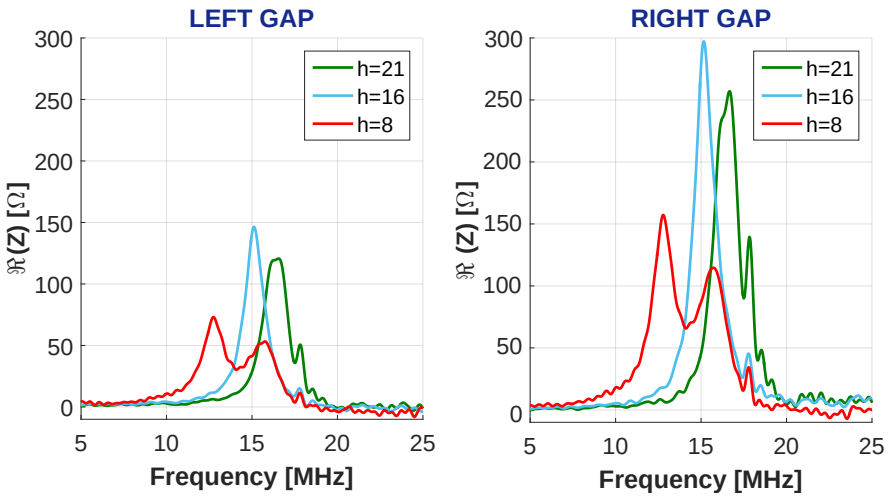

Figure 6.29: Measured gap impedance of cavity 11 tuned to h=8, 16, 21 when the left gap is shorted.

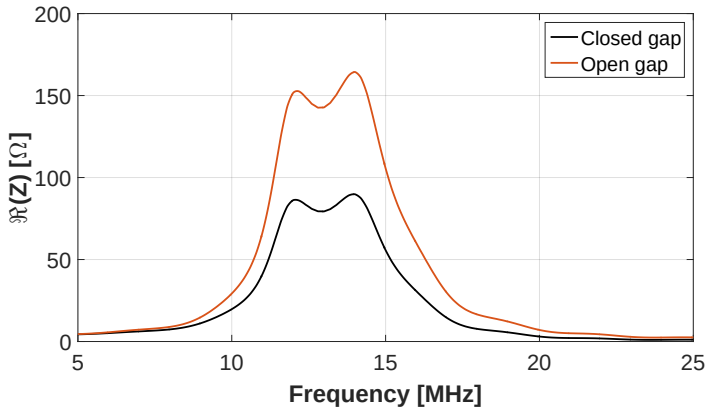

Figure 6.30: Real part of the gap impedance of the 10 MHz cavity tuned to h=8 as computed through CST simulations, when one gap is short-circuited by a gap relay. The orange trace is the impedance of the gap left open, while the black one is the impedance of the gap short-circuited by the gap relay.

The further reduction of the impedance, due to the combined effect of the cavity resonance set by the gap relay and a series resonance is also demonstrated. The series resonance is related to the cavity-amplifier geometry properties, since the reduction tends to become less significant when the gap relay inductance value changes (Fig. 6.31).
CST gives the possibility to define field monitors for transient simulations, providing

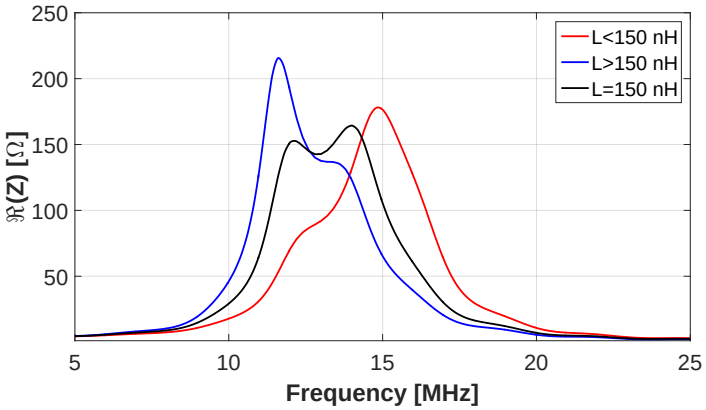

Figure 6.31: Gap impedance variation, due to different values of the gap relay equivalent inductance L.

additional information on the electromagnetic field distribution inside the structure. Figure 6.32 shows the distribution of the wake field along the z axis in the cavity structure. As expected, the maximum of the field is generated on the ceramic gap. A bunch travelling in the longitudinal directions generates a wake field which is higher across the gap left open, compared to the short-circuited one.

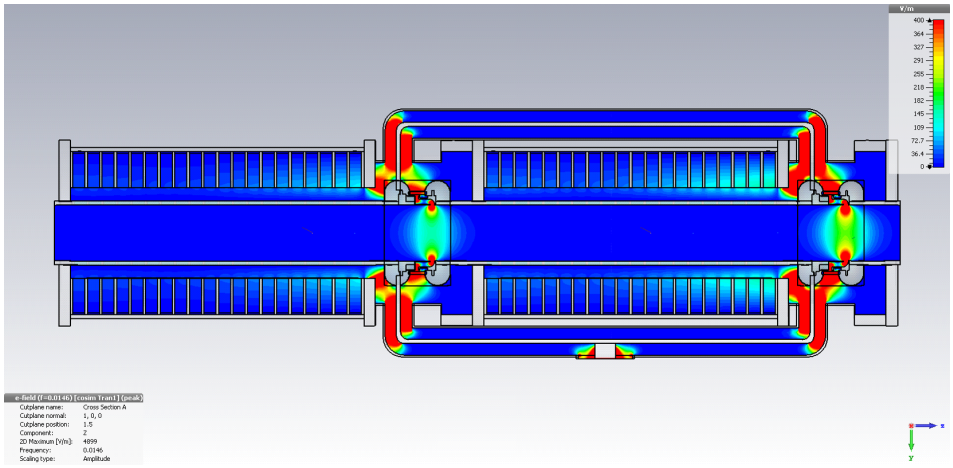

Figure 6.32: Wake field distribution along the z axis of the 10 MHz when only the left relay is closed.

The numerical simulations and the analysis of the circuit pointed out that the main contribution to the asymmetry comes from the coupling bar connecting the two gaps. It was found that at high frequencies the electrical delay of the line influences the

coupling between the two half resonators, making it less tight than expected. In addition, the geometry of the line reduces further the coupling; this geometric effect can be reproduced in PSPICE simulations, by adding inductance in series to the coupling lines, to model the line discontinuities. On the other hand, the magnetic coupling does not seem to give any contribution to the voltage distribution.

6.3 Validation of the upgraded amplifier

The measurement technique described in Sec. 6.1 has been applied for the characterization of the cavities installed in the PS ring in order to evaluate the impedance contribution of the 10 MHz system to the total PS impedance. In this context, a dedicated measurement campaign has been carried out for the validation of the upgraded amplifier.

The upgraded amplifier, described in Chap. 4, has been installed in the PS ring during the winter technical stop 2015/16 and it presently drives the cavity in straight section 11.

The tests have been performed by measuring the induced voltage and the beam intensity in time and frequency domain. The measurement set-up is illustrated in Fig. 6.33.

A Keysight LAN/GPIB/USB Gateway device provides a communication bridge between the PC and the instruments, via Ethernet. The instruments are connected to the gateway via GPIB interfaces and are remotely controlled using a dedicated Matlab code which allows to automate the measurements and the data acquisition.

The induced voltage in a cavity gap by a n-ToF beam at h=8 has been measured on several cavities. Cavity 11 was initially operated by a standard amplifier and the results are shown in Fig. 6.13. After the installation of the upgraded amplifier in the PS ring new measurements have been carried out to evaluate the effective impedance reduction, by comparing the performance of cavity 11 when operated by a standard amplifier and by the upgraded one.

The measurement results, shown in Fig. 6.34, confirm the expected reduction of the impedance, which is maintained across the full frequency operating range of the cavity. Major attention is given to the frequency corresponding to h=21, since LHC-type beams are accelerated at this harmonic.

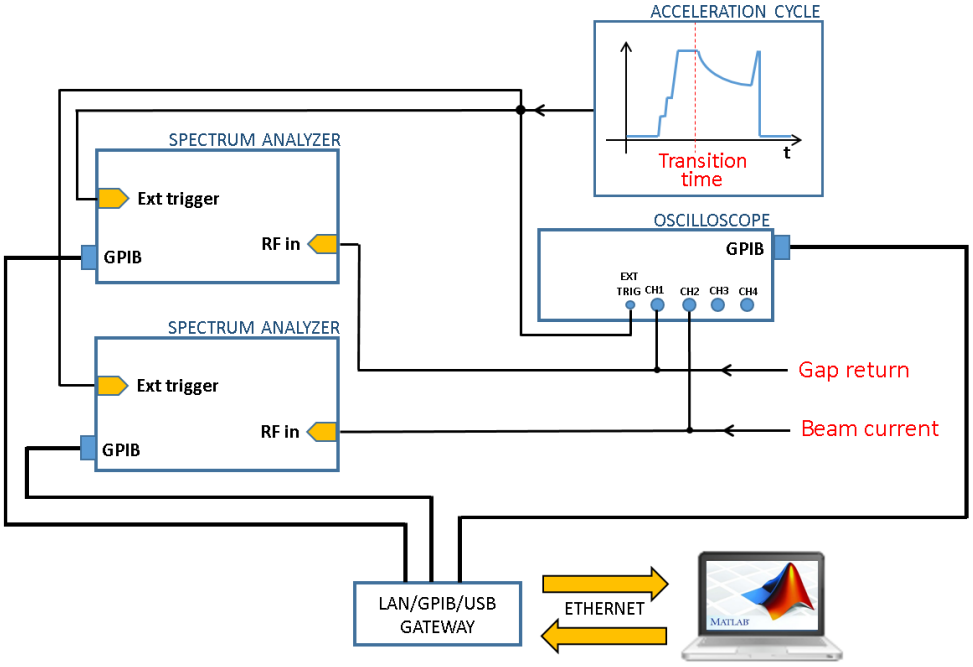

Figure 6.33: Set-up used for measuring the beam induced voltage and the beam current. The two spectrum analyzers on the left acquire the induced voltage and the beam current spectra; on the right the oscilloscope measures both signals in time domain. The instruments are connected to a LAN/GPIB/USB Gateway.

These measurements were performed with the driving power to the amplifier chain set to zero, so that the voltage measured across the cavity gap is only due to the contribution of the beam current. Additional measurements took place to analyze the performance of the PS cavities when the accelerating RF voltage is generated across the gap.

The voltage induced by a n-ToF beam has been measured in the frequency domain and Fig. 6.35 reports the measured beam and the gap voltage spectra. The lines are spaced by ∼470 kHz, corresponding to the revolution frequency of the PS.

The duration of the bunch allows to use the short-bunch approximation $I_{rf} \approx 2 \cdot I_{DC}$, where:

$$I_{DC} = N_b \cdot q \cdot f_{rev} \approx 8 \cdot 10^{12} 1.6 \cdot 10^{19} \cdot 470\,\text{kHz} \approx 0.5\,\text{A} \tag{6.6}$$

In the frequency range up to 15 MHz, in fact, the amplitude of the beam spectrum lines (Fig. 6.35) is ∼1 A. Since the cavity energy decay time is short enough compared

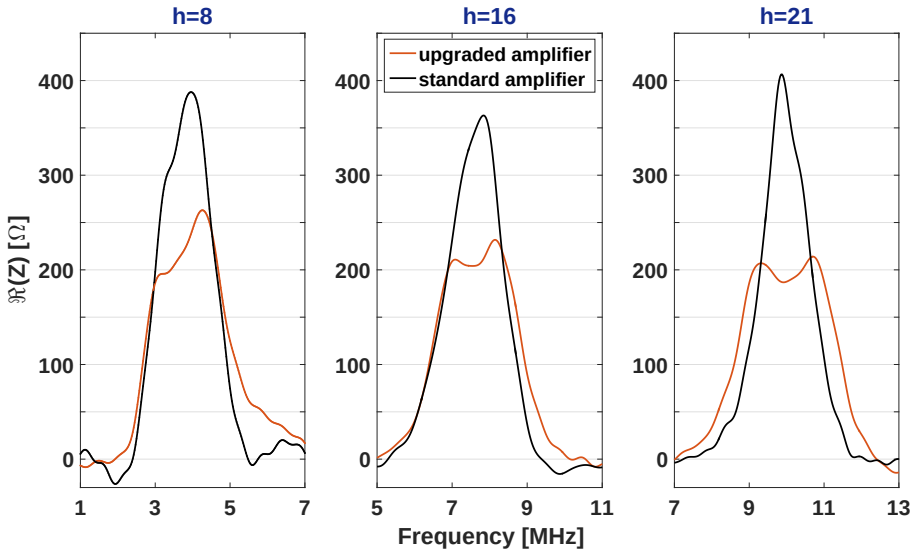

Figure 6.34: Real part of the gap impedance of PS cavity in straight section 11 operated with a standard (black) and the upgraded amplifier (orange).

to the revolution period, the impedance is approximately obtained, by normalizing the induced voltage to the beam current. The impedance has been measured by varying the voltage in one gap from 0 to 10 kV_p, in steps of 2 kV_p. In order to provide a total of 200 kV_p accelerating voltage to the beam (usually achieved using ten cavities), ten plus the spare cavity 11 have been used. For varying the gap voltage of the cavity under test, a second cavity was used such as the sum of the voltages on both cavities gaps is kept at 20 kV_p (Fig. 6.36).

Figure 6.37 plots the results of the gap impedance computation of three cavities at the harmonics multiple of the revolution frequency. For gap voltages $>0\,V_p$ the component at h=8 has been removed. Cavities 36 and 56 are chosen since they feature respectively the highest and the lowest impedance among the 11 cavities installed in the machine.

Since the fine tuning loop starts working when the voltage on the cavity gap reaches $\sim$700 V_p, the shape of the impedance of cavity 11 and 36 is different at 0 V_p. Then it become more and more flat increasing the gap voltages. Cavity 56, instead, presents an overshoot on the edges of the passband, meaning that the stability margins are reduced. This may be related to the working point of the tubes: in the new configuration of the amplifier, the bias current of the tubes is higher compared to the standard

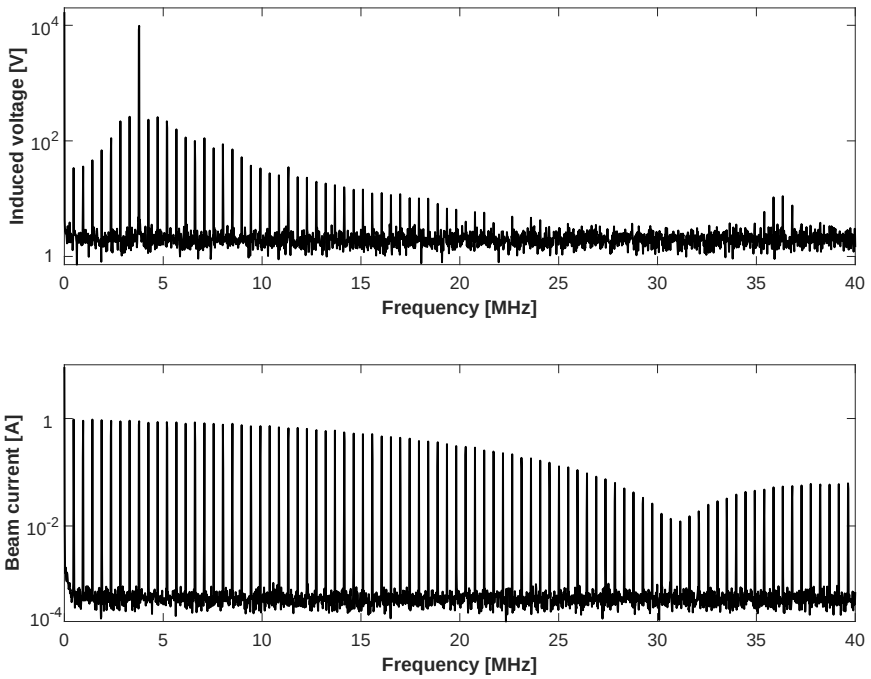

Figure 6.35: Measurements of the n-ToF beam (h=8, bunch length∼60ns) and the induced voltage spectra during transition crossing. The spectrum lines are spaced by f_{rev}.

configuration. Since the transconductance of the tubes is closer to the maximum value, the difference of the forward gain of the amplifier chain between high and low field is smaller. Contrarily, the increase of the transconductance of the tubes in the standard configuration of the amplifier leads to an increase of the forward gain of the amplifier chain, and thus of the loop gain. This causes a reduction of the impedance and a consequent reduction of the stability margins, which is more significant for cavity 56.

Keeping the stability margins large enough is an important requirement to maximize the compensation provided by the 1-turn delay feedback. The latter reduces the impedance at the revolution harmonics, by re-injecting an anti-phase signal to the amplifier driving the cavity, with a time delay equal to the revolution period. The main limitation to the performance of the 1-turn delay feedback system is given by the delay of the 10 MHz system and electronics, because the 1-turn delay feedback,

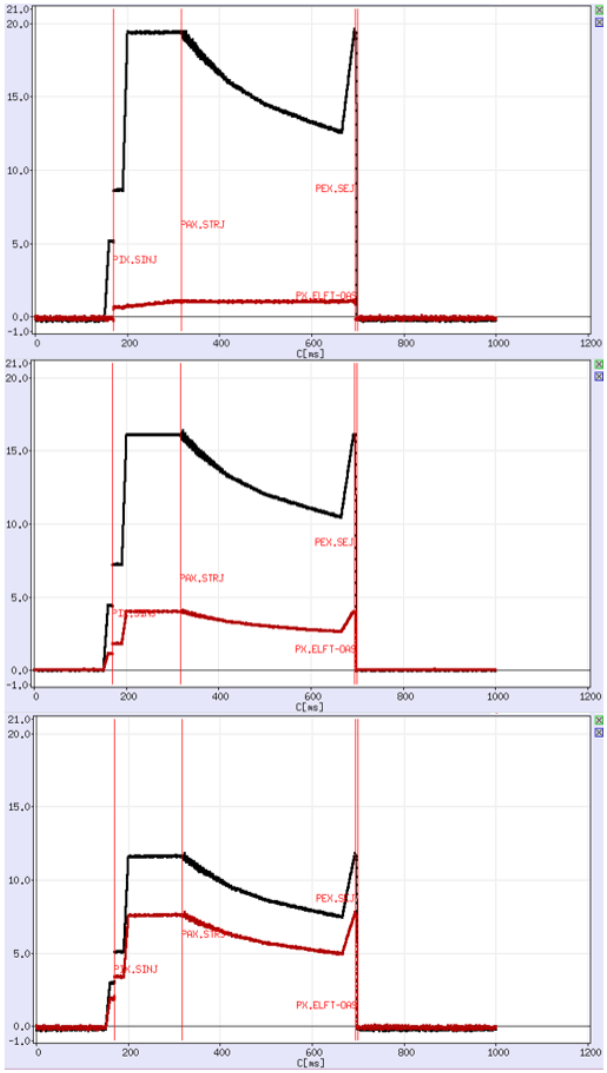

Figure 6.36: Distribution of a total cavity voltage of $20\,\mathrm{kV_p}$ ($10\,\mathrm{kV_p}$/gap) between two cavities. The black curve represents the voltage program of a cavity under test, while the red curve is the programmed voltage of the "compensating" cavity. Three different cases are shown: *i*) V_{test}=$20\,\mathrm{kV_p}$ - V_{comp}=$0\,\mathrm{kV_p}$, *ii*) V_{test}=$16\,\mathrm{kV_p}$ - V_{comp}=$4\,\mathrm{kV_p}$, *iii*) V_{test}=$12\,\mathrm{kV_p}$ - V_{comp}=$8\,\mathrm{kV_p}$.

in its present configuration, is able to compensate only for a constant delay. If the stability margins are too low they compromise the linearity of the system phase.
In addition, a symmetric shape of the impedance is also important for the 1-turn delay feedback. However, it has been found that the impedance of some cavities become asymmetric when the high voltage is applied to the gap (Fig. 6.38).

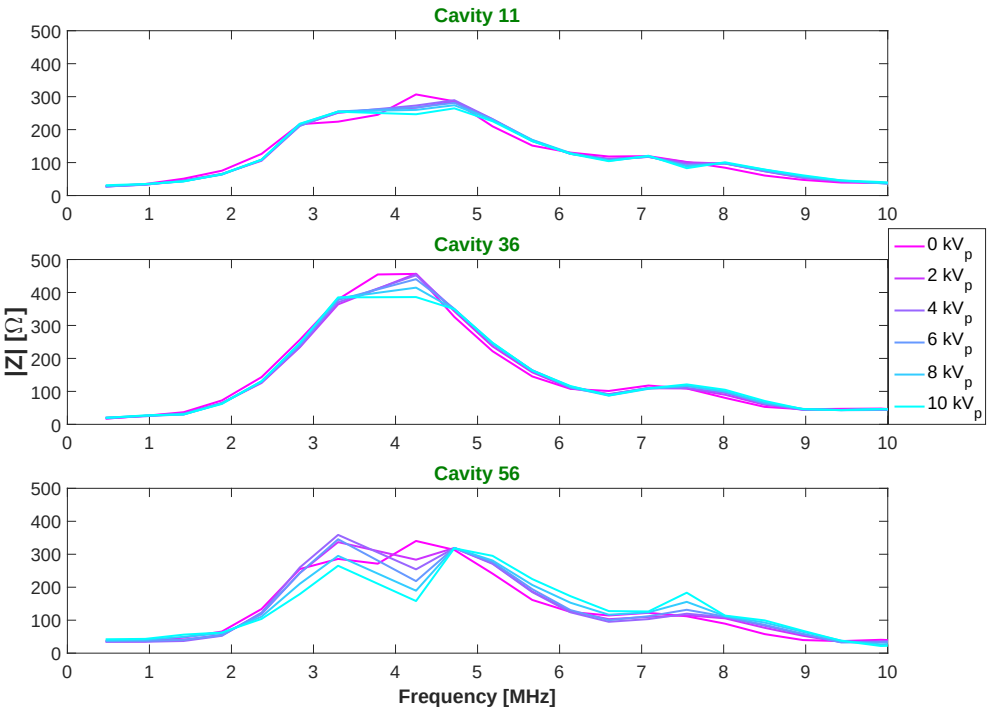

Figure 6.37: Measurements of the gap impedance of cavities in straight sections 11, 36, 56 (tuned to h=8), with different voltages at the cavity gap.

In fact, at high voltage, if the phase shift introduced in the amplifier chain is too large, the Final grid tuning system may not be able to provide the current needed to properly tune the resonator in order to make the shape of the closed loop response, and thus the cavity impedance, symmetric. This may especially happen at 10 MHz, where the tuning current is at its maximum.

In conclusion, at h=8 the new prototype amplifier provides a reduction of the impedance also if compared with cavities featuring the lowest impedance. Moreover, because of the improved stability, the impedance reduction is constant over the operational bandwidth.

A particular interest goes to the performance of the new amplifier at 10 MHz, which is the accelerating frequency of the LHC-type beams (h=21). In order to measure more than one cavity at harmonics higher than h=8, and overcome the limit set by the tuning group acceleration scheme, a new n-ToF-like beam (high intensity single

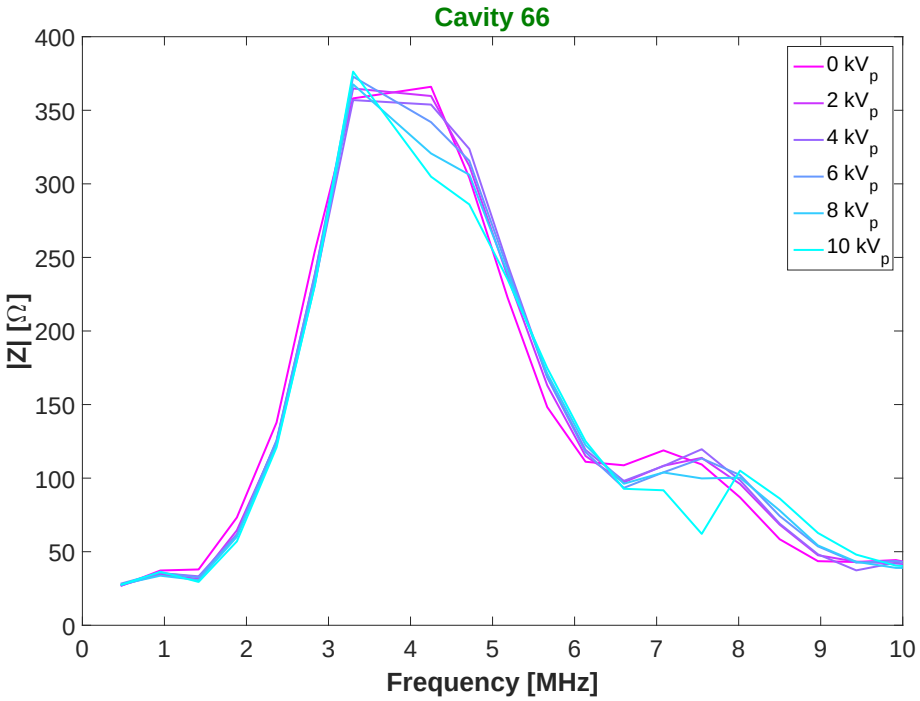

Figure 6.38: Measurements of the gap impedance of the cavity in straight sections 66 at $h = 8$, with different voltages on the cavity gap.

bunch) has been developed.

To perform the same measurements on cavities tuned to h=21, without jeopardising the acceleration process and deteriorating the beam characteristics, the solution consists in adopting a reduced ramp rate acceleration, which hence requires a smaller number of cavities. This new beam is accelerated by a total gap voltage of $120\,\mathrm{kV_p}$, which can be provided by six cavities only, leaving up to five cavities available for the measurements. In order to keep the same bucket area of the n-ToF beam (which uses $200\,\mathrm{kV_p}$), according to Eq. 1.15, the programmed B field slope characteristic is set at $\frac{dB}{dt} = 1.1\,\mathrm{T/s}$, which is half of the one used for the operational n-ToF cycle. The intensity of the beam is $\sim 4 \cdot 10^{12}$ ppb.

Measurements of the gap impedance as seen by the beam were performed on all the PS cavities, at h=8, 16 and 21 and the results are summarized in Fig. 6.39.

It is clear that in the three cases the new cavity-amplifier system in straight section 11 is able to provide a reduction of the impedance as seen by the beam, if compared to

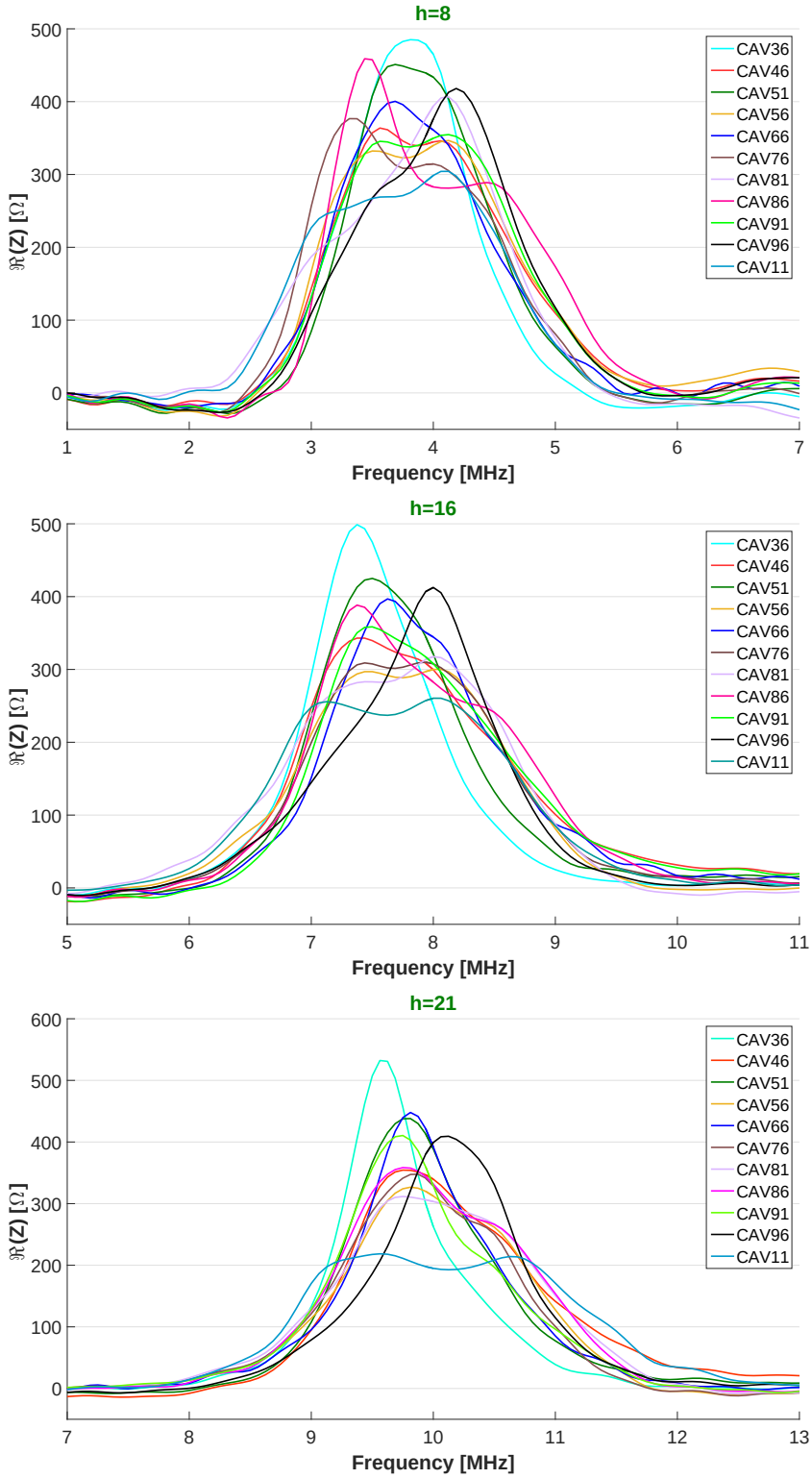

Figure 6.39: Measurements of the gap impedance of the PS cavities at h=8, h=16, h=21.

the standard systems of the PS. Since all the cavities feature different performances, this reduction can be more or less significant and the highest reduction is achieved at 10 MHz. The reduction of the impedance can vary from a factor of ∼1.5 to more than 2 (3-6 dB).
In addition, the impact of the beam intensity on the cavity impedance has been analyzed, by measuring the induced voltage on the cavity gap and by varying the number of protons per bunch from $\sim 4 \cdot 10^{12}$ to $\sim 2 \cdot 10^{12}$. Measurements were also performed on the cavity in straight section 11, driven by the upgraded amplifier (Fig. 6.40), and on the cavity in straight section 36, driven by a standard amplifier (Fig. 6.41). In both cases the intensity variation does not significantly affect the cavity gap impedance.

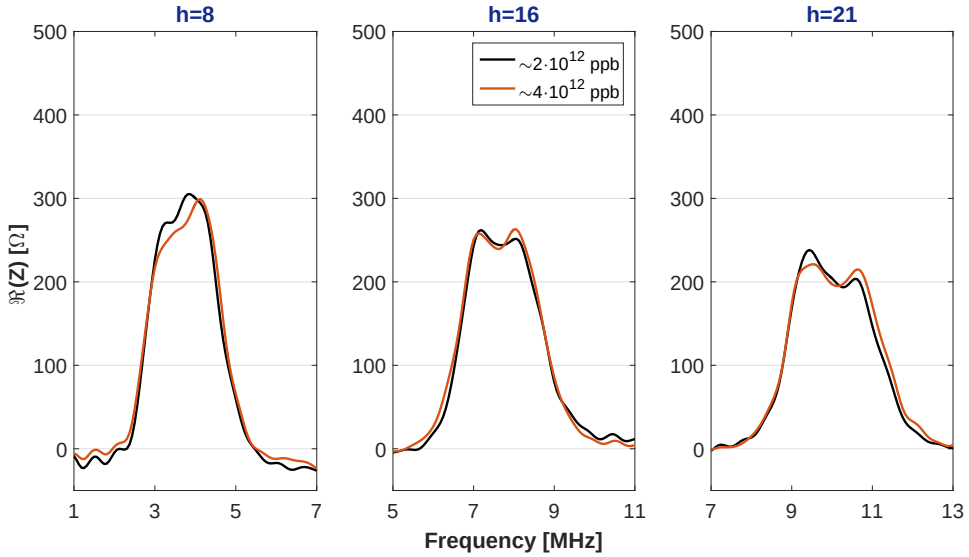

Figure 6.40: Measurements of the gap impedance of the cavity in straight section 11 at h=8, 16, and 21 as seen by a single bunch beam of intensities $\sim 4 \cdot 10^{12}$ and $\sim 2 \cdot 10^{12}$.

In order to directly observe the effect of the new cavity-amplifier system on the longitudinal beam stability, at least four PS 10 MHz amplifiers should be upgraded. Presently, the main limit is given by the available cooling system installed in the ring, which is not able to provide the additional water flow needed to supply more than one upgraded amplifier.
An upgrade of the cooling system is therefore foreseen in the perspective of replacing

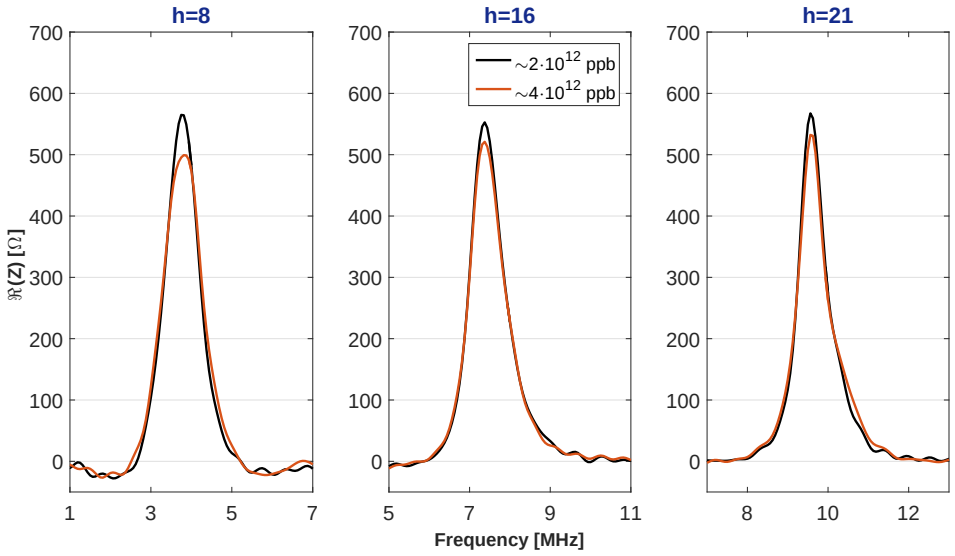

Figure 6.41: Measurements of the gap impedance of the cavity in straight section 36 at h=8, 16, and 21 as seen by a single bunch beam of intensities $\sim 4 \cdot 10^{12}$ and $\sim 2 \cdot 10^{12}$.

all the PS 10 MHz amplifiers during the LS2 in 2019.

Despite the promising results achieved so far, a possible optimization of the upgraded configuration will be studied in the next reference period. Moreover, the possibility to replace the first two stages with a solid state amplifier is being investigated, in order to increase the gain in the forward chain and thus the loop gain.

Conclusions

In the framework of the LHC Injectors Upgrade (LIU), an impedance reduction campaign is planned to mitigate the impedance sources responsible for longitudinal beam instabilities. These instabilities are a significant limitation for the future doubling of bunch intensity required by the Hi-Lumi LHC (HL-LHC) project.
An upgrade of the PS 10 MHz RF system has therefore become mandatory to reduce its impedance contribution and limit the beam induced voltage (beam loading). The reduction of beam loading can be achieved by improving the fast feedback of the power amplifier chain driving the cavities.
This thesis focused on the design, development, characterization and optimization of a prototype feedback amplifier featuring an increased loop gain, providing a stable operation and presenting a limited re-design of the present system.
Simulations of the amplifier system were complemented by several measurement campaigns. In fact, carried out in parallel allowed feeding back the results into the development of models and prototypes. This resulted in a complete PSPICE model, able to reproduce accurately the behaviour of the system, including the tubes for which dedicated libraries were developed.
During the development of the amplifier prototype, RF measurement techniques have been proposed to characterize the elements of the amplifier chain and validate the upgrade in terms of stability of the system. Innovative solutions have been explored to improve the performance of the system. Among those, a measurement technique was developed to evaluate ferro-magnetic material characteristics and their variation when exposed to bias fields or under the effect of a variable RF signal amplitude. Ferrite in fact, is largely used in the amplifier chain, as well as core of the accelerating cavities, and it deeply affects the final performance of the system. The results were helpful and offered the needed insight for the construction of new RF devices, as

well as a deeper understanding of the system behaviour. Moreover, an innovative combined orthogonal-parallel bias method has been tested, aiming at reducing the ferrite losses. This technique, usually used for garnets, has been found promising for our purposes, providing a reduction of the losses by a factor of 2, compared with a standard orthogonal or parallel bias method. It will be therefore further investigated in the future, possibly finding an application in the optimization of our upgraded amplifier.

A complete and accurate impedance model is essential to understand the nature of the beam instabilities and eventually plan possible cures. For these reasons, dedicated measurements were performed to investigate the beam cavity interaction, evaluate the beam induced voltage and understand how the cavity geometry and the amplifier circuit influence the distribution of the induced voltage in the cavities and their impedance. Since the PSPICE model has proven to be a powerful tool for the synthesis of a complex system, as well as for the characterization of single circuit elements, it has been crucial for the beam-cavity interaction studies.

From the beam induced voltage measurements, a first evaluation of the PS 10 MHz cavity impedance was obtained and found compatible with the predictions, confirming the PSPICE simulations. In order to benchmark the results, a CST model of the cavity has been also developed, which accounts for the ferrite characteristics evaluated with the aforementioned technique. Since the total cavity impedance depends on the Final tube resistance and is reduced by the fast feedback action, the possibility to combine PSPICE and CST was explored, resulting in a powerful and quite complete model of the cavity-amplifier system.

By means of a comprehensive set of simulations, using different CST simulation solvers, a correct interpretation of the beam-cavity interaction was obtained and it has been found that the coupling impedance of the cavity, used in the studies of coupled-bunch instabilities, was underestimated by a factor of 4.

Last and not least, a measurement campaign was dedicated to the validation of the prototype of the upgraded amplifier. Its performance was compared to all the standard amplifiers installed in the PS ring. All cavities were found to feature a different impedance, nevertheless the upgraded amplifier prototype proved to reduce the cavity impedance. This improvement was most significant at 10 MHz and was quantified by a factor of 1.5 if compared to the cavity showing the lowest impedance to more than

a factor of 2, if compared to the cavity with the highest impedance.
Additionally, the impact of the increasing input RF power on the stability of the system was evaluated by measuring the coupling impedance of the cavity and by varying the RF voltage on the gap from zero to the maximum. The results confirmed the improved stability of the new amplifier, compared to the standard one, also when driven by an high input signal.
All these studies, culminating in a comprehensive model of the PS 10 MHz system impedance, allowed finally to understand its real contribution to the longitudinal impedance budget. A further optimization will be performed in the future: for instance, new measurements of the incremental ferrite permeability will provide the possibility to simulate the system in the full operating 3-10 MHz range.
The results achieved with the new amplifier let us envisage a significant improvement of the beam characteristics if extended to other amplifiers. To fully validate the upgrade in terms of beam dynamics, the upgrade of most of the amplifiers driving the PS cavities and their cooling system would be required. The upgrade of the full PS 10 MHz system is expected to be accomplished during the LS2 in 2019, in preparation of the Run 3 of the LHC.
In the next reference period, an optimization of the proposed solutions will be completed, aiming at renewing the layout of the present amplifier and possibly reducing the chain group delay.
Despite the vacuum tube configuration is preferred for radiation hardness reasons, the possibility to replace the first two stages with a solid state amplifier is under investigation and may possibly lead to an additional increase of gain in the forward chain.

Appendix A

Electron tubes PSPICE libraries

```
** RS1084CJ PSpice Model**

.SUBCKT RS1084 10 20 30 50 ;(CATH GRID ANODE SCREEN)
Gk 40 14 value = {v(7,10)*(i(vmg)+i(vms)+i(vma))};cathode I
Gs 50 15 value = {v(4,10)*v(5,10)*v(7,10)};screen I
Gg 20 12 value = {v(6,10)*1};grid I
*IA as fn(Vg,Va)
Ga 30 10 value = {IF((v(20,10)>-400 & V(20,10)<160),
+ V(7,10)*(V(100,10)+
+ V(101,10)*V(20,10)+
+ V(102,10)*V(20,10)*V(20,10)+
+ V(103,10)*V(20,10)*V(20,10)*V(20,10)+
+ V(104,10)*V(20,10)*V(20,10)*V(20,10)*V(20,10)+
+ V(105,10)*V(20,10)*V(20,10)*V(20,10)*V(20,10)*V(20,10)+
+ V(106,10)*V(20,10)*V(20,10)*V(20,10)*V(20,10)*V(20,10)*V(20,10)+
+ V(107,10)*V(20,10)*V(20,10)*V(20,10)*V(20,10)*V(20,10)*V(20,10)*V(20,10)),0)};anode I

*tables of coefficient for the Anode current fitted with 7th degree polynomial curve
E100 100 10 table {v(30,10)}= (5000, 41.9648) (7000, 43.624)
+(9000, 45.2858) (11000, 46.9502) (13000, 48.6205)
+(15000,50.3043) (17000,52.0133) (19000,53.7621)
+(21000,55.5678) (23000,57.4475) (25000,59.4170)

E101 101 10 table {v(30,10)}=(5000, 0.2328) (7000, 0.2341)
+(9000, 0.2353) (11000, 0.2367) (13000, 0.2386)
+(15000,0.2414) (17000,0.2454)(19000, 0.2509)
+(21000, 0.2579) (23000, 0.2664) (25000, 0.2760)

E102 102 10 table {v(30,10)} = (5000, 1.3645e-4) (7000, 1.2777e-4)
```

```
+(9000, 1.3029e-4) (11000, 1.4638e-4) (13000, 1.7713e-4)
+(15000,2.2188e-4) (17000,2.7783e-4)(19000,3.3963e-4)
+(21000,3.9911e-4) (23000,4.4505e-4) (25000,4.6306e-4)

E103 103 10 table {v(30,10)} = (5000, -1.4955e-7) (7000, 3.4072e-8)
+(9000, 2.8689e-7) (11000, 5.7784e-7) (13000,8.6186e-7)
+(15000,1.0796e-6) (17000,1.1578e-6) (19000,1.0098e-6)
+(21000,5.3731e-7) (23000,-3.6796e-7) (25000,-1.8214e-6)

E104 104 10 table {v(30,10)} = (5000, -2.02084588943315e-09)
+(7000, -1.12296968677845e-09) (9000, -7.23071952471881e-10)
+(11000, -1.12556004609089e-09) (13000, -2.65791717710979e-09)
+(15000,-5.66291148060100e-09) (17000,-1.04899433134197e-08)
+ (19000,-1.74856156708289e-08) (21000,-2.69836296001735e-08)
+(23000,-3.92941350636033e-08) (25000,-5.46927070715925e-08)

E105 105 10 table {v(30,10)} = (5000, -1.59544776497352e-11)
+(7000,-2.03205561042360e-11)(9000,-2.93230662174935e-11)
+(11000, -4.35568470103972e-11) (13000, -6.35436028153769e-11)
+(15000,-8.97193467123928e-11) (17000,-1.22422669929545e-10)
+ (19000,-1.61883862002320e-10) (21000,-2.08214976955770e-10)
+(23000,-2.61401020225314e-10) (25000,-3.21292511303610e-10)

E106 106 10 table {v(30,10)} = (5000, 3.59771809996351e-14)
+(7000, -5.85033796403767e-15) (9000, -5.66849829662825e-14)
+(11000, -1.16202782086761e-13) (13000, -1.83963063555929e-13)
+(15000,-2.59414208788496e-13) (17000,-3.41899182174316e-13)
+ (19000,-4.30661006744790e-13) (21000,-5.24848440264285e-13)
+(23000,-6.23522169007990e-13) (25000,-7.25661871528166e-13)

E107 107 10 table {v(30,10)} = (5000, 1.68194913642476e-16)
+(7000, 8.96371323026622e-17) (9000, 1.05907807705213e-17)
+(11000, -6.83747801493042e-17) (13000,-1.46711975426593e-16)
+ (15000,-2.23894400906304e-16) (17000,-2.99416068272177e-16)
+ (19000,-3.72790747378774e-16) (21000,-4.43551622612578e-16)
+(23000,-5.11251448162364e-16) (25000,-5.75463345597801e-16)

* Dummy resistors across table nodes
Rd100 100 10 1
```

```
Rd101 101 10 1
Rd102 102 10 1
Rd103 103 10 1
Rd104 104 10 1
Rd105 105 10 1
Rd106 106 10 1
Rd107 107 10 1

*E4 & E5 describe Is as fn(Va,Vg=0v) & Is as f(Vg,Va=2kV)

E4 4 10 table {v(30,10)} = (1.1k,12) (1.2k,8) (1.7k,4) (2.3k,2)
+(3.3k,1) (4.8k,0.5) (10k,0.2) (15k, 0)

E5 5 10 table {v(20,10)} = (-290,0) (-270,0.025) (-250,0.0625)
+(-210,0.125) (-170,0.25) (-100,0.5)
+ (0,1) (100,1.5) (220,2.67) (280,4)

*E6=grid I as fn(Vg)
E6 6 10 table {v(20,10)} = (0,0) (23,1) (50,1.5) (80,1.8)

*E7 truncates all I for Va<2k
E7 7 10 table {v(30,10)} = (1950,0) (2000,1)

*Electrode capacitances
Ckg2 10 50 12pF
Cka 30 10 0.3pF
Cag1 30 20 1.9pF
Cg1k 20 10 136pF
Cg1g2 50 20 165pF
Cag2 30 50 43pF

* Dummy resistors across table nodes
Rd4 4 10 1MEG
Rd5 5 10 1MEG
Rd6 6 10 1MEG
Rd7 7 10 1MEG
Rd40 40 10 1
Rd50 50 10 1MEG
```

```
* I meas.voltmeters
Vms 15 10 0
Vmk 14 10 0
Vma 13 10 0
Vmg 12 10 0
.ENDS


**YL1056 PSpice Model, Vs = 400 V**

.SUBCKT YL1056-400VS 10 20 30 50 ;(CATH GRID ANODE SCREEN)
Gk 40 14 value = {v(7,10)*(i(vmg)+i(vms)+i(vma))};cathode I
Gs 50 15 value = {v(4,10)*v(5,10)*v(7,10)};screen I
Gg 20 12 value = {v(6,10)*1};grid I
*IA as fn(Vg,Va)
Ga 30 10 value = {IF(v(20,10)>-50,
+V(7,10)*(V(100,10)+
+ V(101,10)*V(20,10)+
+ V(102,10)*V(20,10)*V(20,10)+
+ V(103,10)*V(20,10)*V(20,10)*V(20,10)),0)} ;anode I

* tables of coefficient for the Anode current fitted with 3th degree polynomial curve
E100 100 10 table {v(30,10)}= (200,4.417)(300,4.458) (400,4.4931)
+(600,5.479) (1500,5.723) (2500, 6.684)

E101 101 10 table {v(30,10)}=(200,0.2469)(300,0.2317) (400,0.2683)
+(600,0.3235)(1500,0.3405)(2500,0.4221)

E102 102 10 table {v(30,10)}= (200,0.003968)(300,0.003417) (400,0.00452)
+(600,0.006347) (1500,0.006859) (2500,0.00917)

E103 103 10 table {v(30,10)} = (200,1.508e-05)(300,1.076e-05)
+(400,2.226e-5)(600,4.191e-5)(1500,4.678e-05) (2500, 6.811e-5)

* Dummy resistors across table nodes
Rd100 100 10 1
Rd101 101 10 1
Rd102 102 10 1
Rd103 103 10 1
```

```
*E7 truncates all I for  Va<400
E7 7 10 table {V(30,10)} = (30,0) (400,1)

*E4 & E5 describe Is as fn(Va,Vg=0v) & Is as fn(Vg,Va=.5kV)
E4 4 10 table {v(30,10)} = (300,.8) (450,.7) (500,.65)
+(700,.6) (800,.55) (900,.5) (1.2k,.45)
+(1.4k,0.4) (2.2K,0.3) (3k,0)

E5 5 10 table {v(20,10)} = (-20,.1) (-18,.2) (-12,.3)
+(-10,.4) (-8,.45) (-6,.5)
+(-5,.55) (-2,.6) (0,.65) (1,.7)

*E6=grid I as fn(Vg)
E6 6 10 table {v(20,10)} = (0,0) (9,.5) (18,1)

*Electrode capacitances
Ckg2 10 50 2.2pF
Cka 30 10 0.01pF
Cag1 30 20 0.05pF
Cg1k 20 10 42pF
Cg1g2 50 20 60pF
Cag2 30 50 8.5pF

* Dummy resistors across table nodes
Rd4 4 10 1MEG
Rd5 5 10 1MEG
Rd6 6 10 1MEG
Rd7 7 10 1MEG
Rd40 40 10 1
Rd50 50 10 1MEG

* I meas.voltmeters
Vms 15 10 0
Vmk 14 10 0
Vma 13 10 0
Vmg 12 10 0
.ENDS
```

```
**YL1056 PSpice Model, Vs = 300 V**

.SUBCKT YL1056-300VS 10 20 30 50 ;(CATH GRID ANODE SCREEN)
Gk 40 14 value = {v(7,10)*(i(vmg)+i(vms)+i(vma))};cathode I
Gs 50 15 value = {v(4,10)*v(5,10)*v(2,10)};screen I
Gg 20 12 value = {v(6,10)*1};grid I
*IA as fn(Vg,Va)
Ga 30 10 value = {IF(v(20,10)>-38,
+V(7,10)*(V(100,10)+
+ V(101,10)*V(20,10)+
+ V(102,10)*V(20,10)*V(20,10)+
+ V(103,10)*V(20,10)*V(20,10)*V(20,10)),0)} ;anode I

* tables of coefficient for the Anode current fitted with 3th degree polynomial curve
E100 100 10 table {v(30,10)}= (200,2.79)(300,2.762) (400,2.732)
+(600,2.821) (2500,3.002)

E101 101 10 table {v(30,10)}=(200,0.2195)(300,0.1974) (400,0.1769)
+(600,0.1802 )(2500,0.1859)

E102 102 10 table {v(30,10)}= (200,0.005695)(300,0.004367) (400,0.003209)
+(600,0.003226) (2500,0.003207)

E103 103 10 table {v(30,10)} = (200,4.861e-05)(300,2.815e-05)
+(400,1.131e-5)(600,1.131e-5)(2500,1.012e-05)

* Dummy resistors across table nodes
Rd100 100 10 1
Rd101 101 10 1
Rd102 102 10 1
Rd103 103 10 1

*E7 truncates all I for Va<300
E7 7 10 table {V(30,10)} = (30,0) (300,1)

*E4 & E5 describe Is as fn(Va,Vg=0v) & Is as fn(Vg,Va=.5kV)
E4 4 10 table {v(30,10)} = (500,.4) (800,.35) (1.1k,.3) (1.5,.25) (3k,.2)
E5 5 10 table {v(20,10)} = (-12,.1) (-7,.2) (-5,.25) (-4,.3) (-2,.35) (0,.4)
```

```
*E6=grid I as fn(Vg)
E6 6 10 table {v(20,10)} = (0,0) (9,.5) (13,.75)

*Electrode capacitances
Ckg2 10 50 2.2pF
Cka 30 10 0.01pF
Cag1 30 20 0.05pF
Cg1k 20 10 42pF
Cg1g2 50 20 60pF
Cag2 30 50 8.5pF

* Dummy resistors across table nodes
Rd4 4 10 1MEG
Rd5 5 10 1MEG
Rd6 6 10 1MEG
Rd7 7 10 1 MEG
Rd40 40 10 1
Rd50 50 10 1MEG

* I meas.voltmeters
Vms 15 10 0
Vmk 14 10 0
Vma 13 10 0
Vmg 12 10 0
.ENDS
```

In the following the amplifier circuit in the standard configuration is shown, followed by the PSPICE models of the standard and the upgraded system.

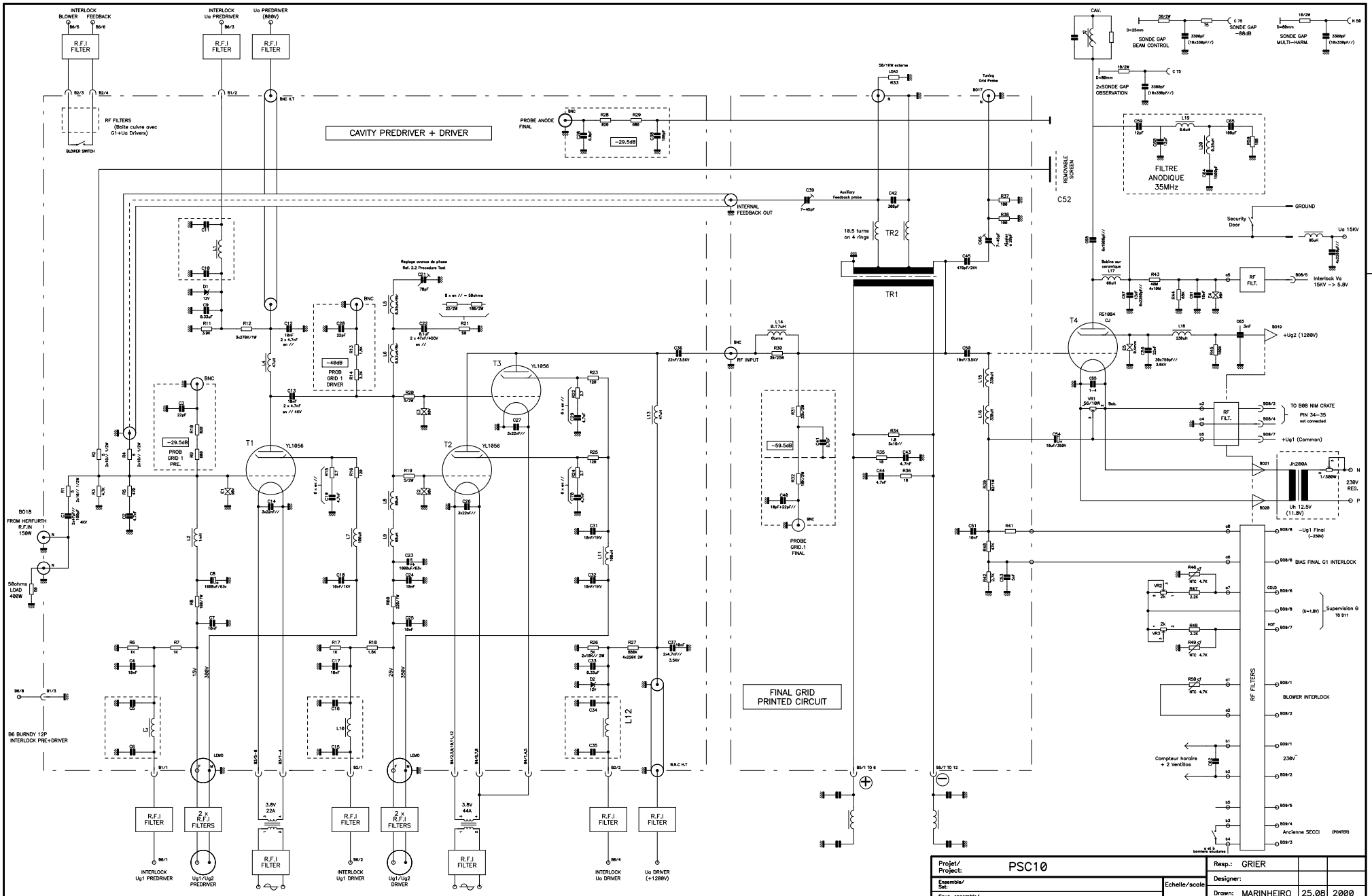

Projet/ Project:	PSC10		Resp.: GRIER	
Ensemble/ Set:		Echelle/scale	Designer:	
Sous-ensemble/ Underset:			Drawn: MARINHEIRO	25.08 2000
Document:	POWER AMPLIFIER PLUG-IN WITH LOCAL RF FEEDBACK FOR THE FERRITE CAVITIES OF THE CERN PS	1/1	MODA:	
			MODB:	
			File: 30447001.SCH	INDICE
LABORATOIRE EUROPEEN POUR LA PHYSIQUE DES PARTICULES EUROPEAN LABORATORY FOR PARTICLE PHYSICS GENEVE / GENEVA		Ref: nb	PS\RF-HC 3044/7-1	

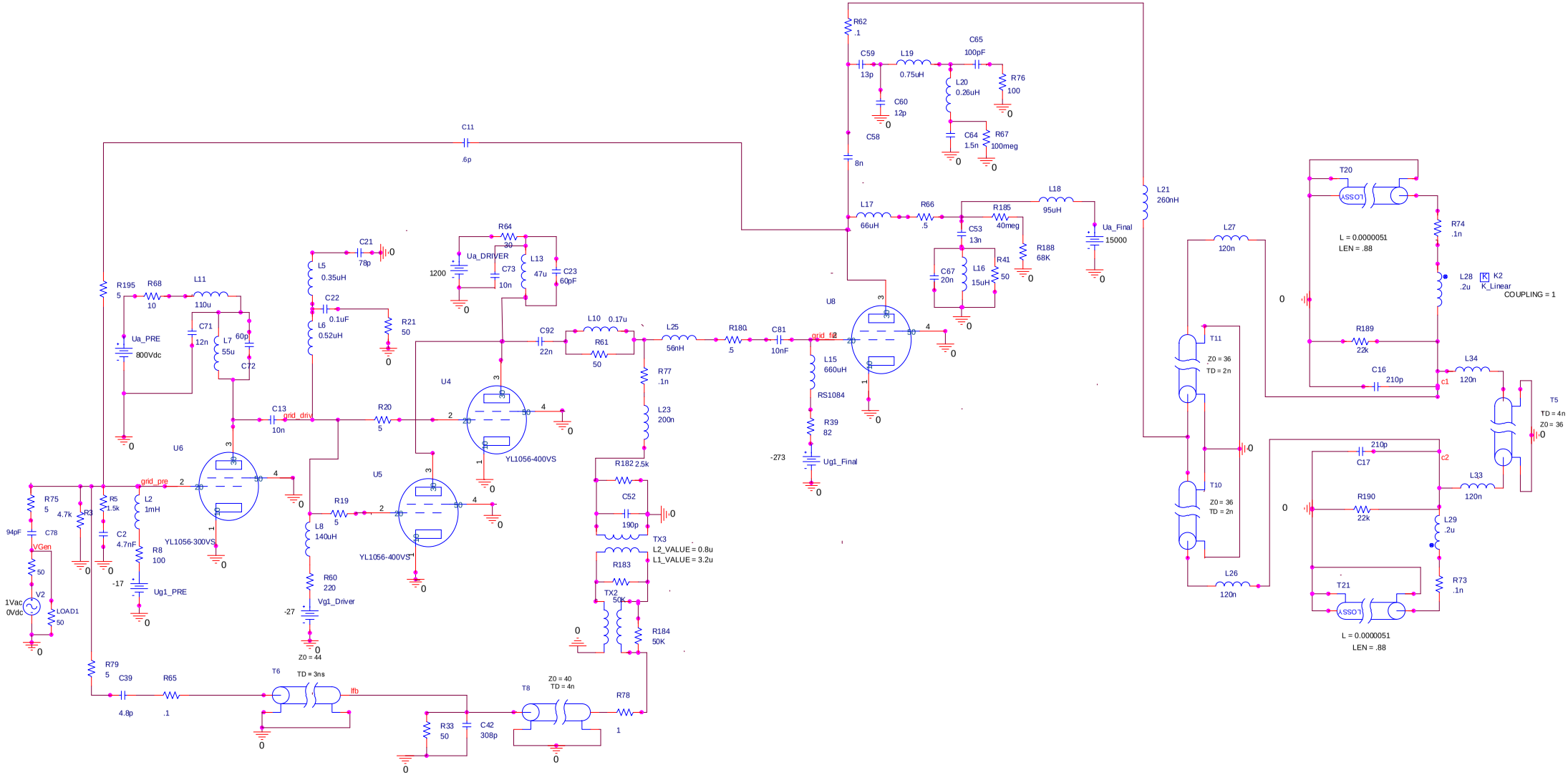
C11
.6p
R62
.1
C65
100pF
C59
13p
L19
0.75uH
L20
0.26uH
R76
100
C60
12p
C58
8n
C64
1.5n
R67
100meg
L18
95uH
L17
66uH
R66
.5
R185
40meg
C53
13n
C67
20n
L16
15uH
R41
50
R188
68K
Ua_Final
15000
L21
260nH
R64
30
Ua_DRIVER
1200
C73
10n
L13
47u
C23
60pF
C21
78p
L5
0.35uH
C22
0.1uF
L6
0.52uH
R21
50
R195
5
R68
10
L11
110u
Ua_PRE
800Vdc
C71
12n
L7
55u
60p
C72
C13
10n
grid_driv
R20
5
C92
22n
L10
0.17u
R61
50
L25
56nH
R180
.5
C81
10nF
grid_fb
U8
U4
U6
U5
YL1056-400VS
YL1056-300VS
R77
.1n
L23
200n
R182 2.5k
C52
190p
TX3
L2_VALUE = 0.8u
L1_VALUE = 3.2u
R183
TX2
50K
R184
50K
L15
660uH
RS1084
R39
82
Ug1_Final
-273
R75
5
4.7k
R3
R5
1.5k
L2
1mH
C2
4.7nF
R8
100
Ug1_PRE
-17
94pF
C78
VGen
V2
1Vac
0Vdc
LOAD1
50
R19
5
L8
140uH
R60
220
Vg1_Driver
-27
Z0 = 44
R79
5
C39
4.8p
R65
.1
T6
TD = 3ns
Ifb
T8
Z0 = 40
TD = 4n
R78
1
R33
50
C42
308p
T20
ASSO1
L = 0.0000051
LEN = .88
R74
.1n
L28
.2u
K2
K_Linear
COUPLING = 1
R189
22k
C16
210p
L34
120n
T5
TD = 4n
Z0 = 36
L27
120n
T11
Z0 = 36
TD = 2n
T10
Z0 = 36
TD = 2n
L26
120n
C17
210p
R190
22k
L33
120n
L29
.2u
T21
R73
.1n
L = 0.0000051
LEN = .88

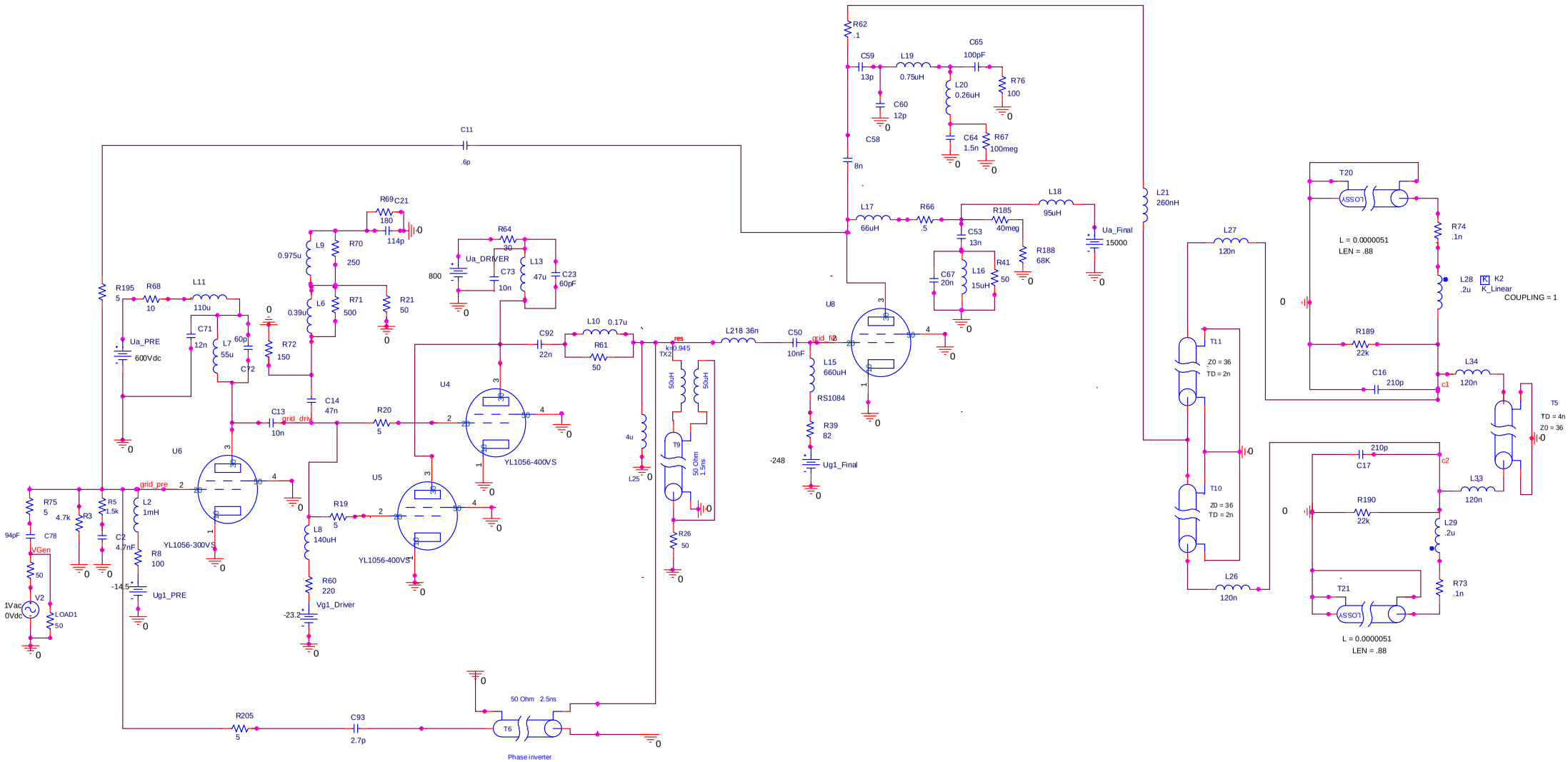
C11
.6p
R62
.1
C59
13p
L19
0.75uH
C65
100pF
L20
0.26uH
R76
100
C60
12p
C58
8n
C64
1.5n
R67
100meg
L18
95uH
L17
66uH
R66
.5
R185
40meg
C53
13n
C67
20n
L16
15uH
R41
50
R188
68K
Ua_Final
15000
L21
260nH
R69
180
C21
114p
R64
30
Ua_DRIVER
800
C73
10n
L13
47u
C23
60pF
L9
0.975u
R70
250
L6
0.39u
R71
500
R21
50
R195
5
R68
10
L11
110u
C71
12n
L7
55u
60p
C72
Ua_PRE
600Vdc
R72
150
C13
10n
grid_drv
C14
47n
R20
5
U4
YL1056-400VS
C92
22n
L10
0.17u
R61
50
4u
L25
res
k=0.945
TX2
50uH
50uH
T9
50 Ohm
1.5ns
R26
50
L218 36n
C50
10nF
grid_fb
U8
L15
660uH
RS1084
R39
82
-248
Ug1_Final
U6
YL1056-300VS
grid_pre
L2
1mH
R75
5
4.7k
R3
R5
1.5k
C78
94pF
VGen
50
V2
1Vac
0Vdc
LOAD1
50
C2
4.7nF
R8
100
-14.5
Ug1_PRE
U5
YL1056-400VS
R19
5
L8
140uH
R60
220
Vg1_Driver
-23.2
R205
5
C93
2.7p
T6
50 Ohm 2.5ns
Phase inverter
L27
120n
T11
Z0 = 36
TD = 2n
T10
Z0 = 36
TD = 2n
L26
120n
T20
ASSO1
L = 0.0000051
LEN = .88
R74
.1n
L28
.2u
K2
K_Linear
COUPLING = 1
R189
22k
C16
210p
L34
120n
T5
TD = 4n
Z0 = 36
210p
C17
c2
L33
120n
R190
22k
L29
.2u
R73
.1n
T21
ASSO1
L = 0.0000051
LEN = .88

Appendix B

Figure 42: Gap of the 10MHz cavity.

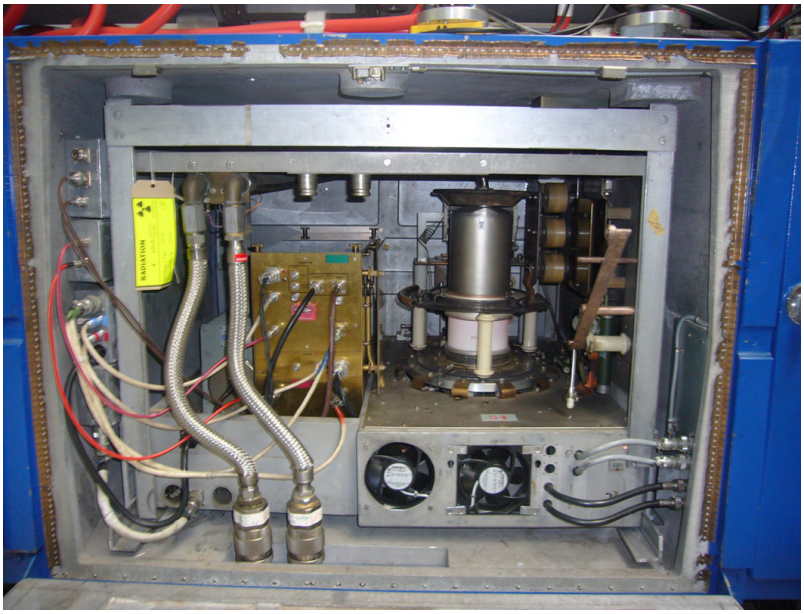

Figure 43: Amplifier installed in the box under the cavity.

Figure 44: Old magnetically tunable autotransformer.

Figure 45: Pieces of the autotransformer.

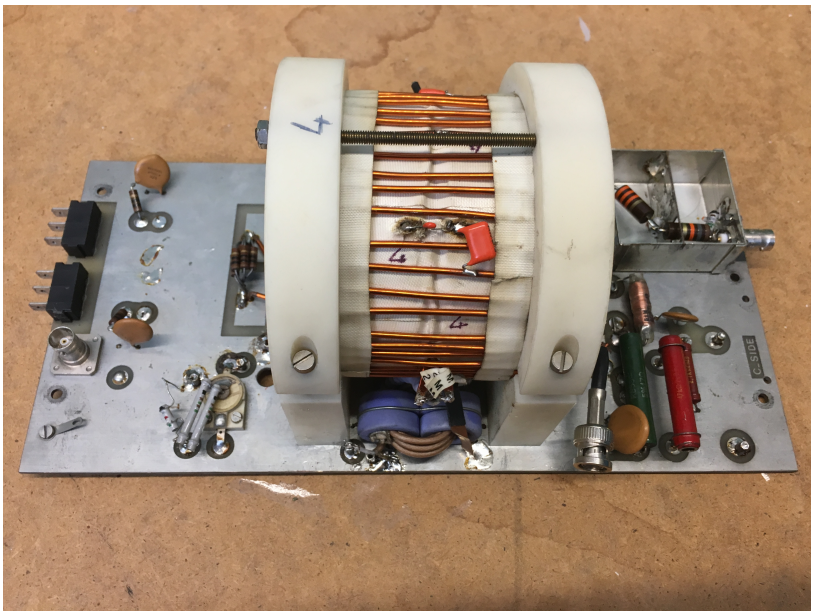

Figure 46: Board housing the old resonator.

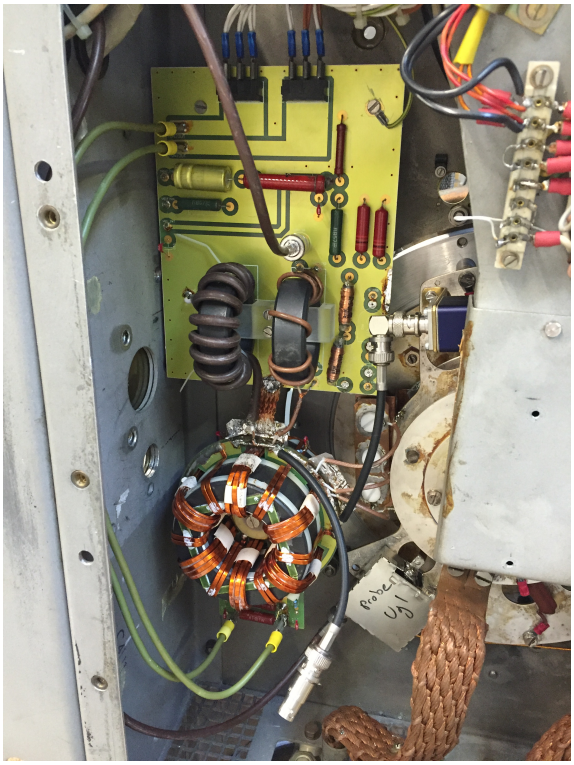

Figure 47: New resonator installed in the amplifier.

Figure 48: "YL1056" tetrode.

Figure 49: "RS1084CJ" tetrode.

References

[1] H. Wiedemann, "Particle accelerator physics", vol. 1. Springer, 2003. 4

[2] S. Y. Lee, "Accelerator Physics." World Scientific, 2004. 4, 9

[3] CERN official webpage, http://home.cern/about. iv, 4, 5, 29

[4] O. Brunining et al., "LHC design report (Volume I, The LHC Main Ring)". CERN, Geneva, Switzerland, 2004. 5

[5] G. Aad, T. Abajyan, B. Abbott, J. Abdallah, S. Abdel Khalek, A. Abdelalim, O. Abdinov, R. Aben, B. Abi, M. Abolins, et al., "Observation of a new particle in the search for the Standard Model Higgs boson with the ATLAS detector at the LHC", Physics Letters B, vol. 716, no. 1, pp. 1-29, 2012. 6

[6] S. Chatrchyan et al., "Observation of a new boson at a mass of 125 GeV with the CMS experiment at the LHC", Physics Letters B, vol. 716, no. 1, pp. 30-61, 2012. 6

[7] E. Gschwendtner et al., "The AWAKE experimental facility at CERN", in International Particle Accelerator Conference 2014, Dresden, Germany. 6

[8] G. Apollinari, I. Béjar Alonso, O. Brüning, M. Lamont, and L. Rossi, eds., "High-Luminosity Large Hadron Collider (HL-LHC), Preliminary Design Report", CERN, Geneva, Switzerland, 2015. 6

[9] H. Damerau, A. Funken, R. Garoby, S. Gilardoni, B. Goddard, K. Hanke, A. Lombardi, D. Manglunki, M. Meddahi, B. Mikulec, G. Rumolo, E. Shaposhnikova, M. Vretenar and J. Coupard, "LHC Injectors Upgrade, Technical Design Report, Vol. I: Protons", No. CERN-ACC-2014-0337, December 2014. v, 6, 29, 31, 32, 36, 55

[10] F. Tecker, "Longitudinal Beam Dynamics", in CERN Accelerator School (CAS): Advanced Accelerator Physics Course, Trondheim, Norway, 18 - 29 Aug 2013, pp.1-21. iv, 7, 11, 16

[11] F. Gerigk, "Cavity types", in CERN Accelerator School (CAS): RF for accelerators, Ebeltoft, Denmark, pp. 277–298, June 2010. 9

[12] G. Dome, "Theory of RF acceleration", in CERN Accelerator School (CAS): Accelerator Physics, pp. 110–158, Sept. 1985. 9

[13] A. Gallo, "RF systems", in CERN Accelerator School (CAS): Accelerator Physics, Varna, Bulgaria, September, 2010. 10

[14] A. Gallo, "Beam Loading and Low-level RF Control in Storage Rings", in CERN Accelerator School (CAS): Accelerator Physics, Trieste, October 2005. iv, 10, 27

[15] E. Jensen, "Cavity basics", in CERN Accelerator School (CAS): RF for Accelerators, Ebeltoft, Denmark, pp.259-275. 10

[16] J. E. Muller, "Longitudinal intensity effects in the CERN Large Hadron Collider", CERN-THESIS-2016-066 iv, 15

[17] K. Schindl, "Instabilities", in CERN Accelerator School (CAS), Zeuthen, Germany, September 2003. 17

[18] L. Palumbo, V. G. Vaccaro, and M. Zobov. "Wake fields and impedance", in CERN Accelerator School (CAS): Accelerator Physic, Rhodes 1994, LNF-94/041, 1994. 18, 112, 121

[19] A. W. Chao, "Physics of collective beam instabilities in high energy accelerators", Wiley, 1993. 18

[20] R. Garoby, "Beam loading in RF cavities", 4th US-CERN School on Particle Accelerators, Hilton Head Island, SC, USA, 7 - 14 Nov 1990, pp.509-541. 21, 25

[21] D. Boussard, "Beam loading." in CERN Accelerator School (CAS), Oxford, England. iv, 22

[22] R. Garoby, "Low level RF and feedback", No. CERN-PS-97-034-RF, 1997. 23

[23] F. Pedersen, "Beam loading effects in the CERN PS booster", IEEE Transactions on Nuclear Science 22.3 (1975): 1906-1909. 23

[24] P. Baudrenghien, "Low level RF systems for synchrotrons : part II: High Intensity. Compensation of the beam induced effects", in CERN Accelerator School (CAS): Radio Frequency Engineering, Seeheim, Germany, 8 - 16 May 2000, pp.175 (CERN-2005-003). 24, 27

[25] S. Gilardoni and D. Manglunki, Fifty years of the CERN Proton Synchrotron, volume I, 2011, CERN-2011-004. iv, 28

[26] nTOF Collaboration (CERN), "The neutron Time-Of-Flight facility, nTOF, at CERN (I): Technical Description", CERN 13 February 2013. 30

[27] P. Belochitskii et al., "Commissioning and first operation of the antiproton decelerator (AD)", in Proceedings of the nineteenth IEEE Particle Accelerator Conference, Chicago, IL, USA, 2001, edited by Y. Cho (IEEE, New York, 2002), p. 580. 30

[28] J. Schacher. "The DIRAC Experiment at CERN", (DIRAC-CONF-1999-04), 1999. 30

[29] http://cloud.web.cern.ch/cloud/. 30

[30] F. Ravotti et al "A New High-intensity Proton Irradiation Facility at the CERN PS East Area", in Proceedings of Technology and Instrumentation in Particle Physics 2014 (TIPP2014), 2-6 June 2014, Amsterdam, Netherlands. 30

[31] B. Mikulec, A. Blas, C. Carli, A. Findlay, K. Hanke, G. Rumolo, J. Tan, "LHC beams from the CERN PS Booster", CERN, 1211 Geneva 23, Switzerland, Proceedings of PAC09, Vancouver, BC, Canada. 31

[32] K. Schindl, "The PS Booster as Pre-injector for LHC", Part. Accel., Vol. 58, Nb.1-4 (1997), pp. 63-78. 31

[33] R. Garoby, "Demonstration of Bunch Triple Splitting in the CERN PS", in 7th European Particle Accelerator Conference, Vienna, Austria, 26 - 30 Jun 2000, pp.e-proc. 304 31

[34] https://wikis.cern.ch/display/PSOP/Beam+Doc+2016. 33

[35] S. Gilardoni et al.,"The PS Upgrade Programme: Recent Advances", in 4th International Particle Accelerator Conference, Shanghai, China, 12 - 17 May 2013, pp.2594. v, 35

[36] H. Damerau et al., "RF manipulations for higher brightness LHC-type beams", No. CERN-ACC-2013-0210, 2013. 34

[37] E. Shaposhnikova et al., "LHC Injectors Upgrade (LIU) Project at CERN", in 7th International Particle Accelerator Conference, Busan, Korea, 8 - 13 May 2016, MOPOY059. 36

[38] L. Ventura, "Studies of Longitudinal Coupled-Bunch Instabiities in the LHC Injector Chain", PhD thesis 2017, CERN, Geneva, Switzerland. 37

[39] D. Perrelet, "New PS one-turn delay feedbacks and further developments", LIU-DAY 11.04.2014, CERN, Geneva, Switzerland. 37

[40] D. Grier, "The PS 10 MHz Cavity and Power Amplifier", PS/RF Note 2002-073, CERN, Geneva, Switzerland. 38, 49, 87

[41] D. Plathner, "New RF cavities", Design report, CERN/MPS/ML 71-2 DP/ed 3.11.1971, CERN, Geneva, Switzerland. 39

[42] H.C. Grassmann, R. Jankobsky and W. Pirkl, "New RF Syestem for the 28 GeV Proton Synchrotron at CERN", Siemens Review XLIV (1977) No. 4, CERN, Geneva, Switzerland. 41

[43] R. Garoby, J. Jamsek, P. Konrad, G. Lobeau and G. Nassibian, "RF system for high beam intensity acceleration in the CERN PS", Particle Accelerator Conference, 1989. Accelerator Science and Technology, Proceedings of the 1989 IEEE, Chicago, IL, 1989, pp. 135-137 vol.1. 43

[44] OrCAD Pspice Designer, https://www.orcad.com/. 57

[45] G. Favia, "The CERN PS main RF system: a study for possible upgrades in the perspective of the ultimate LHC performance", CERN-THESIS-2013-192, CERN, Geneva, Switzerland. 57

[46] R.G. Carter, "RF power generation", arXiv:1112.3209, contribution to the CAS - CERN Accelerator School: Specialised Course on RF for Accelerators, 8 - 17 Jun 2010, Ebeltoft, Denmark. 57

[47] http://www.mathworks.com/products/matlab/. 57

[48] G. Favia, H. Damerau, V. Desquiens, S. Energico, M. Morvillo, D. Perrelet, C. Rossi, "The PS 10 MHz High Level RF System Upgrade", 7th International Particle Accelerator Conference (IPAC'16), Busan, Korea, May 8-13, 2016 (pp. 622-625), JACOW, Geneva, Switzerland. 63

[49] F. Langford-Smith, "Radiotron designer's handbook", Tube Division, Radio Corporation of America, 1960. 64

[50] P. L. D. Abrie, "The design of impedance-matching networks for radio-frequency and microwave amplifiers", Artech House on Demand, 1985 (Chapter 5). 71, 102

[51] A. Labanc, "Reduction of the group delay of a wideband cavity power amplifier to permit the reduction of the cavity equivalent impedance by increased feedback", PhD Thesis, Diploma Thesis, Slovak University of Technology, Bratislava, CERN, Geneva, Switzerland. 70

[52] G. Favia, F. Caspers, M. Morvillo, C. Rossi, C. Vollinger, "Measurement Techniques and Application of Combined Parallel/Orthogonal Magnetic Bias on a Ferrite Tuned Resonator in Low Frequency Range (3-10 MHz)", in 6th International Particle Accelerator Conference (IPAC'15), Richmond, VA, USA, (pp. 3087-3089), JACOW, Geneva, Switzerland.

[53] "Soft Ferrites Accessories", Data Handbook 2013, Ferroxcube. 89, 92

[54] David M. Pozar, "Microwave engineering", John Wiley & Sons, 2009. 90

[55] F. Caspers, private communication. 93

[56] I.S.K. Gardner, "Ferrite Dominated Cavities", CERN Accelerator School (CAS): RF Engineering for Particle Accelerators, Oxford, UK, 3 - 10 Apr 1991, pp.349-374. 97

[57] J. Eberhardt, F. Caspers, and C. Vollinger, "Ferrite Material Characterization in a Static Bias Field for the Design of a Tuneable Cavity", Proceedings of IPAC2014, Dresden, Germany. 99

[58] W. R. Smythe, "Reducing ferrite tuner power loss by bias field rotation." IEEE Transactions on Nuclear Science 30.4 (1983): 2173-2175. 101, 106

[59] R. L. Poirier, "Perpendicular biased ferrite-tuned cavities" Particle Accelerator Conference, 1993, Proceedings of the 1993. IEEE, 1993. 101

[60] C. Vollinger, F. Caspers, "Enlargement of Tuning Range in a Ferrite-Tuned Cavity Through Superposed Orthogonal and Parallel Magnetic Bias", Proceedings of IPAC2013, Shanghai, China. 106

[61] G. Favia, H. Damerau, M. Migliorati, M. Morvillo, C. Rossi, "Study of the beam-cavity interaction in the PS RF 10 MHz system", International Particle Accelerator Conference (IPAC'16), Busan, Korea, May 8-13, 2016 (pp. 622-625), JACOW, Geneva, Switzerland. 111

[62] K. Schindl, "Instabilities", CAS - CERN Accelerator School: Intermediate Course on Accelerator Physics, Zeuthen, Germany, 15-26 Sep 2003, pp.321-342. 112

[63] L. Ventura, "Study of longitudinal multibunch instabilities for LHC-type beams at the CERN Proton Synchrotron", CERN-THESIS-2013-191. 113

[64] H. Damerau et al., "Longitudinal Coupled-bunch Instabilities in the CERN PS" Particle Accelerator Conference, 2007, PAC. IEEE, 2007. 113, 130

[65] https://www.cst.com/. 113

[66] "Technical specification for the ferrite used in the improved cavities of the CERN Proton Synchrotron", MPS/SR/SPEC/69-5, 5.11.1969, CERN, Geneva, Switzerland. 114

[67] CST STUDIO SUITE Help documentation. 116

[68] Pspice User's Guide, http://www.seas.upenn.edu/~jan/spice/PSpice_UserguideOrCAD.pdf, p. 349. 124